



Strål  
säkerhets  
myndigheten

Swedish Radiation Safety Authority

**Authors:** Jeoung Seok Yoon<sup>1)</sup>, Ove Stephansson<sup>1)</sup> and Ki-Bok Min<sup>2)</sup>

<sup>1)</sup>Stephansson Rock Consultant, Berlin, Germany

<sup>2)</sup>Seoul National University, Seoul, South Korea

Technical Note 74; page 61-142

2014:59

Relation between earthquake magnitude,  
fracture length and fracture shear displacement in the KBS-3 repository at Forsmark  
Main Review Phase



## 6. Modelling of target fracture responses to earthquakes on deformation zones

### 6.1. Earthquake at selected deformation zones – present-day “most likely” reverse stress field – Horizontal section model

The modelling cases in this Chapter do not include rock mass heating. Therefore, the modelling was performed without thermal-mechanical coupling in PFC. Target fractures and deformation zones are shortened with “TFs” and “DZs”, respectively, in the following.

#### 6.1.1. Earthquake at zone ZFMWNW0809A

This modelling case assumes that an earthquake takes place at zone ZFMWNW0809A, located West of the Singö fault and East of the repository area. This DZ is chosen as it is the largest in the SKB’s local model area and it is one of the most unstable DZs (see *CFS* in Figure 28). The location of this DZ can be found in Figure 31. Earthquake induced seismicity and the TF shear displacements are investigated for the “most likely” stress field by SKB.

Figure 52 shows the earthquake induced seismic events due to fracturing of rock mass and slip of the joints planes that constitute the TFs and DZs, after activation of zone ZFMWNW0809A, with realization DFN03h. The hypocentre is marked by a pink star of which the simulated maximum moment magnitude is M4.60. Many of the large co-seismic events take place at DZ-DZ and TF-DZ intersections and at tip of TFs and DZs. The largest magnitude of the co-seismic events is M1.81. Small magnitude events ( $< M0.29$ ) are scattered in the rock mass.

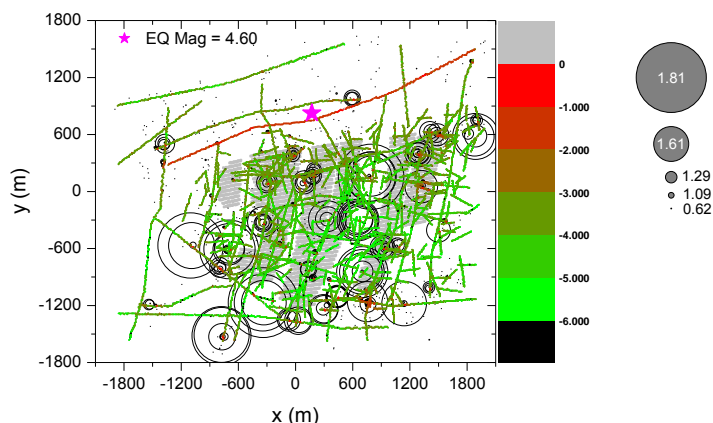


**Figure 52.** Spatial distribution of induced seismic events and shear displacements of the smooth joints of the TFs and DZs, due to an earthquake at zone ZFMWNW0809A with realization DFN03h (Figure A3-17).

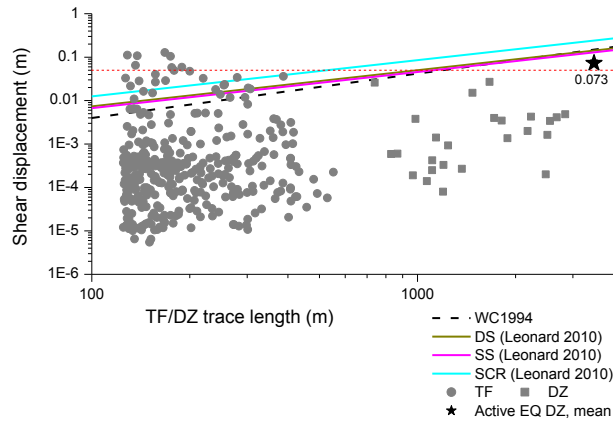


**Figure 53.** Shear displacement of the TFs and DZs with respect to length, due to earthquake at zone ZFMWNW0809A with realization DFN03h and comparison with empirical regressions (Figure A3-18).

Figure 53 shows the induced shear displacements of the TFs and DZs with respect to their trace length. Length and shear displacement of zone ZFMWNW0809A are marked by a black star (mean values). The four plotted regressions are taken from Wells and Coppersmith (1994), and Leonard (2010) for Dip Slip (DS), Strike Slip (SS) and Stable Continental Region (SCR). The figure shows that the point with length versus displacement of zone ZFMWNW0809A fits well to the regressions, which implies that the simulated earthquake closely match the field observations in the literature in terms of length versus displacement. Data points of TFs and DZs, in general, show no clear trend of in the plot of length versus displacement. A few of TFs are showing displacement larger than the canister damage threshold of 50 mm, i.e. data points above the red dashed horizontal line.

The box-and-whisker diagram in Figure 54 shows that, although a few data points are exceeding 50 mm, these data points are above the 95th percentile, therefore can be regarded as outliers.

Figure 55 shows that, in general, the greater the distance from the earthquake hypocentre, the smaller the displacement of the joint segments consisting the TFs and DZs. The box-and-whisker diagram is applied to the data sets. It is seen that those data points above the canister damage threshold are all above the 95th percentile which can be regarded as outliers.

It should be noted that the numbers of data points in Figure 53 and Figure 55 are different. In Figure 53, the average values of the shear displacements on smooth joints of each TF are used. The number of data points in Figure 55, on the contrary, correspond to the total number of smooth joints constituting the TFs. This is done to obtain unambiguous distances between the point of occurrence of the shear displacement and the hypocentre, which cannot be obtained when averaging the shear displacements. In general, shear displacement of smooth joints decreases as the distance from the earthquake hypocentre increases. However, unlike in SKB's observation, no such strong exponential decreasing relation is found.

Results of another modelling case with realization DFN06h are provided in Appendix 3 (Figure A3-22 to A3-26). Similar results are found, where some of the TFs are showing displacement larger than 50 mm, but can be regarded as outliers.

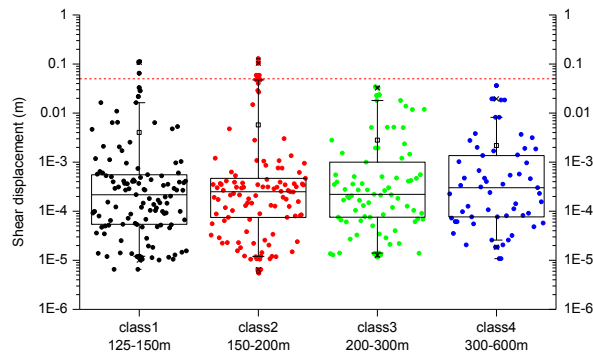


**Figure 54.** Box-and-whisker diagram of the average shear displacements on TFs in four length classes, due to earthquake at zone ZFMWNW0809A with realization DFN03h (Figure A3-19).

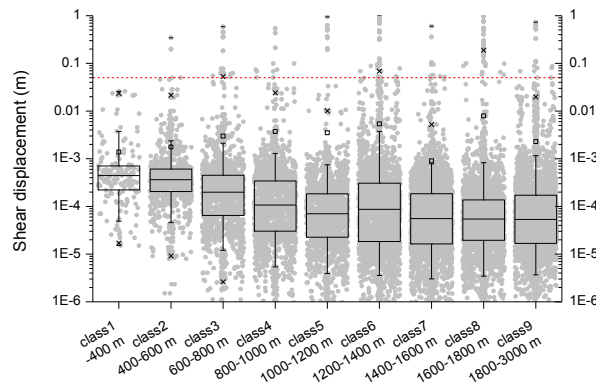
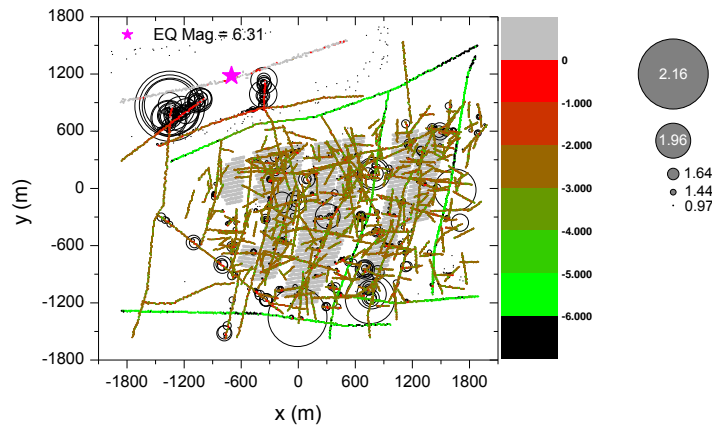


**Figure 55.** Box-and-whisker diagram of the shear displacement of all smooth joints of TFs in nine classes of distance from the hypocentre of simulated earthquake (Figure A3-21).

### 6.1.2. Earthquake at zone ZFMWNW0001, powered shear force

This modelling case assumes that an earthquake takes place at zone ZFMWNW0001, which is the Singö fault truncated by the model boundary. This modelling case assumes that the part of the trace of Singö fault included in the model is activated (2,476 m), but this would only produce magnitudes of  $M \sim 5$ . The magnitude of the correspondent earthquake ( $M6.31$ ), however, is inferred based on a much longer trace than in the PFC model, which is calculated based on the rupture area of  $205.7 \text{ km}^2$  assumed by Backers et al. (2014) in their regional earthquake modelling. This corresponds to a total activated trace length and out-of-plane width of the zone of about 15 km. To model the earthquake, the shear force on the smooth joints belonging to the zone ZFMWNW0001 is increased, and then the bond strength is released in order to power up the seismic magnitude. In this way, a more realistic set of earthquake magnitude and shear displacement data is obtained. The location of this zone can be seen in Figure 31. Earthquake induced seismicity and shear displacements on TFs are investigated for the “most likely” stress field by Martin (2007).

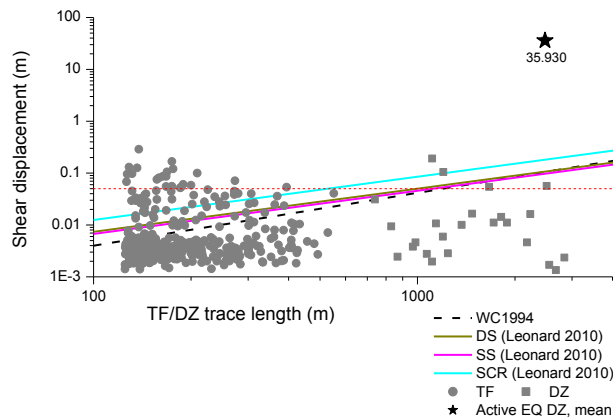
Figure 56 shows the earthquake induced seismic events by fracturing of rock mass and slip of the joint planes that constitute the TFs and DZs after activation of zone ZFMWNW0001, with realization DFN03h. The hypocentre is marked by pink star of which the simulated moment magnitude is M6.31. Many of the large induced events take place at zone ZFMWEW0137 and zone ZFMNNE2308 and mostly at the tip area. The largest magnitude of the co-seismic event is M2.16. TFs within the repository footprint undergo shear displacement larger than 1 mm.



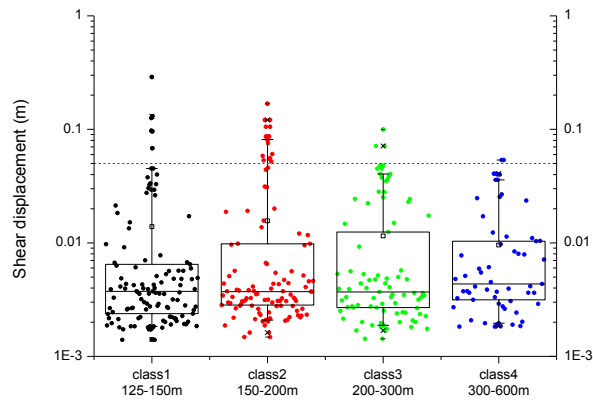
**Figure 56.** Spatial distribution of the induced seismic events and shear displacement of smooth joints of the TFs and DZs, due to earthquake at zone ZFMWNW0001 with realization DFN03h (Figure A3-27).

Figure 57 shows the induced shear displacements of the TFs and DZs with respect to their length. Length and shear displacement of zone ZFMWNW0001 are marked by a black star (when assuming an activated length as in the PFC model, instead of 15 km). It is seen that the shear displacement is about a few tens of meters, due to the forced increase of shear force on the smooth joints. As the simulated displacement far exceeds the regressions, it is reasonable to assume that a larger trace of the zone ZFMWNW0001 should be activated. This issue is discussed later in Chapter 8.

There are many TFs showing displacement larger than the canister damage threshold of 50 mm, i.e. data points above the red horizontal line. Compared to the previous modelling case, where the zone ZFMWNW0809A is activated with resulting moment magnitude of M4.60, the number of TFs with shear displacement exceeding 50 mm is 22, whereas it was 7 in the previous modelling case. This seems reasonable as more TFs should respond with larger shear displacement to a larger magnitude seismic event.



**Figure 57.** Shear displacement of the TFs and DZs with respect to their length, due to earthquake at zone ZFMWNNW0001 with realization DFN03h and comparison with empirical regressions (Figure A3-28). The trace length of zone ZFMWNNW0001 is plotted as in the PFC model (2,476 m) rather than as used for the magnitude calculation (about 15 km).



**Figure 58.** Box-and-whisker diagram of the TF shear displacement in four length classes, due to earthquake at zone ZFMWNNW0001 with realization DFN03h (Figure A3-29).

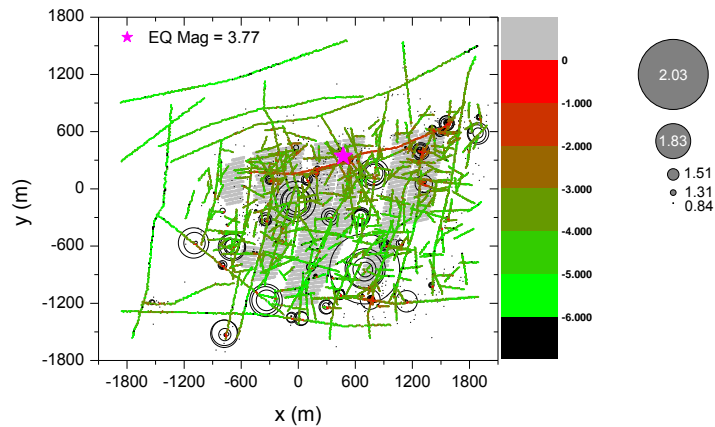
The box-and-whisker diagram is applied to the TFs shear displacement data sets as shown in Figure 58. The figure shows that in particular those TFs in length class 2 (150 to 200 m) are sheared beyond the canister damage thresholds, and at the same time are below the 95th percentile and therefore cannot be regarded as outliers. Among 22 TFs exceeding the canister damage threshold, 7 cannot be regarded as outliers (please notice that these number are coincidentally the same as in the previous page). This implies that there is a risk of canister damage due to the earthquake.

Results of another modelling case with realization DFN06h are provided in Appendix 3 (Figure A3-32 to A3-36). Compared to the modelling case with DFN03h, the simulated maximum magnitude is M5.82 and those TFs sheared larger than 50 mm can all be regarded as outliers.

### 6.1.3. Earthquake at zone ZFMWNW2225

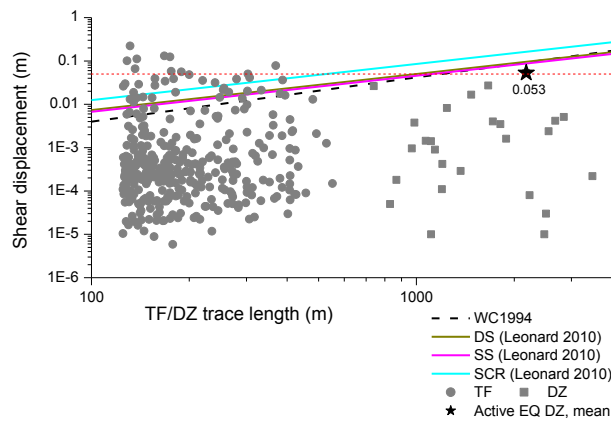
This modelling case assumes that an earthquake takes place at zone ZFMWNW2225. This deformation zone is chosen because it is expected to pose the largest threat to the repository safety as it cuts across three deposition panels. The location of this deformation zone can be found in Figure 31. Earthquake induced seismicity and the TF shear displacements are investigated for the “most likely” stress condition by SKB.

Figure 59 shows the earthquake induced co-seismic events and shear displacements of the joint planes that constitute the TFs and DZs after activation of the zone ZFMWNW2225 with realization DFN03h. Multiple hypocentres are produced and the arithmetic average of the magnitudes and of their coordinates is assigned to the hypocentre with  $M_{3.77}$  in Figure 59 (pink star). Similarly to the previous modelling cases, moderately large magnitude events ( $M_{1.83} < M_w < M_{2.03}$ ) take place along the earthquake hosting DZ and DZ-DZ intersection and at the tips of DZs.



**Figure 59.** Spatial distribution of the induced seismic events and shear displacement of the smooth joints that constitute the TFs and DZs, due to earthquake at zone ZFMWNW2225 with realization DFN03h (Figure A3-37).

Figure 60 shows the induced shear displacements of the TFs and DZs with respect to their length. Length and shear displacement of zone ZFMWNW2225 are marked by black star (mean values). The figure shows that the length versus displacement of zone ZFMWNW2225 fits well to the regressions in the literature. A few of TFs are showing displacement larger than the canister damage threshold and even larger than 100 mm.

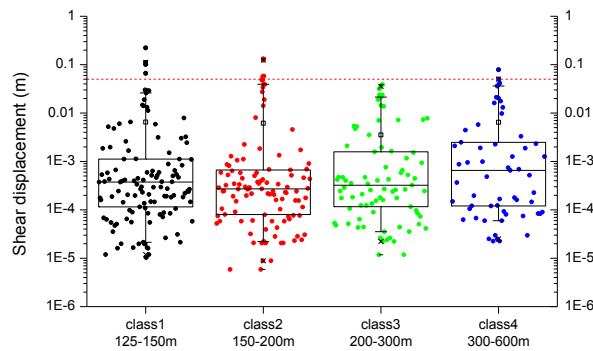


**Figure 60.** Shear displacement of the TFs and DZs with respect to length, due to earthquake at zone ZFMWNNW2225 with realization DFN03h and comparison with empirical regressions (Figure A3-38).

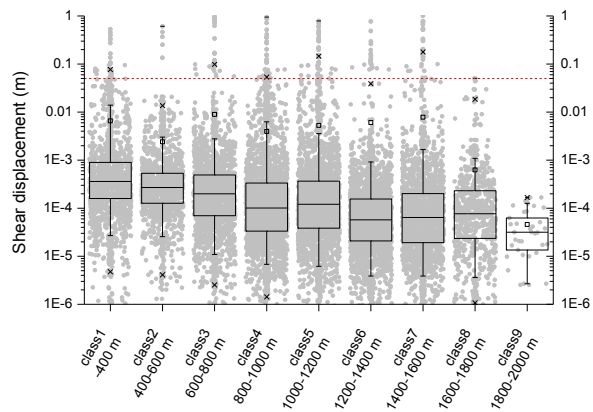
The box-and-whisker diagram in Figure 61 shows that, although a few data points are exceeding 50 mm, these data points are above the 95th percentile and can be regarded as outliers.

Figure 62 shows that, in general, the greater distance from the earthquake hypocentre the smaller the displacement of the joint segments. Also, it is seen that those data points above the canister damage threshold is above the 95th percentile, which is a limit for outliers in each distance class in this report.

Results of another modelling case with realization DFN06h are provided in Appendix 3 (Figure A3-42 to A3-46). Similarly, results are found where some of the TFs are showing displacement larger than 50 mm, but can be regarded as outliers.



**Figure 61.** Box-and-whisker diagram of the TF shear displacement in four trace length classes, due to earthquake at zone ZFMWNNW2225 with realization DFN03h (Figure A3-39).



**Figure 62.** Box-and-whisker diagram of the shear displacement smooth joints of TFs in nine classes of distance from the hypocentre of simulated earthquake (Figure A3-41).

## 6.2. Earthquake at selected deformation zones – glacial induced stress field at the time of forebulge – Horizontal section model

### 6.2.1. Earthquake at zone ZFMWNW0809A

This modelling case assumes that an earthquake takes place at deformation zone ZFMWNW0809A West of Singö fault (ZFMWNW0001) during a future glacial period and in particular at the time of forebulge ahead of the ice front. Figure 63 shows the earthquake induced seismic events and shear displacements of the joint planes that constitute the TFs and DZs after activation of zone ZFMWNW0809A, with realization DFN03h. The hypocentre (pink star) host an event of magnitude M4.70. There is a slight difference in magnitude compared to the modelling case with the present-day “most likely” stress field (M4.60, see Sec. 6.1.1) that comes from the fact that the amount of strain energy stored at the DZs is different under the stress field glacially induced at time of forebulge. The largest magnitude of the co-seismic events is M1.92. Many of the induced events take place at DZ-DZ intersections. This with other events lies at about 1800 m from the host zone at the Western border of the repository. Occurrence of these events indicates that an earthquake can trigger another large magnitude event at a far distance away from the hypocentre, and even at opposite side of the repository. Small magnitude events (< M0.73) are scattered in the rock mass. The red colour along the deformation zone in Figure 63 indicates large shear displacements induced by the earthquake on the host zone.

Figure 64 shows the induced shear displacements of the TFs and DZs with respect to their length. Length and shear displacement of the zone ZFMWNW0809A is marked by black star (mean values). The figure shows that length versus displacement of ZFMWNW0809A fit well to the regressions in the literature. A few of the TFs are showing displacement larger than the canister damage threshold of 50 mm.

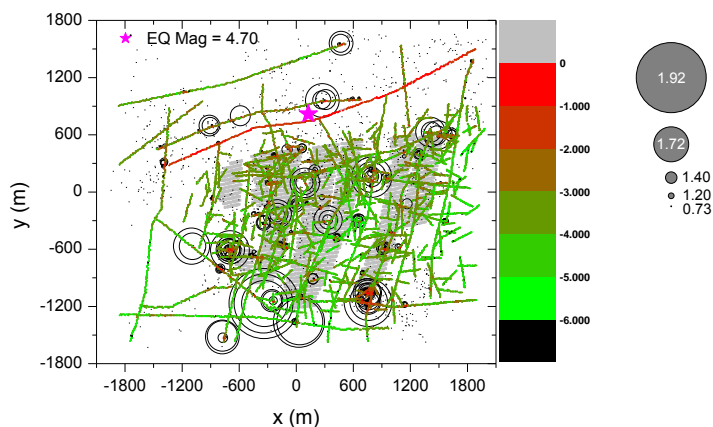


**Figure 63.** Spatial distribution of the induced seismic events and shear displacement of the smooth joints that constitute the TFs and DZs, due to earthquake at zone ZFMWNW0809 with realization DFN03h (Figure A3-47).

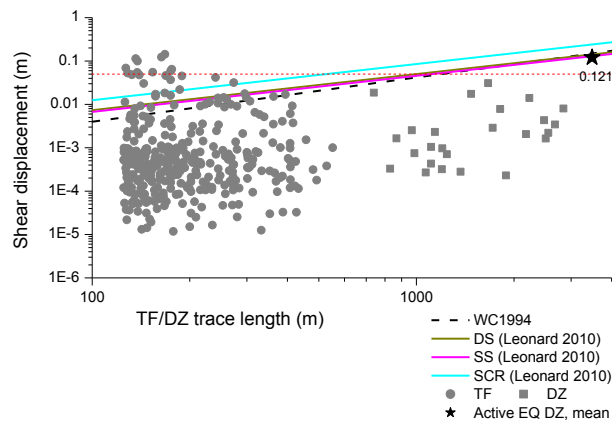


**Figure 64.** Shear displacement of the TFs and DZs with respect to length, due to earthquake at zone ZFMWNW0809A with realization DFN03h and comparison with empirical regressions (Figure A3-48).

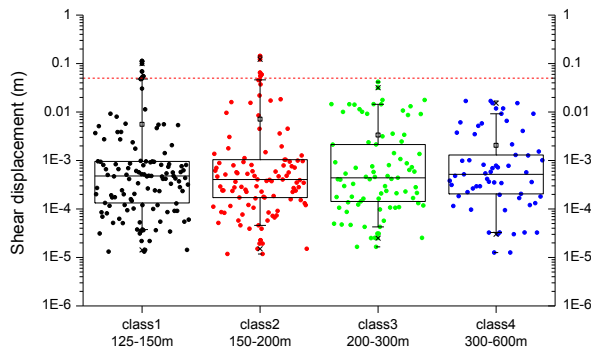


**Figure 65.** Box-and-whisker diagram of the TF shear displacement in four length classes, due to earthquake at zone ZFMWNW0809A with realization DFN03h (Figure A3-49).

The box-and-whisker diagram in Figure 65 shows that, although a few data points are exceeding 50 mm, these data points are above the 95th percentile and can be regarded as outliers.

Results for another modelling case with realization DFN06h are provided in Appendix 3 (Figure A3-52 to A3-56). Similar results are found, where some of the TFs are showing displacement larger than 50 mm, but can be regarded as outliers.

### 6.2.2. Earthquake at zone ZFMWNW0001, powered shear force

This modelling case assumes that an earthquake takes place at zone ZFMWNW0001, which is the truncated Singö fault. Same as in Sec. 6.1.2, shear force on the smooth joints is increased upon releasing of the bond strength, in order to power up the seismic magnitude. The trace length and out-of-plane size of the zone were also assumed to be about 15 km according to Backers et al. (2014). This consequently resulted in an earthquake of magnitude of M6.42, which is slightly larger than the earthquake for the present-day “most likely” stress field (M6.31). The slightly larger

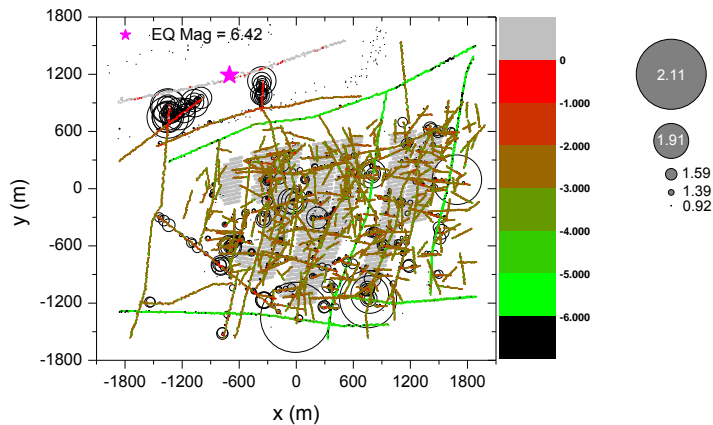
magnitude may have resulted from a higher level of anisotropy of the glacial induced stress field at time of forebulge, i.e.  $SH/Sh = 40 \text{ MPa}/17 \text{ MPa}$ , compared to the present-day “most likely” stress field, i.e.  $SH/Sh = 40 \text{ MPa}/22 \text{ MPa}$ .

Figure 66 shows the earthquake induced seismic events and shear displacements of the joint planes that constituting the TFs and DZs after activation of zone ZFMWNW0001, with realization DFN03h. The hypocentre is marked by pink star.

Similarly to the observation from Figure 56, it can be seen that most of the TFs are showing greenish-red to red colour shear displacements ( $> 1 \text{ mm}$ ). Quite a number of TFs are showing displacement larger than the canister damage threshold of  $50 \text{ mm}$ . Also many of the large events take place at zone ZFMEW0137 and zone ZFMNNE2308, and mostly at the tip areas. The largest magnitude of the co-seismic event is  $M2.11$ . Figure 67 shows the induced shear displacements of the TFs and DZs with respect to their length. Length and shear displacement of zone ZFMWNW0001 is marked by black star (mean value).

The box-and-whisker diagram in Figure 68 shows that 7 TFs in length class 2 are exceeding  $50 \text{ mm}$ , which is the canister damage threshold, and are below the 95th percentile. Therefore these shear displacements cannot be regarded as outliers. The result of this modelling case indicates that a risk of canister damage by the shear displacement of TFs is predicted when the zone ZFMWNW0001 is activated by a  $M6.42$  earthquake that can occur during a future glacial period at the time of forebulge.

The results of another modelling case with realization DFN06h are provided in Appendix 3 (Figure A3-62 to A3-66). In this case the magnitude of the simulated earthquake is  $M6.47$  and the number of TFs with shear displacements larger than  $50 \text{ mm}$  is 8 and cannot be regarded as outliers (see Figure A3-64 where 5 TFs are in class 2, 1 TF in class 3 and 2 TFs in class 4).



**Figure 66.** Spatial distribution of the induced seismic events and shear displacement of the smooth joints that constitute the TFs and DZs, due to earthquake at zone ZFMWNW0001 with realization DFN03h (Figure A3-57).

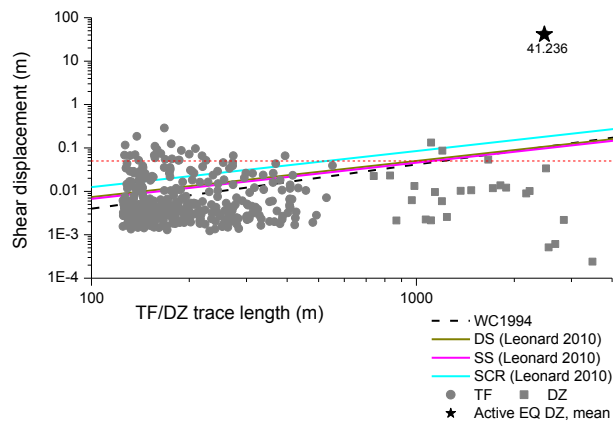


**Figure 67.** Shear displacement of the TFs and DZs with respect to length, due to earthquake at zone ZFMWNW0001 with realization DFN03h and comparison with empirical regressions (Figure A3-58). The trace length of zone ZFMWNW0001 is plotted as in the PFC model (2,476 m) rather than as used for the magnitude calculation (about 15 km).

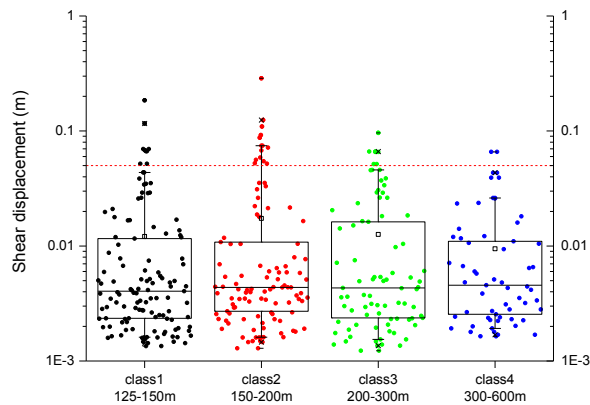


**Figure 68.** Box-and-whisker diagram of the TF shear displacement in four trace length classes, due to earthquake at zone ZFMWNW0001 with realization DFN03h (Figure A3-59).

### 6.2.3. Earthquake at zone ZFMWNW2225

This modelling case assumes that an earthquake takes place at deformation zone ZFMWNW2225. Figure 69 shows the earthquake induced seismic events and shear displacements of the joint planes constituting the TFs and DZs after activation of zone ZFMWNW2225, with realization DFN03h. The hypocentres are marked by a pink star and the simulated magnitude is M4.09. The figure shows many events taking place within the repository footprint. Also, similarly to the previous modelling cases, there are co-seismic events taking place at a far distance away from the hypocentres. The largest magnitude of the co-seismic event is M1.94.

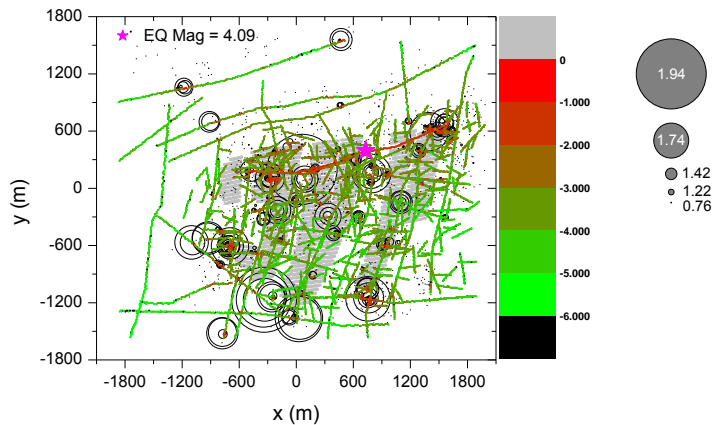


**Figure 69.** Spatial distribution of the induced seismic events and shear displacement of the smooth joints constituting the TFs and DZs, due to earthquake at zone ZFMWNW2225 with realization DFN03h (Figure A3-67).

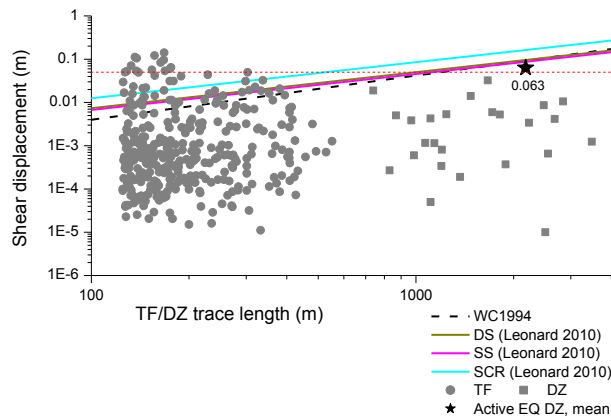


**Figure 70.** Shear displacement of the TFs and DZs with respect to length, due to earthquake at zone ZFMWNW2225 with realization DFN03h and comparison with empirical regressions (Figure A3-68).

Figure 70 shows the induced shear displacements of the TFs and DZs with respect to their length. Length and shear displacement of zone ZFMWNW2225 are marked by black star (mean values). A few of TFs are showing larger displacement than the canister damage threshold of 50 mm.

The box-and-whisker diagram in Figure 71 shows that, unlike in previous modelling cases under the “most likely” stress field, there are two TFs in the length class 2 for which the shear displacement is exceeding 50 mm, but below the 95th percentile (60 mm). These cannot be regarded as outliers, and imply that occurrence of an earthquake at zone ZFMWNW2225 can induce shear displacement of TFs exceeding the canister damage threshold. The maximum value of the shear displacements at TFs are 111, 141, 44 and 50 mm for length class 1, 2, 3 and 4, respectively.

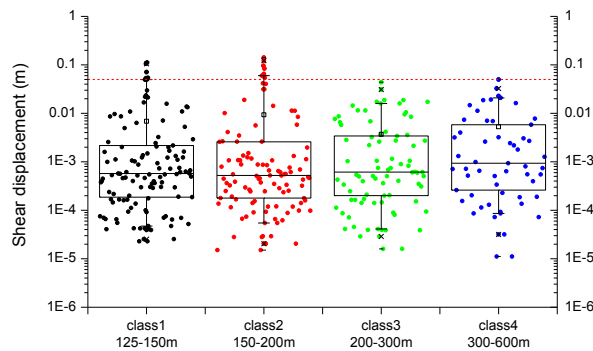


**Figure 71.** Box-and-whisker diagram of the TF shear displacement in four trace length classes, due to earthquake at zone ZFMWNW2225 with realization DFN03h (Figure A3-69).

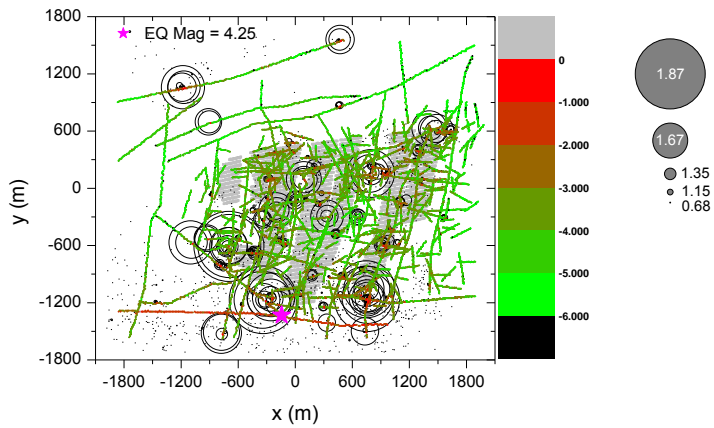
Results of another modelling case with realization DFN06h are provided in Appendix 3 (Figure A3-72 to A3-76). Similar results are found, where one TF is showing displacement larger than 50 mm, which cannot be regarded as an outlier.

#### 6.2.4. Earthquake at zone ZFMNW1200

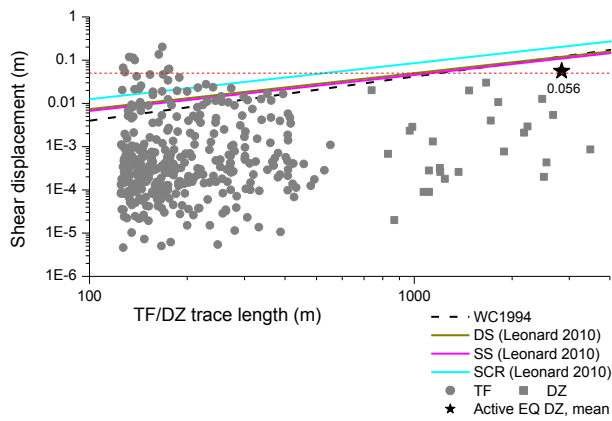
This modelling case assumes that an earthquake takes place at zone ZFMNW1200. This DZ is selected as it shows the largest *CFS* at the time of forebulge and estimated to be the most unstable (see Figure 29). Figure 72 shows the earthquake induced seismic events and shear displacement of the joint planes that constitute the TFs and DZs after activation of zone ZFMNW1200, with realization DFN03. The hypocentre is marked by a star and the simulated magnitude is M4.25. The largest magnitude of the co-seismic event is M1.87. The figure shows many events occurring along the nearby DZs, such as ZFMNNW0100 and ZFMWNW0123, which are also estimated to be unstable based on their *CFS* (see Sec. 4.7). For this reason, the intensity of the co-seismic events near the earthquake hosting zone is high. Similarly to previous modelling cases, there are a number of moderate magnitude events taking place at far distance away from the hypocentres.

Figure 73 shows the induced shear displacements of the TFs and DZs with respect to their length. Length and shear displacement of zone ZFMNW1200 are marked by black star (mean values). A few of the TFs are showing displacements larger than the canister damage threshold of 50 mm. However, as shown in the box-and-whisker diagram in Figure 74, these data points can be regarded as outliers.

Results of another modelling case with realization DFN06h are provided in Appendix 3 (Figure A3-82 to A3-86).



**Figure 72.** Spatial distribution of the induced seismic events and shear displacement of the smooth joints constituting the TFs and DZs, due to earthquake at zone ZFMNW1200 with realization DFN03h (Figure A3-77).



**Figure 73.** Shear displacement of the TFs and DZs with respect to length, due to earthquake at zone ZFMNW1200 with realization DFN03h and comparison with empirical regressions (Figure A3-78).

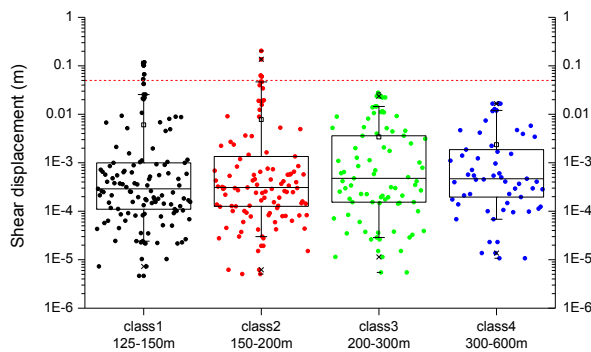


**Figure 74.** Box-and-whisker diagram of the TF shear displacement in four trace length classes, due to earthquake at zone ZFMNW1200 with realization DFN03h (Figure A3-79).



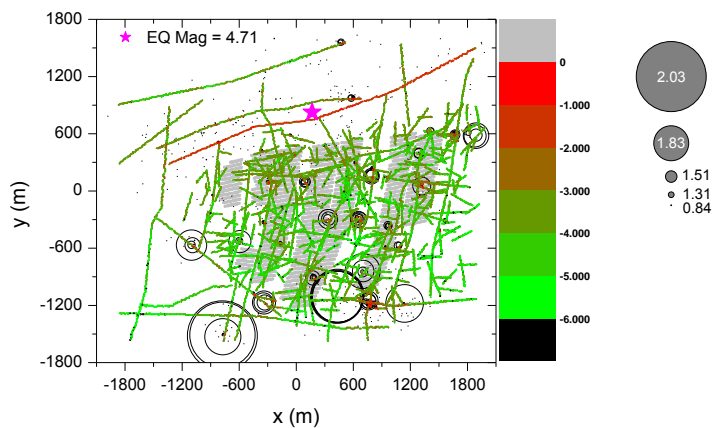
### 6.3. Earthquake at selected deformation zones – glacial induced stress field at the time of maximum ice cover – Horizontal section model

#### 6.3.1. Earthquake at zone ZFMWNW0809A

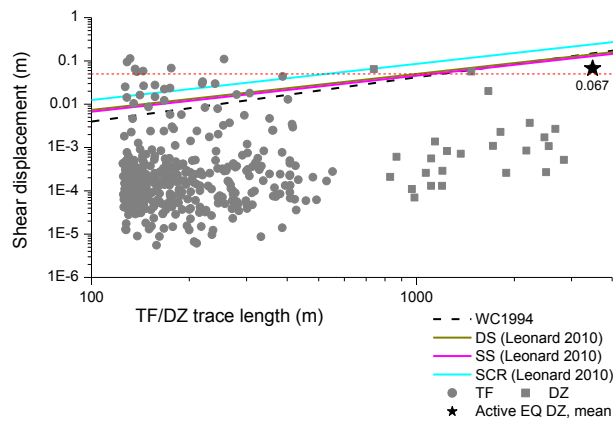
This modelling case assumes that an earthquake takes place at zone ZFMWNW0809A during a future glacial period at the time of maximum thickness of ice cover. Figure 75 shows the earthquake induced seismic events and shear displacements of the TFs right after activation of zone ZFMWNW0809A, with realization DFN03h. The hypocentre is marked a star, and the simulated magnitude is M4.71. The largest magnitude of the co-seismic event is M2.03. Small magnitude events (< M0.84) are scattered in the rock mass. There are events at about 1800 m away from the zone. Occurrence of these events indicates that an earthquake can trigger another event at a far distance away from the hypocentre on the host zone.

Figure 76 shows the induced shear displacements of the TFs and DZs with respect to their length. Length and shear displacement of zone ZFMWNW0809A are marked by a black star (mean values). A few of TFs are showing displacement larger than the canister damage threshold 50 mm, which are all above the 95th percentile and therefore can be regarded as outliers.

Results of another modelling case with realization DFN06h are provided in Appendix 3 (Figure A3-92 to A3-96). Similar results are found where some of the TFs are showing displacement larger than 50 mm, but can be regarded as outliers.



**Figure 75.** Spatial distribution of the induced seismic events and shear displacement of the smooth joints that constitute the TFs and DZs, due to earthquake at zone ZFMWNW0809A with realization DFN03h (Figure A3-87).



**Figure 76.** Shear displacement of the TFs and DZs with respect to length, due to earthquake at zone ZFMWNW0809A with realization DFN03h and comparison with empirical regressions (Figure A3-88).

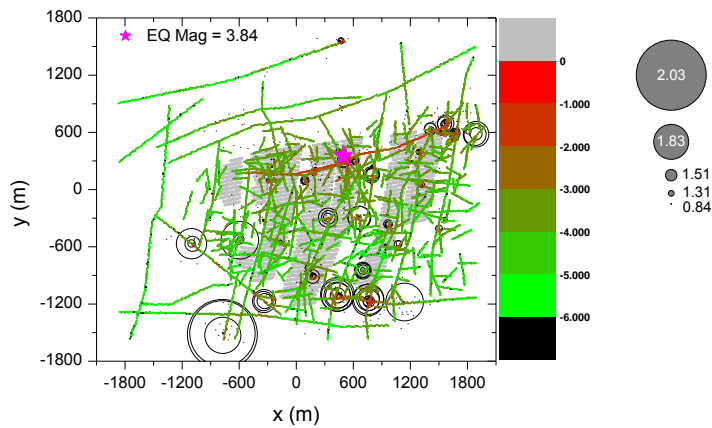


**Figure 77.** Spatial distribution of the induced seismic events and shear displacement of the smooth joints constituting the TFs and DZs, due to earthquake at zone ZFMWNW2225 with realization DFN03h (Figure A3-97).

### 6.3.2. Earthquake at zone ZFMWNW2225

This modelling case assumes that an earthquake takes place at zone ZFMWNW2225. This DZ intersects three repository panels and is expected to have the largest threat to the repository safety if activated. Figure 77 shows the earthquake induced seismic events and shear displacements of the joint planes that constitute the TFs and DZs after activation of zone ZFMWNW2225, with realization DFN03h. The hypocentre is marked by a star, and the simulated magnitude is M3.84. The largest magnitude of the co-seismic event is M2.03. Similar to previous modelling cases, there are a number of co-seismic events taking place at a far distance away from the hypocentre on zone ZFMWNW2225.

Figure 78 shows the induced shear displacements of the TFs and DZs with respect to their length. Length and shear displacement of the zone ZFMWNW2225 are marked by a black star (mean values). The figure shows that very few of TFs are showing

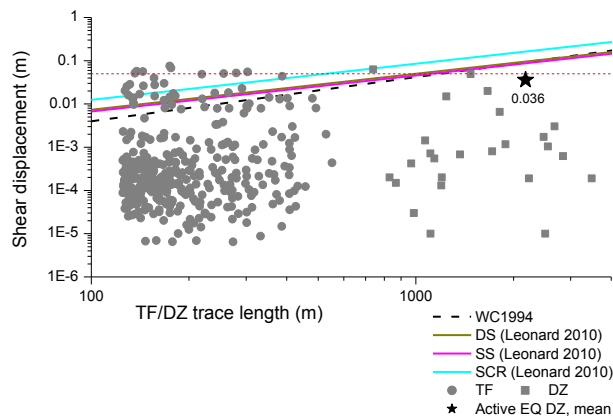


**Figure 78.** Shear displacement of the TFs and DZs with respect to length, due to earthquake at zone ZFMWNW2225 with realization DFN03h and comparison with empirical regressions (Figure A3-98).

shear displacement larger than 50 mm, and these are all below the 95th percentile threshold (Figure A3-99).

Results of another modelling case with realization DFN06h are provided in Appendix 3 (Figure A3-102 to A3-106). Similar results are found where a few TFs are showing displacement larger than 50 mm, but can be regarded as outliers.

### 6.3.3. Earthquake at zone ZFMNW1200

This modelling case assumes that an earthquake takes place at zone ZFMNW1200. Figure 79 shows the earthquake induced seismic events and shear displacements of the joint planes constituting the TFs and DZs after activation of zone ZFMNW1200, with realization DFN03h. The hypocentre is marked by a star, and the simulated magnitude is M4.60. The figure shows many co-seismic events taking place along and near zone ZFMNW1200 and small magnitude within the repository footprint. The intensity of the co-seismic events in terms of magnitude and concentration is similar to those observed in the previous modelling case with glacial induced stress field at the time of forebulge (see Sec. 6.2.4).

Shear displacements of the TFs (Figure A3-108) are analysed by the box-and-whisker diagram, which shows that all the TFs exceeding 50 mm shear displacement can be regarded as outliers (Figure A3-109).

Results of another modelling case with realization DFN06h are provided in Appendix 3 (Figure A3-112 to A3-116). Similar results are found, where a few of the TFs are showing displacement larger than 50 mm, but can be regarded as outliers.

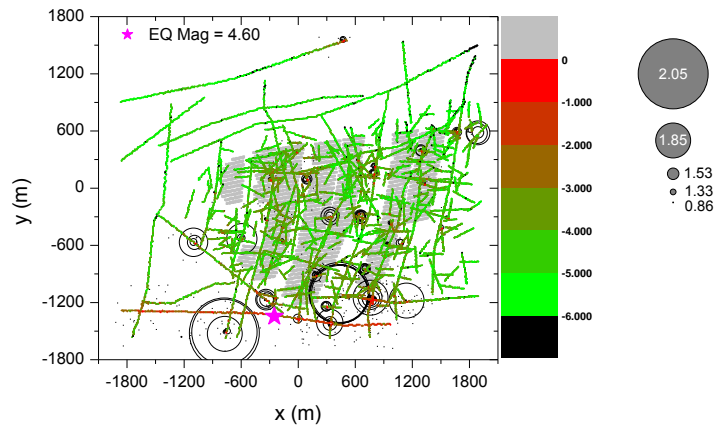


**Figure 79.** Spatial distribution of the induced seismic events and shear displacement of the smooth joints that constitute the TFs and DZs, due to earthquake at zone ZFMNW1200 with realization DFN03h (Figure A3-107).

## **6.4. Earthquake at selected deformation zones – present-day “most likely” reverse stress field – Vertical section model**

In this section, three modelling cases are investigated for the vertical section model under present-day “most likely” reverse stress field by SKB. The first case assumes that one of the gently dipping DZs, ZFMA2, is activated with an earthquake. The second case assumes that multiple deformation zones, ZFMA2, ZFMA3, ZFMA8 and F1 are activated at the same time. The third case is same as in the second one, except that the shear force acting on the joint planes in the activated zones are increased to simulate higher magnitude earthquake (“powered shear force”). Two DFN-realizations were used, DFN03v and DFN06v.

### **6.4.1. Earthquake at zone ZFMA2**

Figure 80 shows the result of the first modelling case where the zone ZFMA2 is activated with realization DFN03v. The hypocentre of earthquake is marked by a star, and the simulated magnitude is M3.93. From the colour coding of the shear displacement of the joint planes and scaling of the seismic events, one can see that many of the seismic events take place at DZ-DZ intersections, where gently dipping zones are connected to a steeply dipping zone. None of the TFs is showing shear displacement larger than 50 mm (Figure A3-118).

Results of another modelling case with realization DFN06v are provided in Appendix 3 (Figure A3-122 to A3-126). Similar results are found, where a few of the TFs are showing displacement larger than 50 mm, but can be regarded as outliers.

### **6.4.2. Earthquake at zones ZFMA2-A3-A8-F1**

Figure 81 shows the result of the second modelling case where the multiple DZs are activated at the same time with realization DFN06v. The figure shows a distinct difference compared to Figure 80. The hypocentre is located at the middle of the activated zones and the simulated magnitude is M5.26, which is larger than that of previous modelling case on vertical sections due to the increased length of the activated zones. One TF is showing a shear displacement larger than 50 mm (Figure A3-128), but the analysis by a box-and-whisker diagram indicates that that can be regarded as an outlier (Figure A3-129).

### **6.4.3. Earthquake at zones ZFMA2-A3-A8-F1, powered shear force**

Figure 82 is the result of the third modelling case where the multiple DZs are activated at the same time with realization DFN06v, and the shear force on the smooth joints are powered by a factor of 10. Similar to the previous modelling case, the hypocentre is in the middle of the activated DZs, but the simulated magnitude is 5.63. A few of the TFs are showing shear displacement larger than 50 mm (Figure A3-133). The analysis by a box-and-whisker diagram indicates that 3 TFs in the length class 2 are showing shear displacement below the 95th percentile, and therefore cannot be regarded as outliers (Figure A3-134).

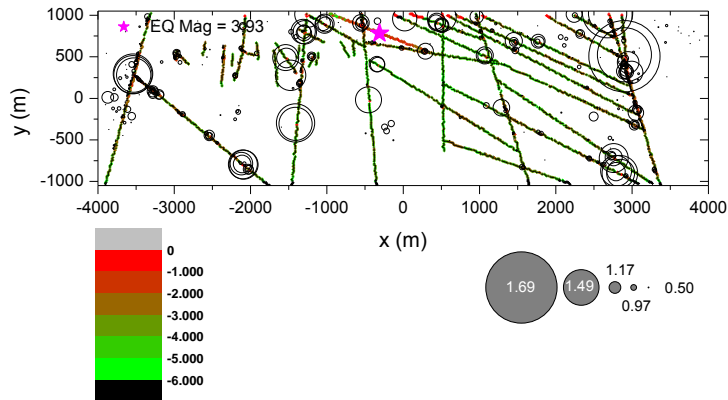


**Figure 80.** Spatial distribution of the induced seismic events and shear displacement of the smooth joints that constitute the TFs and DZs, due to earthquake at zone ZFMA2 with realization DFN03v (Figure A3-117).

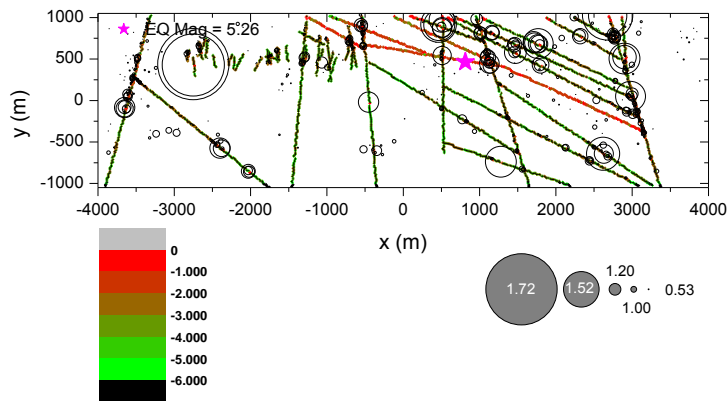


**Figure 81.** Spatial distribution of the induced seismic events and shear displacement of the smooth joints that constitute the TFs and DZs, due to earthquake at zones ZFMA2-A3-A8-F1 with realization DFN06v (Figure A3-127).

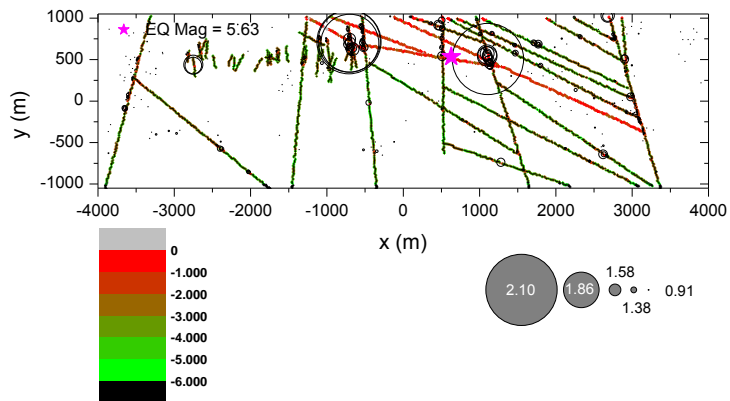


**Figure 82.** Spatial distribution of the induced seismic events and shear displacement of the smooth joints constituting the TFs and DZs, due to earthquake at zone ZFMA2-A3-A8-F1, with powered shear force and with realization DFN06v (Figure A3-132).

## 6.5. Earthquake at selected deformation zones – glacial induced stress field at time of maximum ice cover – Vertical section model

This section deals with two modelling cases of earthquake under glacial induced stress field at time of maximum thickness of ice cover during future glacial period. An activated zone ZFMA2 was modelled. Two cases with multiple deformation zones were also studied. The first case assumes that multiple deformation zones, ZFMA2, ZFMA3, ZFMA8 and F1, are activated at the same time. The second case deals with powering up the shear force on the joints in the earthquake hosting multiple deformation zones to simulate larger magnitude earthquake. For two modelling cases with realization DFN03v and DFN06v were carried out.

### 6.5.1. Earthquake at zone ZFMA2

The seismic event modelled for ZFMA2, the induced stress field at time of maximum ice cover results and with realization DFN03v results in a magnitude of M3.9. The shear displacements of the joint planes of the TFs are below 10 mm (see Figure A3-137 to A3-141).

### 6.5.2. Earthquake at zones ZFMA2-A3-A8-F1

Figure 83 is the result of the seismic events and shear displacements of the joint planes of the TFs and DZs. The hypocentre is in the middle of the activated DZs and the simulated magnitude is M5.35. The simulated magnitude is a slightly higher than the magnitude simulated under the present-day reverse stress field and multiple zones. This is due to that fact that the stresses are higher due to the loading of the ice cover. Therefore the amount of the strain energy stored at the zones and released is larger than it was under the present-day stress field. One TF is showing a shear displacement larger than 50 mm (Figure A3-143), but the analysis with the box-and-whisker diagram indicates that it can be regarded as an outlier (Figure A3-144).

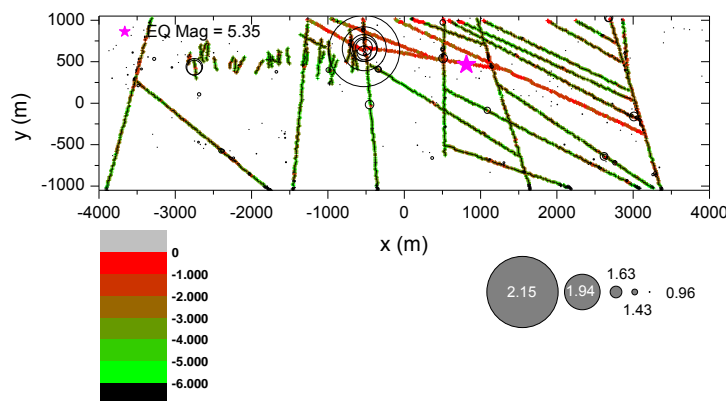


**Figure 83.** Spatial distribution of the induced seismic events and the shear displacement of the smooth joints that constitute the TFs and DZs, due to earthquake at zone ZFMA2, ZFMA3, ZFMA8 and F1 with realization DFN06v (Figure A3-142).

### 6.5.3. Earthquake at zones ZFMA2-A3-A8-F1, powered shear force

Figure 84 is the result of the modelling case where multiple zones are activated at the same time, and shear force on the smooth joints are powered by a factor of 10. Similarly to the previous case, the hypocentre is in the middle of the activated DZs, and the simulated magnitude is M5.91, which is also larger than before due to the larger strain energy stored at the zones by higher level of glacially induced stresses. A few of the TFs are showing shear displacement larger than 50 mm (Figure A3-148). Analysis by a box-and-whisker diagram indicates that 3 TFs are showing shear displacements larger than 50 mm that are below the 95th percentile (Figure A3-149) and cannot be regarded as outliers.

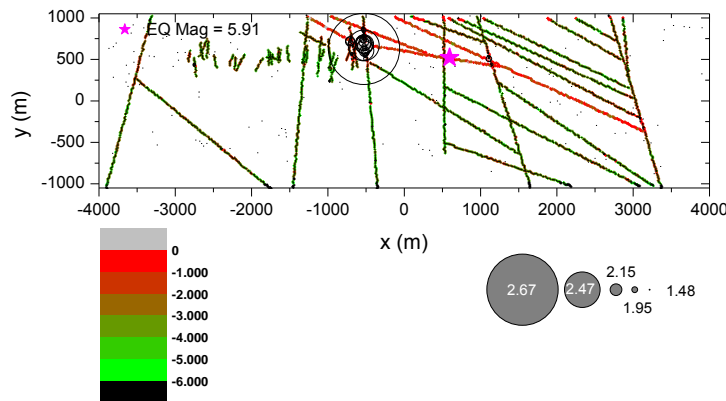


**Figure 84.** Spatial distribution of the induced seismic events and the shear displacement of the smooth joints that constitute the TFs and DZs, due to earthquake at zone ZFMA2-A3-A8-F1, with powered shear force and with realization DFN06v (Figure A3-147).

## 6.6. Earthquake at selected deformation zones – glacial induced stress field at time of ice retreat – Vertical section model

In this section, two modelling cases are compared where the multiple zones ZFMA2, ZFMA3, ZFMA8 and F1 are activated under the glacial induced stress field at time of ice cover retreat during a future glacial period. A case without and one with “powered shear force” on the joints are presented, hence two different magnitudes of earthquake are obtained for the same deformation zones and realization DFN06v. More modelling cases for ZFMA2, the multiple zones and realization DFN03v can be found in Appendix 3.

### 6.6.1. Earthquake at zone ZFMA2

The seismic event modelled for ZFMA2, the induced stress field at time of ice retreat results and with realization DFN06v results in a magnitude of M4.07. The 95th percentile of the shear displacements of the joint planes of the TFs is below the canister damage threshold of 50 mm (see Figure A3-137 to A3-141).

### 6.6.2. Earthquake at zones ZFMA2-A3-A8-F1

Figure 85 shows the seismic events and shear displacements of the joint planes of the TFs and DZs. The hypocentre is in the middle of the activated DZs. For the case of ice retreat, the simulated magnitude is M5.43, which is slightly larger than the simulated magnitude in the case of maximum ice cover (M5.35). This is due to the fact that the glacial induced stresses at the time of ice retreat are more anisotropic due to reduced vertical stress that leads to higher degree of reverse faulting. The largest magnitude of the co-seismic event is M2.13. None of the TFs is showing shear displacement larger than 50 mm (Figure A3-163 and A3-164).

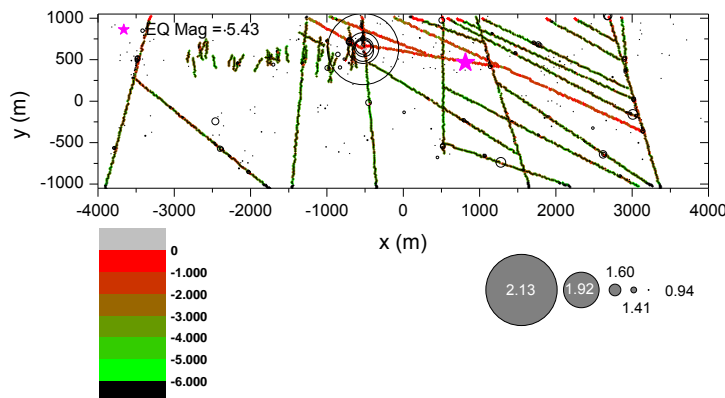


**Figure 85.** Spatial distribution of the induced seismic events and the shear displacement of the smooth joints that constitute the TFs and DZs, due to earthquake at zone ZFMA2-A3-A8-F1 with realization DFN06v (Figure A3-162).

### 6.6.3. Earthquake at zones ZFMA2-A3-A8-F1, powered shear force

Figure 86 shows the seismic events and shear displacements of the joint planes of the TFs and DZs by activation of multiple zones with shear force on the joint planes powered by a factor of 10. Similarly to the previous modelling case, the hypocentre is in the middle of the activated DZs, and the simulated magnitude is M5.73. Shear displacement of the TFs is analysed by a box-and-whisker diagram and shows that the shear displacements exceeding 50 mm can be regarded as outliers (Figure A3-174).

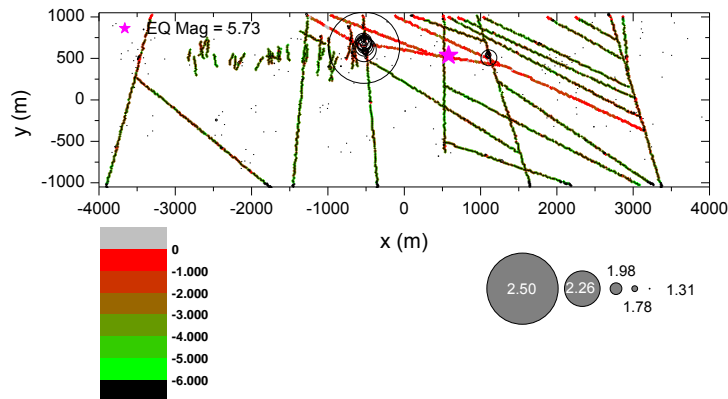


**Figure 86.** Spatial distribution of the induced seismic events and the shear displacement of the smooth joints that constitute the TFs and DZs, due to earthquake at zone ZFMA2-A3-A8-F1, with powered shear force and with realization DFN06v (Figure A3-172).

## 6.7. The Consultants' assessment

Shear displacements of the target fractures and deformation zones are plotted with respect to their length and compared with the regressions by Wells and Coppersmith (1994) and Leonard (2010). The modelled earthquakes on host deformation zones show fairly good match with the regressions in terms shear displacements for activated lengths for both the horizontal and the vertical section models.

In all modelling cases, there is a number of target fractures showing shear displacement exceeding the canister damage threshold of 50 mm. A box-and-whisker diagram is applied to the data sets as a way for non-parametric assessment.

From the results of the modelling cases with the horizontal section model, the risk of canister damage due to shearing of the target fractures is expected when the zones ZFMWNW0001 and ZFMWNW2225 are activated under the present-day “most likely” stress field and the glacially induced stress field at the time of forebulge. Target fractures are more prone to shear under the glacial induced stress field. This is due to the fact the stress field at the time of forebulge becomes more anisotropic due to the reduction of the minimum horizontal stress  $S_h$  from 22 MPa to 17 MPa.

Figure 87 shows the relation between the simulated earthquake moment magnitudes and the target fracture shear displacements (maximum and 95th percentile values). Generally, it is observed that the shear displacement of target fractures is generally independent on the earthquake magnitude lower than  $M_w$  5. When the magnitude is larger than  $M_w$  5, both the maximum and the 95th percentile values are showing an increasing trend with the earthquake magnitude. Shear displacements that corresponds to the 95th percentile are under the canister damage threshold of 50 mm when the seismic event magnitude is below about  $M_w$  5.5. This implies that when an earthquake with magnitude larger than  $M_w$  5.5 occurs, the risk of canister damage due to the shearing of target fractures can be expected. This is in agreement with SKB's results in Fälvh et al. (2010).

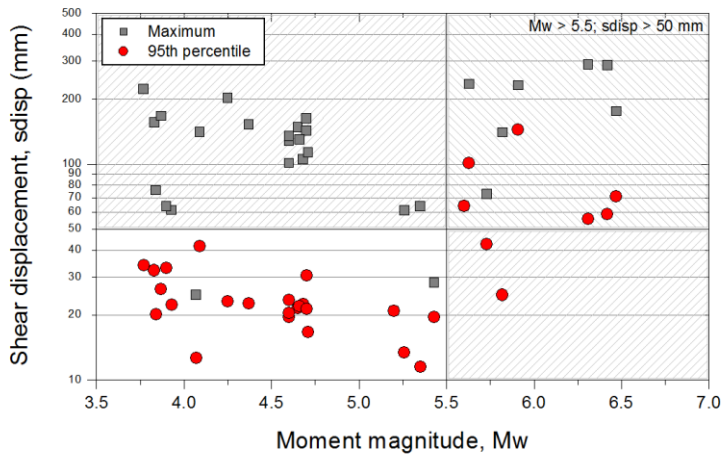


**Figure 87.** Relation between the moment magnitudes  $M_w$ , and the maximum and the 95th percentile of the average value of shear displacement on target fractures for earthquakes modelled with PFC.

## 7. Modelling of target fracture responses to simultaneous earthquake and heating of the repository

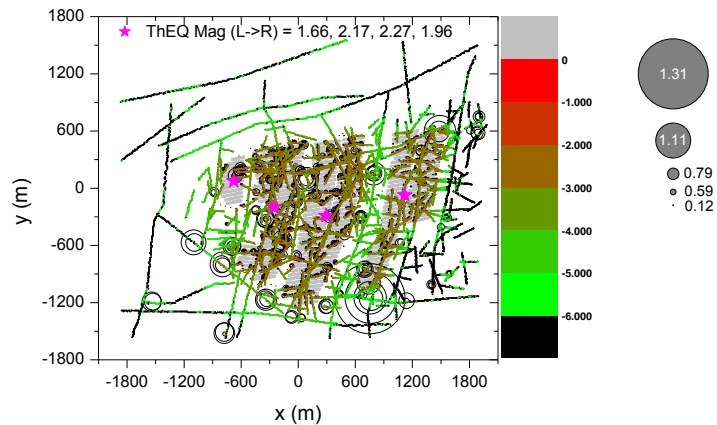
This section deals with two modelling cases where an earthquake takes place on a deformation zone after 50 years of sequential heating of the repository rock mass. For the earthquake generation, two deformation zones, ZFMWNW0809A and ZFMWNW2225, are chosen as they are estimated to be unstable under the present-day “most likely” reverse stress field by SKB. Zone ZFMWNW0809A is the longest in Forsmark local geological model while zone ZFMWNW2225 poses the largest threat as it cuts across three deposition panels in the repository. Target fractures and deformation zones are shortened with “TFs” and “DZs”, respectively, in the following.

### 7.1. Earthquake at ZFMWNW0809A after 50 years of sequential heating – present-day “most likely” stress field – horizontal section model

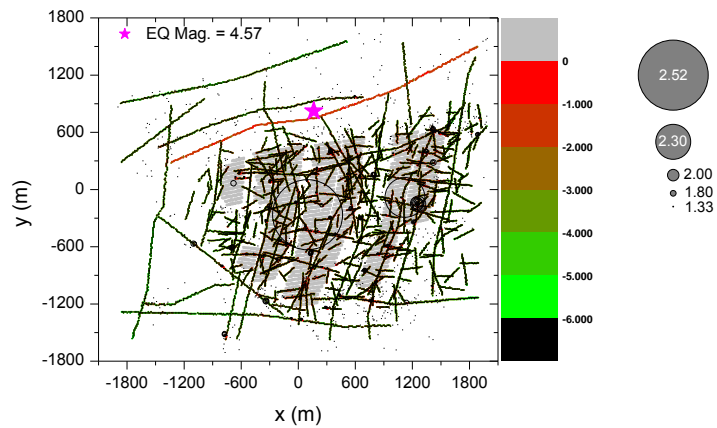
This modelling case assumes that an earthquake takes place at deformation zone ZFMWNW0809A after 50 years of sequential heating of the repository rock mass.

Figure 88 appears similar to Figure 47, as both show similar spatial distributions of thermal induced co-seismicity from the start of deposition to 50 years of sequential heating. However, there is a slight difference due to the fact that the zone ZFMWNW0809A has been locked during the 50 years of sequential heating in the model in Figure 88. No bond breakages were allowed on the smooth joints that constitute the host zone. The maximum co-seismic event of magnitude M1.31 is however comparable with the maximum co-seismic event of magnitude M1.25 resulting when the bond breakages on the host zone are allowed (see Sec. 5.2).

Figure 89 shows the co-seismic events induced by activation of the earthquake at the host zone ZFMWNW0809A (M4.57) after 50 years of sequential heating. By the colour of joint segments of TFs and DZs, it can be clearly seen that an earthquake at ZFMWNW0809A results in a significant increase in shear displacement of TFs and DZs compared with the case of 50 years of sequential heating only. It should be also noted that the largest co-seismic events takes place within the repository footprint and has a magnitude almost double (M2.52) compared with largest magnitude of thermally induced events observed during 50 years of sequential heating (M1.31). However, this magnitude is rather close to that of the largest co-seismic event due to activation of zone ZFMWNW0809A without heating of the repository (M1.81, see Sec. 6.1.1). Also the magnitude of the triggering earthquake is almost the same in the two cases.



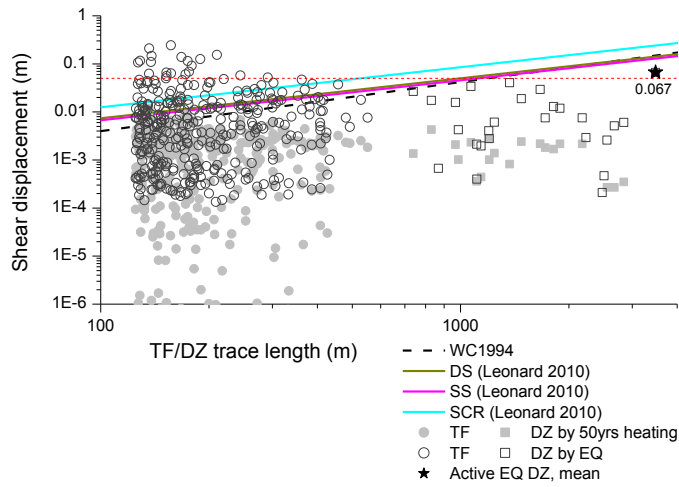
**Figure 88.** Spatial distribution of the induced co-seismic events and shear displacements of the smooth joints that constitute the TFs and DZs after 50 years of sequential heating with realization DFN03h (Figure A3-177).



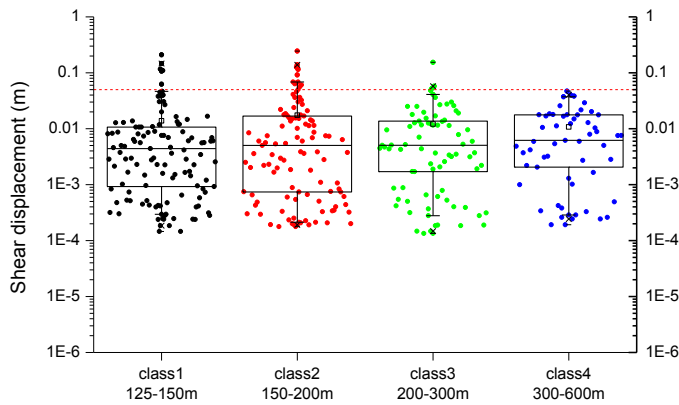
**Figure 89.** Spatial distribution of the induced co-seismic events and shear displacements of the smooth joints that constitute the TFs and DZs due to an earthquake at zone ZFMWNW0809A after 50 years of sequential heating with realization DFN03h (Figure A3-178).

Figure 90 shows the shear displacement of the TFs and DZs with respect to their length that are observed after 50 years of sequential heating (grey dots) and after activation of an earthquake at zone ZFMWNW0809A after 50 years of sequential heating (open black dots). It can be clearly seen that activation of the earthquake significantly increases the shear displacement of TFs with maximum increase up to two orders of magnitude, on average from  $10^{-6}$  m to  $10^{-4}$  m.

Figure 90 also shows that 50 years of heating do not result in shear displacement of any of the TFs exceeding the canister damage threshold. However, after earthquake activation during heating, as seen in the box-and-whisker diagram in Figure 91, there are quite a number of TFs, in particular in trace length between 150 and 200 m, that exceeds the canister damage threshold 50 mm and cannot be regarded as outliers.



**Figure 90.** Shear displacement of the TFs and DZs by 50 years of heating (grey dots) and by an earthquake at zone ZFMWNW0809A superposed to heating (open black dots) and comparison with empirical regressions (Figure A3-179).



**Figure 91.** Shear displacement of the TFs induced by an earthquake at zone ZFMWNW0809A after 50 years of sequential heating, divided into four trace length classes (Figure A3-180).

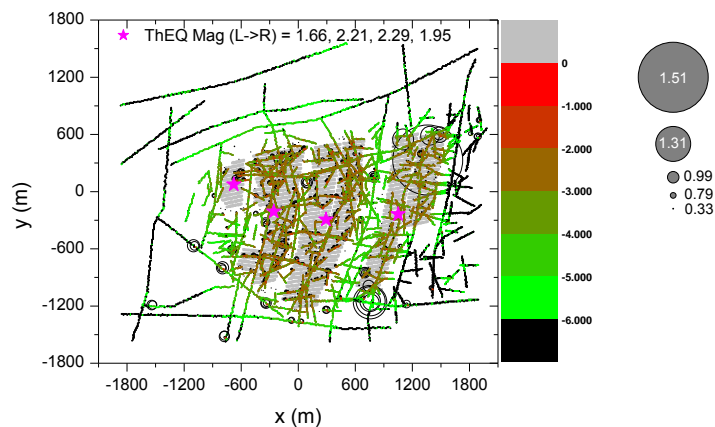
The total number of TFs of which the shear displacement exceeds the 50 mm threshold is 20, and 5 of them cannot be regarded as outliers. For the case of an earthquake on ZFMWNW0809A without heating, the data points above the canister damage threshold are all larger than the 95th percentile, and could therefore be regarded as outliers (see Sec. 6.1.1).

## 7.2. Earthquake at ZFMWNW2225 after 50 years of sequential heating – present-day “most likely” stress field – horizontal section model

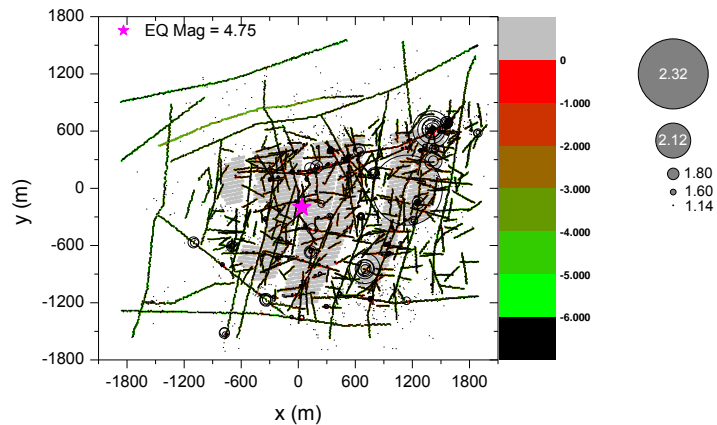
This modelling case assumes that an earthquake takes place at zone ZFMWNW2225. Figure 92 shows the thermally induced events after 50 years of heating, showing four equivalent hypocentres located at the centres of each sequentially heated panel, which is similar to the previous modelling case. The largest magnitude event takes place at upper corner of the panel D area with magnitude of M1.51. Relatively large shear displacement are shown for the TFs that are within the repository footprint (reddish green, greenish red colour in the figure) and TF and some part of DZs outside of the repository footprint are showing relatively small displacement (green).

Figure 93 shows the seismic events induced by an earthquake at zone ZFMWNW2225. Unlike in the previous modelling case, seismic activation of zone ZFMWNW2225 after 50 years of sequential heating of the repository results in a large magnitude of M4.75. It should be noted that the magnitude of the earthquake without the sequential heating of the repository was M3.77 (see Sec. 6.1.3). Heating of the repository has the effect of powering the seismic moment of about one order of magnitude. Similarly to the previous modelling case, comparing the colour of joint segments of TFs and DZs, it is clearly seen that earthquake activation at zone ZFMWNW2225 results in significant increase in shear displacement of the TFs and DZs.

The triggering of the earthquake on zone ZFMWNW2225 induce several other simultaneous events across the heated repository, therefore the equivalent hypocentre is not placed on the zone in Figure 93. Unlike in previous modelling case, the earthquake hypocentre is shifted from the trace of zone ZFMWNW2225 to the centre of the panel A, B and C. This implies that activation of the zone ZFMWNW2225 during the repository heating poses that largest threat as the largest magnitude hypocentre is shifted towards the centre of the repository.



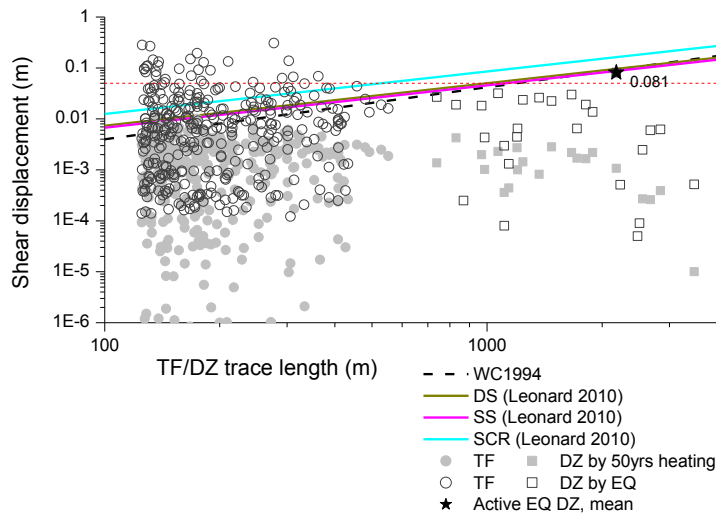
**Figure 92.** Spatial distribution of the induced seismic events and shear displacement of the smooth joints that constitute the TFs and DZs after 50 years of sequential heating with realization DFN03h (Figure A3-183).



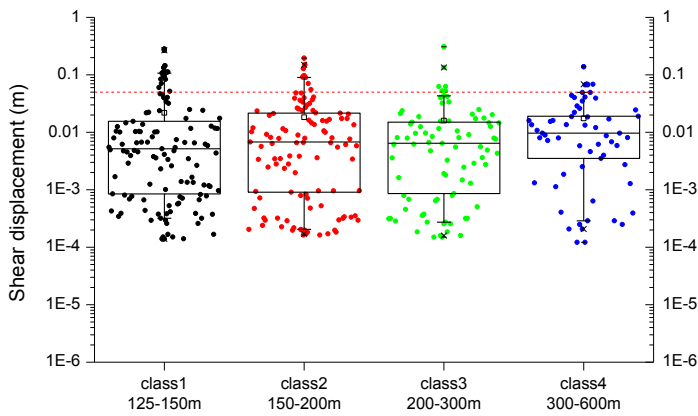
**Figure 93.** Spatial distribution of the induced co-seismic events and shear displacement of the smooth joints that constitute the TFs and DZs due to an earthquake at zone ZFMWNW2225 after 50 years of sequential heating with realization DFN03h (Figure A3-184).

Figure 94 also shows the shear displacement of the TFs and DZs with respect to their length that are observed after 50 years of sequential heating (grey dots) and after activation of an earthquake superposed to heating (open black dots). The activation of earthquake significantly increases the shear displacements. However, unlike in previous modelling case, some of the DZs are showing reduction in amount of shear displacement due to the earthquake. Such observations might be due to the reverse direction of shear displacement of the DZs due to the earthquake activation. The figure also shows that 50 years of heating do not result in shear displacement of any of the TFs exceeding the canister damage threshold. However, after earthquake activation, as seen in the box-and-whisker diagram in Figure 95, there are quite a number of TFs, in particular with trace length between 125 and 200 m (class 1 and class 2), that exceed the canister damage threshold of 50 mm and cannot be regarded as outliers. The total number of the TFs of which the shear displacement exceed the 50 mm threshold is 29, and 10 of them cannot be regarded as outliers.

The results for the seismic activation of zone ZFMWNW2225 without heating gives a few data points are exceeding 50 mm, but these were above the 95th percentile and could be regarded as outliers (see Sec. 6.1.3).



**Figure 94.** Shear displacement of the TFs and DZs by 50 years of heating (grey dots) and by an earthquake at zone ZFMWNNW2225 superposed to heating (open black dots) and comparison with empirical regressions (Figure A3-185).



**Figure 95.** Shear displacement of the TFs induced by an earthquake at zone ZFMWNNW2225 after 50 years of sequential heating, divided into four trace length classes (Figure A3-186).

### 7.3. The Consultants' assessment

Shear displacement of the target fractures and deformation zones are plotted with respect to their length and compared with the regressions by Wells and Copper-Smith (1994) and Leonard (2010). Figure 90 and 94 contain two sets of data; (i) shear displacement of target fractures and deformation zones induced by 50 years of sequential heating, (ii) shear displacement of target fractures and deformation zones induced by an earthquake superposed to 50 years of sequential heating. The first data sets (grey dots) show that all the target fractures are undergoing shear displacement lower than 10 mm. However, the latter shows that the earthquake activation during heating significantly increases the shear displacement, i.e. up to two orders of magnitude. The box-and-whisker diagrams show that many of the target fractures of trace length between 125 and 200 m undergo shear displacement larger than the canister damage threshold 50 mm and cannot be regarded as outliers. Compared to the earthquake only induced modelling cases, these two cases where an earthquake takes place while the target fractures are undergoing thermally induced movement poses the greatest risk of canister damage.

Comparing these two cases, it can be concluded that the level of risk of canister damage is higher in case an earthquake takes place at zone ZFMWNW2225 (i.e. 10 target fractures show shear displacements larger than 50 mm and cannot be regarded as outliers), than an earthquake at zone ZFMWNW0809A (i.e. 5 target fractures show shear displacement larger than 50 mm that cannot be regarded as outliers). On the other hand, all the shear displacements on target fractures obtained from the models with an earthquake at zone ZFMWNW2225 or ZFMWNW0809A without heating, although larger than 50 mm, could be regarded as outliers.

Observations made from the horizontal section models motivate the necessity of investigating also the vertical section model, where the effects of heating and earthquake occurring at a single and multiple gently dipping deformation zones can be studied.

Vertical section models were not conducted here. This is due to fact that it is difficult to estimate the number of equivalent heat source particles along a vertical profile of the candidate area. In the vertical section model, the thickness in out-of-plane direction is 1 m and poses the problem of under-estimating the total heat energy. Therefore, this modelling case requires a careful planning and it is suggested as a further research topic, in particular by means of 3D modelling.



## 8. Discussion

Table 12 lists the key results of the 38 PFC2D modelling cases in this study.

Those modelling cases where the risk of canister damage can be expected, i.e. where some of the target fractures undergo shear displacements larger than 50 mm and cannot be regarded as outliers (i.e. smaller than the 95<sup>th</sup> percentile), are shown by means of shaded cells in the table. The columns in the table are as follows:

- *Column A*: Loading conditions (Thermal induced; Earthquake; Thermal and earthquake) and model type (horizontal section model; vertical section model) and time period of modelling (Operation < 1000 years; Present day; Glacial period at time of forebulge; Glacial period at time of maximum thickness of ice cover; Glacial period at time of ice retreat);
- *Column B*: Key variations of loading (Sim: Simultaneous heating; Seq: Sequential heating; Earthquake hosting deformation zone; Discrete fracture network; with powering shear force enabled or disabled);
- *Column C*: Moment magnitude  $M_w$  of the earthquake at the host deformation zone when assuming full out-of-plane size (i.e. equal to the trace length of the zone);
- *Column D*: Total number of target fractures;
- *Column E*: Number of target fractures where the shear displacement exceeds the canister damage threshold of 50 mm, for each trace length class, i.e. class 1/2/3/4 for horizontal section model, and class 1/2 for vertical section model, respectively;
- *Column F*: Number of target fractures where the shear displacement exceeds the 95th percentile of the shear displacement, for each trace length class, i.e. class 1/2/3/4 for horizontal section model, and class 1/2 for vertical section model, respectively;
- *Column G*: Number of target fractures where the shear displacement exceeds the canister damage threshold of 50 mm, but is less than the 95th percentile shear displacement, for each trace length class, i.e. class 1/2/3/4 for horizontal section model, and class 1/2 for vertical section model, respectively;
- *Column H*: Maximum shear displacement (mm) of the target fractures observed for each trace length class, i.e. class 1/2/3/4 for horizontal section model, and class 1/2 for vertical section model;
- *Column I*: Shear displacement of the target fracture (mm) that corresponds to the 95th percentile for each trace length class, i.e. class 1/2/3/4 for horizontal section model, and class 1/2 for vertical section model, respectively.

**Table 12.** Summary of the key results of the 38 modelling cases in this study.

	A	B	C	D	E	F	G	H	I
THERMAL – HORIZONTAL SECTION	Operation (< 1000 yrs)	Sim; DFN03h	2.27	346	0	0	0	8	5
			2.16		0	6	0	10	6
			2.15		0	4	0	5	5
			1.64		0	3	0	5	4
		Sim; DFN06h	2.23	271	0	4	0	7	6
			2.21		0	4	0	7	5
			2.17		0	4	0	6	4
			1.60		0	3	0	4	3
		Seq; DFN03h	2.26	346	0	6	0	12	4
			2.17		0	6	0	10	6
			1.96		0	4	0	7	4
			1.66		0	3	0	6	4
		Seq; DFN06h	2.25	271	0	4	0	12	5
			2.19		0	4	0	12	6
			1.66		0	4	0	8	4
			1.64		0	3	0	4	3
EARTHQUAKE – HORIZONTAL SECTION	Present-day "most likely" stress	ZFMWNNW0809A; DFN03h	4.60	346	3	6	0	111	18
					4	6	0	128	47
					0	4	0	34	19
					0	3	0	36	12
		ZFMWNNW0809A; DFN06h	4.65	271	4	4	0	148	26
					4	4	0	139	35
					0	4	0	46	20
					1	3	0	58	18
		ZFMWNNW0001; DFN03h; powered shear force	6.31	346	6	6	0	289	53
					13	6	7	168	81
					2	4	0	100	42
					1	3	0	54	38
		ZFMWNNW0001; DFN06h; powered shear force	5.82	271	3	4	0	131	26
					3	4	0	140	25
					2	4	0	70	21
					1	3	0	98	24
		ZFMWNNW2225; DFN03h	3.77	346	4	6	0	222	27
					4	6	0	131	39
					0	4	0	38	22
					2	3	0	78	38
		ZFMWNNW2225; DFN06h	3.83	271	2	4	0	156	33
					5	4	1	137	84
					1	4	0	60	19
					1	3	0	72	18
Glacial period, forebulge	ZFMWNNW0809A; DFN03h	4.70	346	5	6	0	113	48	
				5	6	0	143	46	
				0	4	0	42	14	
				0	3	0	17	10	
	ZFMWNNW0809A; DFN06h	4.68	271	2	4	0	71	28	
				3	4	0	105	32	
				0	4	0	44	21	
				1	3	0	69	18	
	ZFMWNNW0001; DFN03h; powered shear force	6.42	346	6	6	0	185	47	
				13	6	7	288	74	
				4	4	0	96	47	
				1	3	0	66	31	
	ZFMWNNW0001; DFN06h; powered shear force	6.47	271	4	4	0	162	41	
				9	4	5	176	97	
				5	4	1	102	63	
				5	3	2	114	63	
	ZFMWNNW2225; DFN03h	4.09	346	5	5	0	111	50	
				8	6	2	141	60	
				0	4	0	44	17	
				0	3	0	50	23	
	ZFMWNNW2225; DFN06h	4.37	271	2	4	0	76	15	
				5	4	1	152	68	
				0	4	0	23	12	
				0	3	0	46	17	

Table 12. Cont. Summary of the key results of the 38 modelling cases in this study.

A		B	C	D	E	F	G	H	I		
A	Glacial period, max ice cover	ZFMNW1200; DFN03h	4.25	346	5 4 0 0	6 6 4 3	0 0 0 0	118 203 28 17	31 46 16 12		
		ZFMNW1200; DFN06h	4.60	271	2 3 0 1	4 4 4 3	0 0 0 0	68 101 21 69	6 41 10 19		
		ZFMWNW0809A; DFN03h	4.71	346	5 1 1 0	6 6 4 3	0 0 0 0	113 68 110 44	26 12 20 8		
		ZFMWNW0809A; DFN06h	4.66	271	2 3 0 2	4 4 4 3	0 0 0 0	59 130 46 69	8 42 15 20		
		ZFMWNW2225; DFN03h	3.84	346	3 2 2 1	6 6 4 3	0 0 0 0	57 76 52 55	22 17 19 14		
		ZFMWNW2225; DFN06h	3.88	271	1 4 0 1	4 4 4 3	0 0 0 0	55 167 46 55	15 63 15 26		
		ZFMNW1200; DFN03h	4.60	346	3 2 1 0	6 6 4 3	0 0 0 0	85 68 135 44	20 24 13 16		
		ZFMNW1200; DFN06h	4.70	271	1 2 0 1	4 4 4 3	0 0 0 0	163 129 46 69	4 27 14 20		
		EARTHQUAKE – VERTICAL SECTION	Present day	ZFMA2; DFN03v	3.93	16	0 0	1 1	0 0	9 9	9 9
				ZFMA2; DFN06v	3.93	31	0 1	1 1	0 0	16 61	11 36
				ZFMA2-A3-A8-F1; DFN06v	5.26	31	0 1	1 1	0 0	13 61	9 30
				ZFMA2-A3-A8-F1; DFN06v; powered shear force	5.63	31	1 3	1 1	0 2	101 235	31 141
			Glacial period, max ice cover	ZFMA2; DFN06v	3.90	31	0 1	1 1	0 0	5 64	4 44
				ZFMA2-A3-A8-F1; DFN06v	5.35	31	0 1	1 1	0 0	10 64	7 30
ZFMA2-A3-A8-F1; DFN06v; powered shear force	5.91			31	2 3	1 1	1 2	145 231	71 149		
Glacial period, ice retreat	ZFMA2; DFN06v			4.07	31	0 0	1 1	0 0	5 25	3 17	
	ZFMA2-A3-A8-F1; DFN03v		5.20	16	0 0	1 1	0 0	21 9	18 8		
	ZFMA2-A3-A8-F1; DFN06v		5.43	31	0 0	1 1	0 0	11 28	7 23		
	ZFMA2-A3-A8-F1; DFN03v; powered shear force		5.60	16	1 0	1 1	0 0	64 10	46 9		
	ZFMA2-A3-A8-F1; DFN06v; powered shear force		5.73	31	1 0	1 1	0 0	73 43	36 40		
	T+EQ (H)		Operation (<1000 yrs)	Seq; ZFMWNW0809A; DFN03h	4.57	346	6 11 3 0	6 6 4 3	0 5 0 0	210 244 154 47	52 68 43 38
Seq; ZFMWNW2225; DFN03h				4.75	346	14 8 4 3	6 6 4 3	8 2 0 0	282 195 308 138	108 88 45 56	

From the results of three modelling campaigns, the Authors summarize observations, provide interpretations of the results and discuss the implications for the long-term safety of the repository at Forsmark.

- 1) For all the earthquake modelling cases, the shear displacements of the deformation zones hosting an earthquake match well the regressions as a function of the fault length presented in the literature (e.g. Wells and Coppersmith, 1994; and Leonard, 2010). This validates the modelling schemes of generic earthquakes against the case histories in the regression databases in terms of length and displacement of the faults or deformation zones.

Figure 96 shows the relationship between the rupture area  $RA$  of the earthquake hosting deformation zones and the average shear displacement  $D_{av}$ . Two lines are provided by Leonard (2010) that represent the upper and lower limits of the shear displacement, taking into account of the uncertainty of the parameters of the regressions:

$$\text{Upper limit: } \log(D_{av}) = 0.5 \log(RA) - 3.92$$

$$\text{Lower limit: } \log(D_{av}) = 0.5 \log(RA) - 4.82 \quad \text{Eq. (8-1)}$$

The figure shows that most of the data points resulting from the numerical modelling are distributed within the uncertainty range. In all cases, an out-of-plane width of the deformation zones is assumed to be as large as their trace length, except for those marked by grey stars. Those data points correspond to the modelling cases of the zone ZFMWNW0001 (Singö deformation zone), where the truncated trace length of the zone (2476 m) rather than its full length is activated by powering the shear force on the forming joint elements. Therefore, it is reasonable to assume that a longer trace of zone ZFMWNW0001 is in reality activated. It is assumed that the rupture area of this zone is larger than the numerical model and equal to 205.7 km<sup>2</sup> (from Backers et al., 2014). Even with this makeshift, the simulated shear displacements still exceed the upper uncertainty limit by Leonard (2010).

Figure 97 shows another relationship between the rupture area  $RA$  and the moment magnitudes  $M_w$  of the activated earthquakes. The plotted moment magnitudes correspond to the seismic moments of the full size deformation zones (with out-of-plane width equal to the trace length). It shows that most of the data points are distributed within the range  $\pm 3$  standard deviations ( $\pm 3\sigma$ ) around the mean value from the regression by Wells and Coppersmith (1994):

$$M_w = 4.07 + 0.98 \log(RA) \quad \text{Eq. (8-2)}$$

Here,  $\pm 3\sigma$  is the uncertainty range adopted as the trace length and the width of the deformation zones may have large variation.

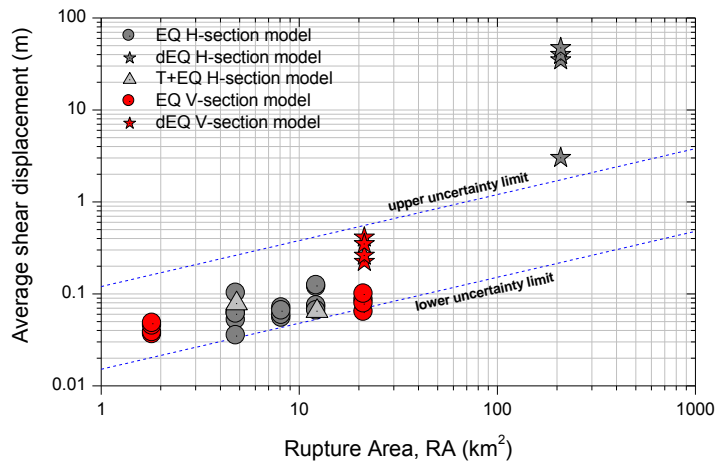


**Figure 96.** Relation between the simulated rupture area of a deformation zones hosting an earthquake and the simulated shear displacement (average). The uncertainty limits of the regression by Leonard (2010) are indicated.

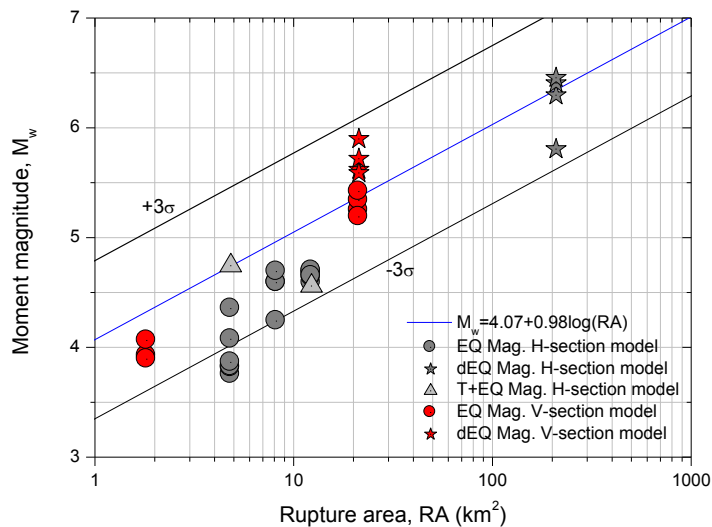


**Figure 97.** Relation between rupture area  $RA$  of the earthquake hosting deformation zones and the moment magnitudes  $M_w$  of the simulated earthquakes. The uncertainty range  $\pm 3\sigma$  from the mean value of the regression by Wells and Coppersmith (1994) is indicated.

- 2) The stability of the deformation zones is estimated by means of the Coulomb Failure Stress  $CFS$  analysis as in Sec. 4.7. For each of the stress models, unstable deformation zones are identified and few of them are compared with SKB's estimates. This includes ZFMWNW0809A, ZFMNW1200, ZFMWNW0123, ZFMENE0062A, and ZFMENE0060A. From the  $CFS$  analysis, the last two deformation zones (ZFMENE0062A, ZFMENE0060A) are found to be stable, which agrees with SKB's evaluation (Fälth and Hökmark, 2010).

- 3) From the modelling of the heating of the repository, it is found that, not only the target fractures, but also some deformation zones can undergo shearing due to the heating from the spent nuclear fuel. For the modelling case with heating from simultaneous deposition of the fuel canisters, it is found that the deformation zones that are under stable state (striking NE-SW) can undergo shearing and interact with the deformation zones under unstable state (striking NW-SE), which results in co-seismic events in particular at their intersections.
- 4) From the modelling of the earthquake occurrence for the present-day stress field, it is found that the occurrence of earthquake at zone ZFMWNW0809A (beyond the repository footprint) can trigger seismic events (e.g. secondary earthquakes) at zone ZFMNW1200, which is located at the opposite side of the repository. In case zone ZFMWNW2225 is activated, the induced co-seismic events tend to concentrate along the earthquake hosting deformation zone. This result seems reasonable as this zone intersects many other fractures and deformation zones; when the strain energy stored in it is released, the nearby fractures and deformation zones are likely to absorb most of the energy by means of movements. As consequence, such concentrated pattern of shear displacements along and near the earthquake hosting deformation zone results in many local co-seismic events. Concerning the repository safety, the occurrence of an earthquake at zone ZFMWNW2225 tends to pose the largest risk as this zone is located within the footprint of the repository. One can argue that the trace of the zone in the PFC model was, for practical reasons, elongated by 35% (Table 1) compared to the geological evidences, and this might enhance criticality. The additional length of about 500 m falls into the length range for the fractures included in the DFNs (125-600 m). Therefore, a random fracture with a length of about 500 m and with unfortunate location and orientation could link to zone ZFMWNW2225 and produce the effect highlighted by the modelling. The case of an elongated zone, which cannot be ruled out, serves here as a conservative case and deserves attention.
- 5) From the modelling of glacially induced earthquakes, it is found that there is high probability that zone ZFMWNW2225 is triggered by the earthquake at zone ZFMNW1200. Secondary earthquakes, i.e. triggered co-seismic events along and near the zone ZFMWNW2225, tend to show much higher intensity and frequency under the glacially induced stress field that corresponds to the time when the minimum horizontal stress is reduced due to forebulge ahead of the ice cover.
- 6) In this report, the values of shear displacements on target fractures are treated as the outcomes of a stochastic variable of which the 95<sup>th</sup> percentile is calculated. Values of the shear displacement exceeding the values of the 95<sup>th</sup> percentile are considered as outliers and not included in the count of the critical positions. This is done to take into account possible local magnification effects and numerical singularities in the PFC models.

Concerning the occurrence of the shear displacements exceeding the threshold for canister damage of 50 mm, it is recommended to further investigate where in the models the values that cannot be regarded as outliers are located. SKB states that no canister depositions will be allowed within 100 m from the traces of deformation zones longer than 3 km. However, the risk of canister damage would be reduced if the target fractures within the respect distance from even smaller zones than 3 km

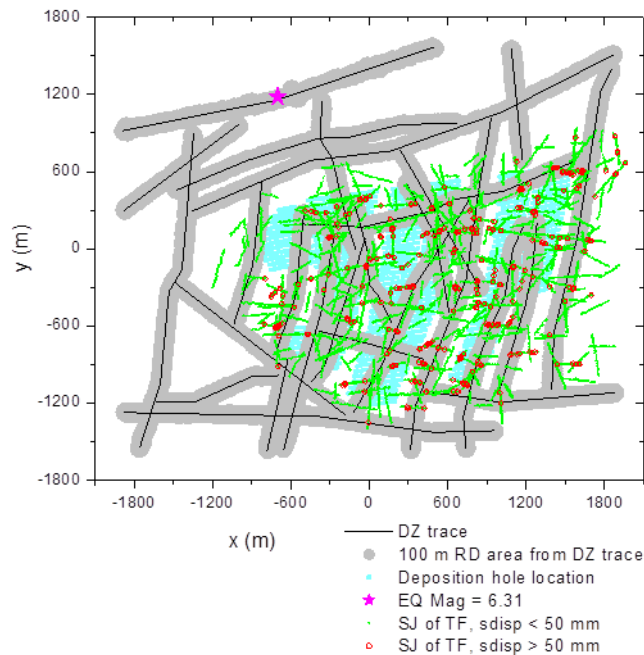


**Figure 98.** Respect distances of 100 m (grey areas) applied to the traces of the deformation zones (black lines) and shear displacements of smooth joints constituting target fractures: shear displacements smaller than 50 mm are shown in green; shear displacements larger than the canister damage threshold of 50 mm are shown in red. The figure corresponds to the modelling case where the ZFMWNN0001 is activated with powering shear force under present-day “most likely” stress field with realization DFN03h.

were avoided. In Figure 98, target fractures undergoing shear displacement smaller than 50 mm are shown in green, while larger shear displacements than 50 mm are shown in red. When applying a respect distance area of 100 m (grey areas) from the traces of deformation zones (black lines), target fracture with shear displacement exceeding 50 mm are often avoided. However, there still are some target fractures located beyond the respect distance, and therefore within the rock volume where canisters will be emplaced in the repository, exceeding the damage threshold. Furthermore, the spatial economy of the repository would be heavily affected by the application of the respect distance to all deformation zones shorter than 3 km.

- 7) From the modelling of an earthquake striking during the sequential heating of the repository under the present-day “most likely” stress field, it is found that the shear displacement of target fractures and deformation zones is magnified compared to the case when the earthquake strikes without heating (e.g. after cooling of the repository). Displacements increase up to a factor of 3 due to the overlapping effect of the earthquake and the heating. The magnitudes of the triggered earthquake and of the co-seismic events are also increased by the heating. Compared to the case with an earthquake without heating, several target fractures (in particular those with trace

length smaller than 200 m) show shear displacements larger than the canister damage threshold of 50 mm, and cannot be regarded as outliers.

- 8) The linear relation between target fracture length and shear displacement as postulated by Fälth et al. (2010) is not found in the modelling results with PFC. This is due to the fact that in the PFC models the target fractures are randomly distributed, have a wide range of lengths and are interconnected with each other. These features were not considered in the models by SKB. In some cases, the box-and-whisker diagrams show a weak increasing trend of the median values of fracture shear displacements induced by the earthquakes with increasing fracture trace length. This is not observed in the modelling results of fracture responses induced by heating.

It can also be observed that large shear displacements are not always located in the central part of the target fractures, but can also be located closer to the tips of the fractures. This observation is in contradiction with SKB's assumption that target fractures exhibit the largest shear displacement in their central part and the lowest shear displacement at their tips.

- 9) From the modelling campaigns (38 modelling cases in total), it is observed that the risk of canister damage tends to be the highest under the conditions where an earthquake occurs when the repository rock mass is heated due to the decay of the spent nuclear fuel in the canisters. The heating effect for sequential heating tops after about 50 years, which corresponds to the time of operation of the repository or just after its closure. However, the effects of heat generation fade out after about 1000 years after closure of the repository.

Another case where the risk of canister damage is most evident is when an earthquake occurs on gently dipping zones either under present-day stress conditions, or under maximum ice cover during a glacial cycle.

It should be noted that the probability of occurrence of an earthquake is directly related to the span of the time interval considered for the risk calculation, thus the time of the peak effect due to heating at 50 years after the start of the canister deposition is relatively very short compared to the time spans related to different phases of one or several glacial cycles.

- 10) This study focused on the shear displacement of the target fractures. Due to a technical limitation of the modelling method, monitoring of the shear velocity at target fractures could not be done. In order to get the shear velocity of a target fracture, it is necessary to store all the values of shear displacement at each time and for each single smooth joint that belongs to each single target fracture. The shearing velocity can then be obtained as the differential of the shear displacement versus time curve. There are 346 and 271 target fractures in realization DFN03h and DFN06h, respectively, and the total number of smooth joints constituting the target fractures amount to 12,733 and 10,580, respectively. PFC does not allow recording histories of more than 10,000 smooth joints to monitor the shear displacement and velocity.
- 11) Seismometer particles were placed in the PFC models along the deformation zone ZFMWNW0809A, ZFMWMW0001, ZFMWNW2225, ZFMNW1200 (Figure 34), and the seismic slip velocity can be recorded during the calculations. Figure 35 shows an example of average peak slip velocity records after the seismic activation of a deformation zone. This

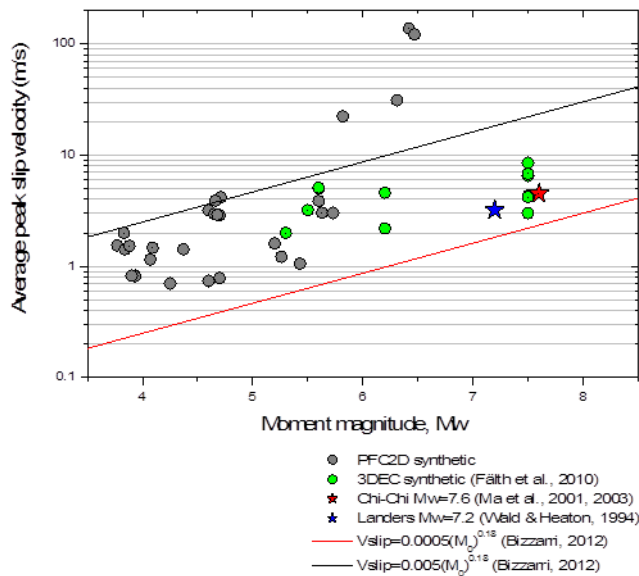
example shows that on average the average peak slip velocity on most of the modelled deformation zone hosting an earthquake is around 1 m/s.

Figure 99 shows the relation between the simulated earthquake moment magnitude and the average peak slip velocity of the active deformation zones in the PFC models (grey dots). The 3DEC synthetic earthquakes from Fälth et al. (2010) are also shown (green dots) together with data from the Chi-Chi earthquake ( $M=7.6$ ; Ma et al., 2001 and 2003) and from the Landers earthquake ( $M=7.2$ ; Wald & Heaton, 1994) (marked by red and blue stars, respectively). Moment magnitude  $M_w$  versus slip velocity  $V_{slip}$  relations were obtained by Bizzarri (2012) based on investigations of a wide catalogue of synthetic earthquakes, numerically modelled as spontaneous, fully dynamic, 3-D ruptures on extended faults and governed by different frictional laws. Bizzarri (2012) proposed the equation:

$$V_{slip} = aM_w^{0.18} \quad \text{Eq. (8-3)}$$

For this equation, two proportionality constants  $a$  are used here: 0.0005 m/s and 0.005 m/s. The figure illustrates that the average peak slip velocity of an active deformation zone hosting an earthquake increases with the magnitude. Comparison between the 3DEC synthetic data and the PFC synthetic data shows similar trends. However, there are some data points showing significantly large slip velocities. These data points correspond to the modelling cases with PFC where the shear force on the zone ZFMWNW0001 (truncated Singö fault) was powered up to increase the magnitude.

It could be assumed that the slip velocity on target fractures is lower than the slip velocity on an earthquake hosting deformation zones, but this assumption was not checked within the scope of this study.



**Figure 99.** Average peak slip velocity versus moment magnitude of synthetic earthquakes. PFC synthetic data (grey dots) and 3DEC data (green dots; Fälth et al., 2010) are compared with two regression lines by Bizzarri (2012). The Chi-Chi and Landers earthquakes are provided for comparison (blue and red star).



## 9. The Consultants' overall assessment and conclusions

The Authors have conducted three campaigns of numerical modelling related to the influence of heating and earthquakes on the repository of spent fuel at Forsmark. Horizontal and vertical sections of the repository were studied.

The first modelling campaign deals with shear displacement of the target fractures and seismic events induced by the heat from the canisters containing the spent nuclear fuel. The second modelling campaign deals with shear displacement of the target fractures and co-seismic events induced by the occurrence of an earthquake at nearby deformation zones that are considered unstable under present-day "most likely" stress field and stress fields induced during a future glacial period. The third modelling campaign envisages modelling of superposition of heat generation and earthquake on selected deformation zones during operation or after closure of the repository under present-day stress field.

An earthquake is modelled in a generic way, where the strain energy stored at a specific deformation zone due to the applied stress field is released.

From the results of the three modelling campaigns summarized and discussed in Chapter 8, general conclusions can be drawn as listed below:

- Heat from the disposed spent nuclear fuel can induce seismicity in the deposition panels and surrounding rock mass.
- Heat from the disposed spent nuclear fuel can induce shear displacement of the deformation zones (striking NE-SW) that are judged to be stable by SKB. Shearing can lead to interaction with other deformation zones (striking NW-SE) that are judged by SKB to be unstable under present-day stress field. Such interaction can lead to moderately large magnitude seismic events. These events tend to occur at the intersections of the deformation zones.
- An earthquake occurring at a deformation zone in unstable state can induce shear displacement of the target fractures exceeding the canister damage threshold. However, by adopting 10% of significance level for the shear displacement on target fractures (95th percentile), there is little risk that target fractures will undergo shearing beyond the canister damage threshold of 50 mm.
- An earthquake occurring at a deformation zone can trigger another moderate event at large distance from the main earthquake hypocentre. This could not be modelled by SKB as multiple deformation zones and seismic wave attenuation were not taken into account in their models.
- Secondary shear displacements of the target fractures and deformation zones induced by the earthquakes are in general estimated to have lower values than those obtained from the regressions for primary events. However, there is always a small probability that target fractures can undergo a shear displacement larger than the canister damage threshold of 50 mm. This probability is higher for the earthquake cases than for the case with only heating.
- Occurrence of an earthquake at a nearby deformation zone while the repository is under heating can induce shear displacements of target

fractures exceeding the canister damage threshold of 50 mm. In this case 1% to 3% of the target fractures exceed the canister damage threshold of 50 mm.

- An earthquake tends to increase the amount of shear displacement of the target fractures in a heated repository by up to three times compared to the case with only heating. The maximum shear displacement in the models with earthquake during heating is up to 280 mm.
- Among all investigated modelling cases, the risk to impair the integrity of the repository tends to be the highest when an earthquake occurs at deformation zone ZFMWNW2225, under present-day stress field and during the heating of rock mass. Similar cases for the vertical section model were not considered in this study.
- From the statements listed above, the Authors draw an overall conclusion that the scope of the modelling and analyses conducted by SKB are not broad enough to conclude that the integrity of the repository can be guaranteed, in particular in case of an earthquake activation at a major deformation zone occurring at present day and in a future glacial period, and in particular in the case of an earthquake striking during the operational and thermal phases of the repository.
- Therefore, the Authors conclude and suggest that additional modelling studies should be carried out taking into account a realistic geometry of the Forsmark site, including deformation zones and target fracture networks (DFN). In particular, modelling cases should be tested where the repository is subjected to an earthquake loading during the operational and thermal phases of the repository.

## 10. Recommendations

In this Chapter, several issues that the Authors suggest for further study are addressed:

### *Discrete Fracture Network (DFN)*

Among the ten DFN realizations produced for this assignment to SSM, two cases were adopted, which are chosen as the most conservative and the least conservative cases. In order to draw a more general conclusion, the Authors suggest that several more simulations shall be conducted with different DFN realizations, at least one additional DFN with neutral level of conservativeness.

### *Target fractures of length shorter than 125 m*

The DFNs adopted have length distributed in the range between 125 and 600 m. As some of the earthquake modelling cases show that the shortest fractures have quite large shear displacements, it is expected that target fractures that are even shorter than 100 m could undergo large shear displacements exceeding the canister damage threshold in particular circumstances. Therefore, the Authors suggest that the fracture length range in the DFNs be widened so to contain smaller fractures, e.g. with trace length between 50 m and 125 m.

### *Sequential heating*

Sequential heating of the rock mass can be modelled in a more realistic way by adopting “2-days-1-canister rule”. In the sequential heating modelling conducted in this study, it is assumed that all canisters in one panel are disposed at the same time, which is more realistic than the modelling cases where all canisters are disposed at the same time. However, the Authors argue that panel heating is still unrealistic and suggest conducting more detailed sequential calculations of the heating scenario.

### *Representation of deformation zones*

The Authors argue that representing a deformation zone or fault with one discrete planar feature is unrealistic. In this study, deformation zones are represented as a collection of small fractures aligned in a stepped way. This way of representing deformation zones enables mimicking undulated structures which the Authors consider as more realistic than the approach by SKB. However, in such way, it is not possible to mimic the observed structure of the deformation zones where the total thickness of deformation zone, consisting of a fractured core and a damage zone, is considered. In the early stage of the model development in this study, deformation zones were represented as combination of fractured core and damage zone. Smooth joints were used for the core and the damage zone by means of an assembly of smaller bonded particles together with lower stiffness and strength. However, as the model was modified later to include more deformation zones, this approach was not applied as much more particles were needed to construct the model. Nevertheless, the Authors suggest that this way of representing deformation zones should be investigated.

### *Generic earthquake modelling*

Release of the stored strain energy is simulated by lowering the bond strength of the smooth joint contacts. The Authors suggest that, in addition to lowering of the strength parameters, also lowering of the joint normal and shear stiffness should be tested to see how it affects the magnitudes of the activated earthquake. Also, lowering of the strength parameters was done in one step in this study. It is necessary to check how much the number of steps in which the strength lowering is done (e.g. in two or three steps, or even in several steps to obtain a “smooth earthquake”) affects the results.

### *Earthquake activation time for the thermal-and-earthquake modelling cases*

In the heat and earthquake modelling cases, earthquake activation is simulated after 50 years of sequential heating of the repository. It is necessary to conduct several more modelling cases, where an earthquake occurs at different selected times, e.g. 25 years after the start of the heating of each panel A, B, C, and D, respectively.

### *Earthquake activation at multiple deformation zones*

In the earthquake modelling cases, it is assumed that earthquake activation takes place at a single deformation zone, e.g. either zone ZFMWNW0809A, ZFMWNW2225 or ZFMNW1200. However, there can be a situation where multiple deformation zones that are oriented parallel, close in space and/or connected are activated at the same time, e.g. for the case of zone ZFMWNW0123 + ZFMNW1200 + ZFMNNW0100, or zone ZFMWNW1053 + ZFMWNW0809A. Activation of multiple deformation zones is done in the vertical section models in this study, where the parallel and connected deformation zones are activated at the same time, which led to higher resulting magnitudes of the calculated earthquake.

# 11. References

- Backers T, Meier T, Gipper P, Stephansson O, 2014. Rick Mechanics – Assessing probability and extent of blind faults and fault-end growth around the KBS-3 repository at Forsmark, SSM Technical Note 2014:58, Swedish Radiation Safety Authority (SSM).
- Bizzarri A, 2012. Rupture speed and slip velocity: What can we learn from simulated earthquakes? *Earth and Planetary Science Letters* 317-318, p. 196-203.
- Derschowitz WS, Einstein HH, 1988. Characterizing rock joint geometry with joint system models. *Rock Mechanics & Rock Engineering* 21, p. 21-51.
- Deisman N, Mas Ivars D, Pierce M, 2008. PFC2D smooth joint contact model numerical experiments. In: *Proceedings of the GeoEdmonton'08*, Edmonton, Canada, Paper 83.
- Dumstorff P, Yoon J, Zang A, Dresen G, Meschke G, 2006. Numerical simulation of crack paths in laboratory compressed Aue granite. *Geophysical Research Abstracts*, Vol. 8, No. 07361.
- Esmaili K, Hadjigeorgiou J, Grenon M, 2009. Estimation of synthetic rock mass strength accounting for sample size. In: *Proceedings of the international conference on rock joints & jointed rock mass*, Kulatilake PHSW ed. Arizona: Tucson, 7-8 Januari 2009.
- Fälth B, Hökmark H, Munier R, 2010. Effects of large earthquakes on a KBS-3 repository. Evaluation of modelling results and their implications for layout and design. SKB TR-08-11, Swedish Nuclear Fuel and Waste Management Company (SKB).
- Fälth B, Hökmark H, 2013. PM Termiskt inducerade skalv. SKB DokumentID 1403906 (in Swedish), Swedish Nuclear Fuel and Waste Management Company (SKB).
- Glamheden R, Fredriksson A, Röshoff K, Karlsson J, Hakami H, Christiansson R, 2007. Rock Mechanics Forsmark. Site descriptive modelling Forsmark stage 2.2, SKB R-07-31, Swedish Nuclear Fuel and Waste Management Company (SKB).
- Hadjigeorgiou J, Esmaili K, Grenon M, 2009. Stability analysis of vertical excavations in hard rock by integrating a fracture system into a PFC model. *Tunnelling and Underground Space Technology* 24, p. 296-308.
- Hanks TC, Kanamori H, 1979. A moment magnitude scale. *Journal of Geophysical Research* 84 (B5), p. 2348-2350.
- Hazard JF, Young RP, 2002. Moment tensors and micromechanical models. *Tectonophysics* 356, p. 181-197.
- Hazard JF, Young RP, 2004. Dynamic modelling of induced seismicity. *International Journal of Rock Mechanics & Mining Sciences* 41, p. 1365-1376.
- Hökmark H, Lönnqvist M, Kristensson O, Sundberg J, Hellström G, 2009. Strategy for thermal dimensioning of the final repository for spent nuclear fuel. SKB R-09-04, Swedish Nuclear Fuel and Waste Management Company (SKB).
- Hökmark H, Lönnqvist M, Fälth B, 2010. THM-issues in repository rock. Thermal, mechanical, thermo-mechanical and hydromechanical evolution of the rock at

- the Forsmark and Laxemar sites. SKB TR-10-23, Swedish Nuclear Fuel and Waste Management Company (SKB).
- Itasca, 2009. PFC2D version 4.0. Theory and Background. Itasca Consulting Group Inc. Minneapolis, USA.
- Kulatilake PHSW, Malama B, Wang J, 2001. Physical and particle flow modelling of jointed rock block behavior under uniaxial loading. *International Journal of Rock Mechanics & Mining Sciences* 38, p. 641-657.
- Leonard M, 2010. Earthquake Fault Scaling: Self-Consistent Relating of Rupture Length, Width, Average Displacement, and Moment Release. *Bulletin of Seismological Society of America* 100, p. 1971-1988.
- Lund B, Schmidt P, Hieronymus C, 2009. Stress evolution and fault stability during the Weichselian glacial cycle. SKB TR-09-15, Swedish Nuclear Power and Waste Management Company (SKB).
- Ma K-F, Mori J, Lee S-J, Yu SB, 2001. Spatial and Temporal Distribution of Slip for the 1999 Chi-Chi, Taiwan, Earthquake. *Bulletin of the Seismological Society of America* 91 (5), p. 1069-1087.
- Ma K-F, Brodsky EE, Mori J, Ji C, Song T-RA, Kanamori H, 2003. Evidence for fault lubrication during the 1999 Chi-Chi, Taiwan, earthquake (Mw7.6). *Geophysical Research Letters* 30 (5), p. 1244.
- Martin CD, 2007. Quantifying in situ stress magnitudes and orientations for Forsmark. Forsmark stage 2.2. SKB R-07-26, Swedish Nuclear Fuel and Waste Management Company (SKB).
- Mas Ivars D, Pierce M, DeGagné D, Darcel C, 2008. Anisotropy and scale dependency in jointed rock-mass strength – A synthetic rock mass study. In: *Proceedings of the 1<sup>st</sup> international FLAC/DEM symposium on numerical modeling*, Hart R, Detournay C, Cundall P, eds. Paper 06-01. Minneapolis: Itasca Consulting Group, 25-27 August 2008.
- Mas Ivars D, Pierce ME, Darcel C, Reyes-Montes J, Potyondy DO, Young RP, Cundall PA, 2011. The synthetic rock mass approach for jointed rock mass modelling. *International Journal of Rock Mechanics & Mining Sciences* 48, p. 219-244.
- Min KB, Lee J, Stephansson O, 2014. Rock Mechanics – Evolution of fracture transmissivity within different scenarios in SR-Site, SSM Technical Note (in preparation), Swedish Radiation Safety Authority (SSM).
- Morris JP, Jocker J, Prioul R, 2013. Exploring alternative characterizations of fracture stiffness and their respective scaling behaviors. . In: *Proceedings of the 47th US Rock Mechanics / Geomechanics Symposium*, San Francisco, CA, USA, 23-26 June 2013. Paper ARM 13-197.
- Munier R, 2010. Full perimeter intersection criterion. Definitions and implementations in SR-Site. SKB TR-0-21, Swedish Nuclear Fuel and Waste Management Company (SKB).
- Park ES, Martin CD, Christiansson R, 2004. Simulation of the mechanical behavior of discontinuous rock masses using a bonded-particle model. In: *Proceedings of the 6th North American Rock Mechanics Symposium*, Houston, Yale D et al. eds. Paper ARMA 04-480.

- Pierce M, Gaida M, DeGagne D, 2009. Estimation of rock block strength. In: Proceedings of the 3<sup>rd</sup> Canada-US Rock Mechanical Symposium, Toronto, May 2009.
- Potyondy DO, Cundall PA, 2004. A bonded-particle model for rock. *International Journal of Rock Mechanics & Mining Sciences* 41, p. 1329-1364.
- SKB, 2009. Site engineering report Forsmark. Guidelines for underground design Step D2. SKB R-08-83, Swedish Nuclear Fuel and Waste Management Company (SKB).
- SKB, 2011. Long-term safety for the final repository for spent nuclear fuel at Forsmark Main report of the SR-Site project. SKB TR-11-01, Swedish Nuclear Fuel and Waste Management Company (SKB).
- Stephens MB, Fox A, La Pointe P, Simeonov A, Isaksson H, Hermanson J, Öhman J, 2007. Geology Forsmark. Site descriptive modelling Forsmark stage 2.2. SKB R-07-45, Swedish Nuclear Fuel and Waste Management Company (SKB).
- Zang A, Stanchits S, Dresen G. 2002. Acoustic emission controlled triaxial rock fracture and friction tests. In: Dyskin AV, Hu X, Sahouryeh E, eds., *Structural Integrity and Fractures*, Swets & Zeitlinger, Lisse, p. 289-294.
- Zang A, Yoon JS, Stephansson O, Heidbach O, 2013. Fatigue hydraulic fracturing by cyclic reservoir treatment enhances permeability and reduces induced seismicity. *Geophysical Journal International* 195, p. 1282-1287.
- Wald DJ, Heaton TH, 1994. Spatial and temporal distribution of slip for the 1992 Landers earthquake, California. *Bulletin of the Seismological Society of America* 84 (3), p. 668-691.
- Wanne TS, Young RP, 2008. Bonded-particle modelling of thermally fractured granite. *International Journal of Rock Mechanics & Mining Sciences* 45, p. 789-799.
- Wells DL, Coppersmith KJ, 1994. New Empirical Relationships among Magnitude, Rupture Length, Rupture Width, Rupture Area, and Surface Displacement. *Bulletin of Seismological Society of America* 84, p. 974-1002.
- Yoon JS, 2007. Application of experimental design and optimization to PFC model calibration in uniaxial compression simulation. *International Journal of Rock Mechanics & Mining Sciences* 44, p. 871-889.
- Yoon JS, Zang A, Stephansson O, 2012. Simulating fracture and friction of Aue granite under confined asymmetric compressive test using clumped particle model. *International Journal of Rock Mechanics & Mining Sciences* 49, 68-83.
- Yoon JS, Zang A, Stephansson O, 2014. Numerical investigation on optimized stimulation of intact and naturally fractured deep geothermal reservoirs using hydro-mechanical coupled discrete particles joint model. *Geothermics* 52, p. 165-184.



# Coverage of SKB reports

**Table A1-1.** Coverage of SKB reports reviewed by the authors.

Reviewed report	Reviewed sections
SKB TR-10-23	Chapter 4. Data used in THM modelling ; Chapter 5. Thermal evolution
SKB TR-08-11	Entire report
SKB DocumentID 1403906	Entire report; Figure 5, p. 10, CFS values of several deformation zones under present day stress condition are taken and used for comparison.
SKB R-07-31	Entire report; Chapter 3. Mechanical properties of intact rock; Chapter 4. Mechanical properties of fractures; Chapter 5. Rock mass mechanical properties; Chapter 6. In situ state of stress; Chapter 7. Summary of the rock mechanics model
SKB R-07-45	Appendix 15
SKB R-09-04	Chapter 2. Head load
SKB TR-09-15	Chapter 7. Glacially induced stress
SKB R-05-27	Section 5.3, Rock attenuation factor (near-field), $\lambda_1 = 0.044 \text{ m}^{-1}$ is checked to see if the seismic quality factor Q used in the modelling is reasonable, Q = 50.



# Quality checks on DFN deliveries for PFC simulations with horizontal and vertical section models

## Horizontal sections

*Joel Geier, Clearwater Hardrock Consulting, Date of data delivery: 19 Mar 2014, Document date: 26 Mar 2014.*

This memorandum concerns the delivery of the following data files that were produced on 11 Mar 2014:

SRGeoPFC\_r2\_##\_HZ2dr.prn

where ## = 01, 02, ..., 10.

These files were produced based on DFN simulations for the calculation of  $N_{crit}$  (the number of critical positions). Full documentation is given in an SSM Technical Note by Geier (2014a, in prep.)

The simulated DFN models are based on the same parameters as defined for the  $rI$  calculation that was delivered earlier, and use the same parameter files for input to the *fracgen* simulation module. The only difference is that the new simulations were produced using v. 2.4.1.1 of the *fracgen* module, which was updated to correct an error due to a coding bug, in the simulation of fracture orientations (described in a separate SSM Technical Note by Geier, 2014b, in prep.).

The main parameters for generating fracture sets for these realizations are summarized in Table A2.1.

**Table A2.1.** Parameters for generation of fracture sets for the  $r_0$ -fixed alternative, Calculation Case r2.

	Mean pole trend (°)	Mean pole plunge (°)	Fisher concentration $\kappa$	$r_0$ (m)	$k_r$	$P_{32}$ (unscaled)	$r_{max}$
<b>FFM01</b>							
NE global	314.9	1.3	20.94	0.039	2.72	1.733	564.2
NS global	270.1	5.3	21.34	0.039	2.75	1.292	564.2
NW global	230.1	4.6	15.70	0.039	2.61	0.948	564.2
SH global	0.8	87.3	17.42	0.039	2.58	0.624	564.2
ENE local	157.5	3.1	34.11	0.039	2.97	0.256	564.2
EW local	0.4	11.9	13.89	0.039	2.93	0.169	564.2
NNE local	293.8	0.0	21.79	0.039	3.00	0.658	564.2
SH2 local	164.0	52.6	35.43	0.039	2.61	0.081	564.2
SH3 local	337.9	52.9	17.08	0.039	2.61	0.067	564.2
<b>FFM06</b>							
NE global	125.7	10.1	45.05	0.039	2.79	3.299	564.2
NS global	91.0	4.1	19.49	0.039	2.78	2.150	564.2
NW global	34.1	0.8	16.13	0.039	2.66	1.608	564.2
SH global	84.3	71.3	10.78	0.039	2.58	0.640	564.2
ENE local	155.4	8.3	20.83	0.039	2.87	0.194	564.2
SH2 local	0.0	47.5	12.71	0.039	2.61	0.429	564.2

The steps in the extraction of data from the fracture realizations are:

1. Extraction of all hexagonal fractures (panels) with equivalent radius  $> 50$  m
2. Conversion of the resulting (thinned) set of hexagonal fractures to disks (not used directly for the production of these datasets, but used to simplify checks of the statistical properties of the fracture population);
3. Identification of fractures that cross a horizontal plane at  $z = -465$  m and extraction fracture traces on that plane, using the DFM module *dfmslice* v. 2.4.1.1.
4. Further processing of the 2-D cross-section data to the format requested by GFZ.

These steps are carried out by the following Linux C-shell script which was used to extract these data from DFN simulated fracture data files with the corresponding names of the form:

SRGeoPFC\_r2\_##\_fracs.pan

that were produced for the *Ncrit* task.

**PFC\_get\_thin\_sections\_all2**

```
#!/bin/csh -f
#
# Script used to thin fractures and post-process fracture panels files into 3-D disk format.
#
set SRC = "../FMcritical2"
set STEM = "SRGeoPFC"
foreach CASE ( r2 o2 t2 rg2 og2 tg2 )
  foreach N ( 01 02 03 04 05 06 07 08 09 10 )
    set NAME = "${STEM}_${CASE}_${N}"
    if( -f $SRC/${NAME}_fracs.pan ) then
      awk -f thin_hexpanels.awk -v RMIN=50 $SRC/${NAME}_fracs.pan > $
{NAME}_thin_fracs.pan
      awk -f hexpanel_disks.awk -v OPT=DIP ${NAME}_thin_fracs.pan > $
{NAME}_thin_disks.prn
      dfmslice2411 -p ${NAME}_thin_fracs.pan -x XsectionHZ_465m.pan > $
{NAME}_thin_HZ_465m.prn
      awk -f process2dsection.awk ${NAME}_thin_HZ_465m.prn ${NAME}_thin_disks.prn > $
{NAME}_H22dr.prn
    endif
  end
end
```

The source files for these calculations are contained in the directory:

~/Desktop/modelling/FMcritical2.

Note that this script produces data files for five other calculation cases in addition to the  $r2$  calculation case ( $o2$ ,  $t2$ ,  $rg2$ ,  $og2$ , and  $tg2$ ). These other cases are not covered by this quality check, as it is not anticipated that the results will be used for PFC calculations. A thorough check of those calculation cases for the purposes of the *Ncrit* task is ongoing, and will be reported as part of the technical note for that task.

### Quality Check 1: Comparison of expected and simulated P32 fracture intensity as a function of fracture radius

This quality check was carried out based on the full DFN realizations for the *Ncrit* calculations, prior to thinning. The comparison is based on the increments of  $P32$ , the fracture intensity per unit volume, for a given range of fracture radii  $[r1, r2]$ . For brevity these increments are referred to as  $P32[r1, r2]$ . It may be noted that the overall fracture intensity  $P32[0, \infty]$  is obtained as a particular case.

As discussed in further detail by Geier (2014a), the realizations for *Ncrit* calculations use selective thinning of fractures as a function of fracture radius and distance from the repository horizon. Therefore the check of  $P32[r1, r2]$  needs to be based on the portion of the model volume within which all (or nearly all) fractures are retained. This has been done in the case of the *Ncrit* calculations (which are used to provide datasets for PFC calculations) by calculating  $P32[r1, r2]$  just for the volume in the depth range  $-475 \text{ m} < z < -460 \text{ m}$ , within the area of a minimal polygon that contains the deposition panels in plan view (i.e. the polygon defined in the *fracgen* input file *SDMForsmark468m.sites*). For large fractures that extend above and/or below this depth zone, only the portion of the fracture area that lies in the depth range  $-475 \text{ m} < z < -460 \text{ m}$  is counted in the calculation of  $P32[r1, r2]$ .

The results for fracture domains FFM01 and FFM06, respectively, are plotted in Figures A2.1 and A2.2. In each figure, the top graph shows the expected distribution while the lower two graphs give the simulated results for realizations 01 and 02, respectively. The bars represent  $P32[r1, r2]$  for increments of a quarter order of magnitude in fracture (equivalent) radius.

Note that fractures of  $r < 1.5 \text{ m}$  have been omitted from the stochastic realizations, and the representation of fractures with radius  $< 10 \text{ m}$  is likely to be affected by the discarding (for the *Ncrit* calculations) of fractures in the size range from about  $1.5 \text{ m}$  to  $10 \text{ m}$  that cannot possibly intersect the deposition tunnels. Therefore comparison should be based on the increments from  $10 \text{ m}$  and upward. It can be seen that, for  $r \geq 10 \text{ m}$ , there is visually very good agreement both in terms of total fracture intensity and the fracture intensity for individual fracture sets. Very little difference is seen between the two stochastic realizations.

The exception in terms of agreement with the theoretical distribution is in for the increment of fracture size ( $r = 316 \text{ m}$  to  $562 \text{ m}$ ) for which  $r$  approaches the maximum defined value,  $r_{max} = 564.2 \text{ m}$ . This was initially thought to be a stochastic effect due to the large impact of individual fractures on this scale, for  $P32$  in this increment.

However, further investigation shows that this is a result of the discrete nature of the pseudorandom number generator that is used for Monte Carlo simulation of the fracture size distribution, in combination with the minimum radius for this calculation case ( $r_{min} = 1.5 \text{ m}$ ). The pseudo-random number generator (based on an algorithm given by Press et al., 1986) produces 714025 discrete values on the

interval [0,1). In combination with the algorithm used for generating values of  $r$  from a power-law distribution, this leads to an effective maximum radius:

$$r_{max,eff} = r_{min} \cdot \exp\left[\frac{-\log\left(1 - \frac{1}{714025}\right)}{k_r}\right]$$

which varies from about 202 m to 279 m depending on the value of  $kr$  for a particular fracture set. By comparison, the simulations used in other calculation cases for the  $N_{crit}$  calculations ( $rg2$ ,  $o2$ ,  $og2$ ,  $t2$ , and  $tg2$ ) used  $r_{min} = 3$  m, which gives an effective  $r_{max,eff} = 405$  m to 558 m depending on the value of  $kr$  for a particular fracture set.

The theoretical frequency of fractures larger than  $r_{max,eff}$  is less than 1 per 714025. In comparison, the realizations of  $r2$  the calculation case typically have about 920,000 fractures, prior to thinning out of smaller fractures for the PFC datasets. Thus a given realization would theoretically be expected to contain one or occasionally two fractures in the size range larger than  $r_{max,eff}$ , most likely from one of the four “global” sets due to their greater share of the overall P32, and the persistence of their tails for higher radius.

Due to the method of simulation (in which, for each fracture set in each fracture domain, fractures are generated until the target value of P32 is attained), it is expected that this artificial truncation of the  $r$  distribution is compensated for by generating more fractures in the smaller size classes. For the ongoing  $N_{crit}$  calculations, the significance will be checked by increasing  $r_{min}$  for the  $r2$  calculation case, to use the same value ( $r_{min} = 3$  m) as has been used for the other calculation cases ( $rg2$ ,  $o2$ ,  $og2$ ,  $t2$ , and  $tg2$ ). The results from that exercise should be helpful for evaluating the effects of omitting a few of these very sparse but large fractures from the present datasets.

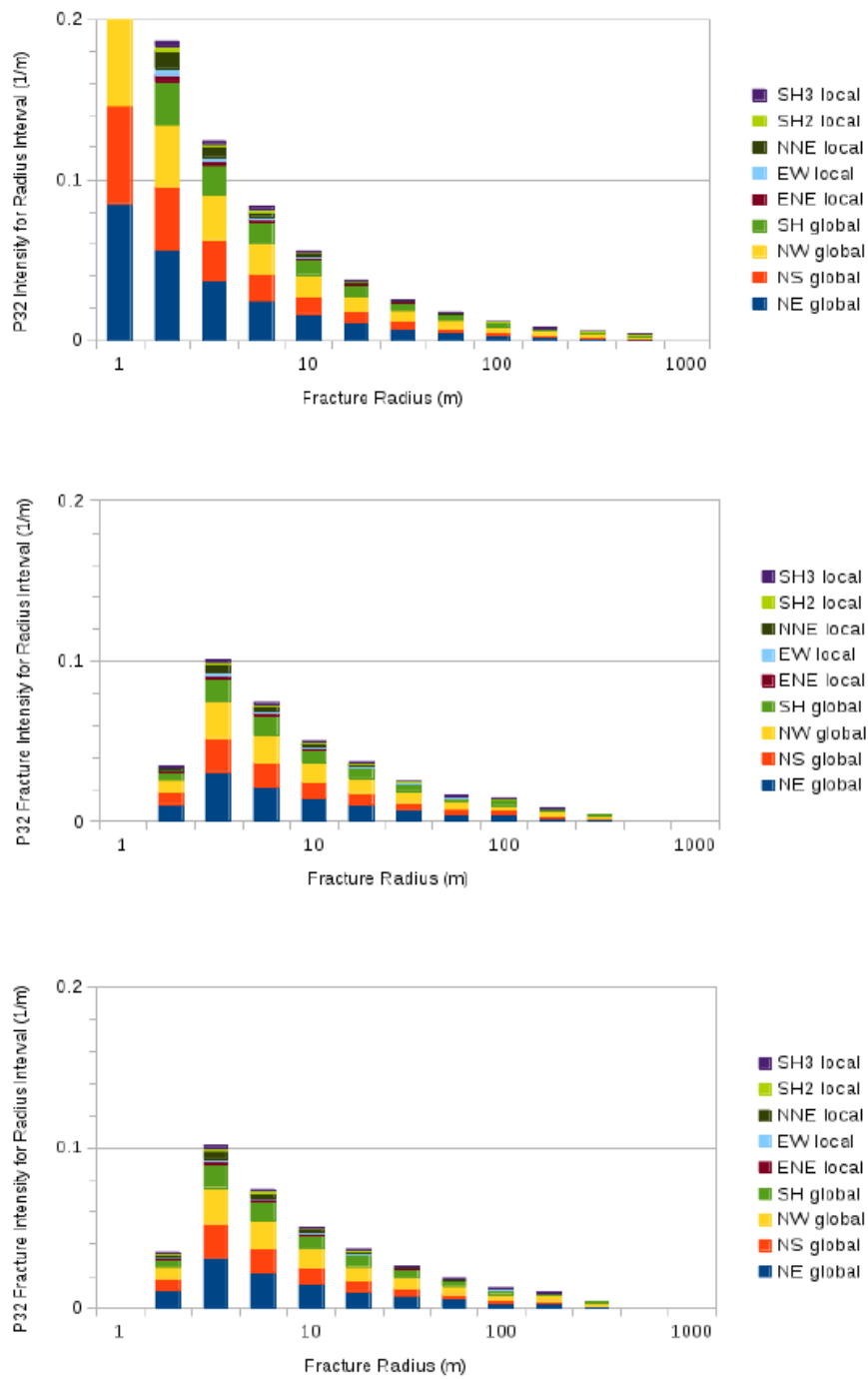


**Figure A2.1.** Comparison of theoretical (top plot) and simulated (bottom two plots) increments of  $P_{32}$  fracture intensity for each of the fracture sets in fracture domain FFM01. The two lower plots represent two different realizations (01 and 02).

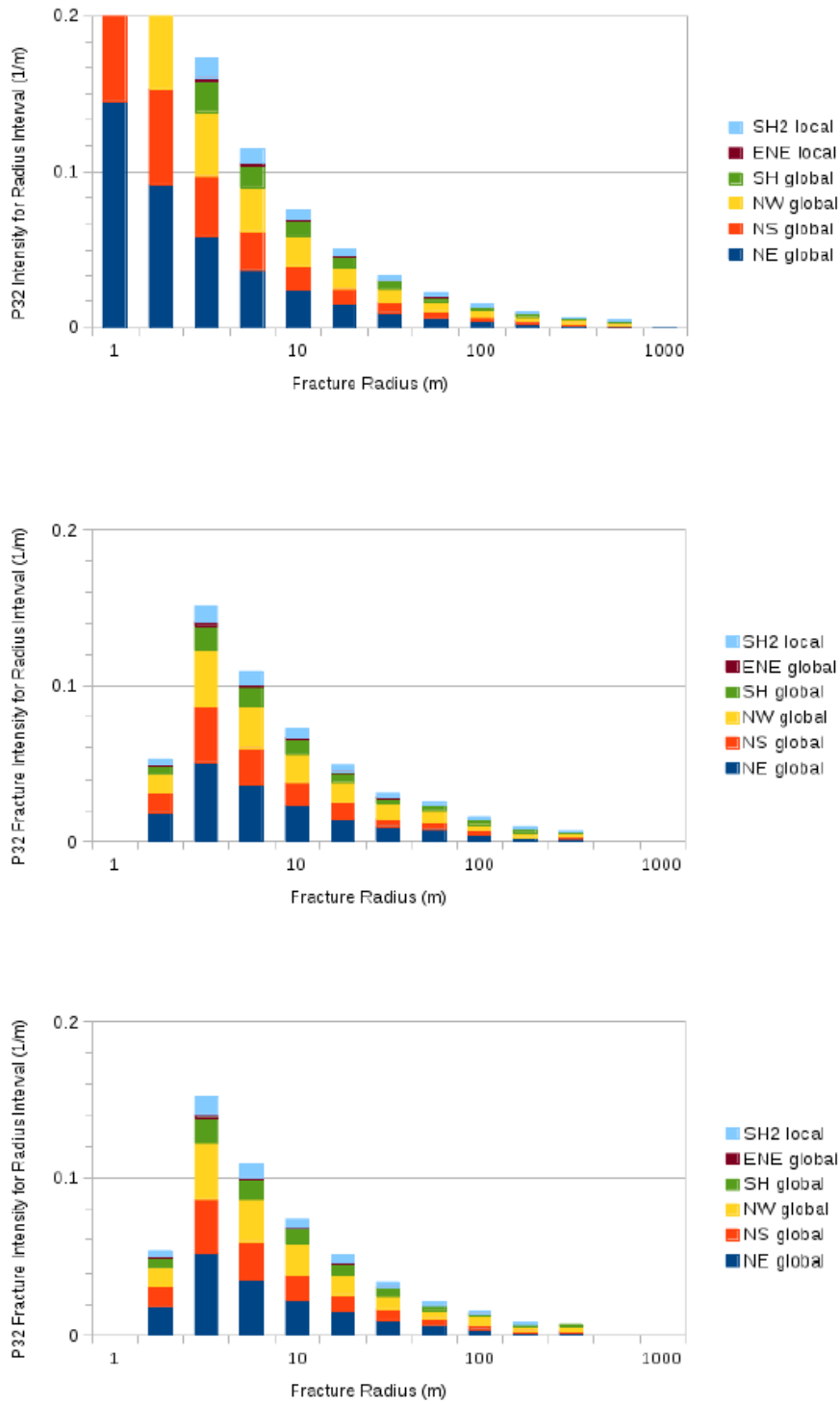


**Figure A2.2.** Comparison of theoretical (top plot) and simulated (bottom two plots) increments of  $P_{32}$  fracture intensity for each of the fracture sets in fracture domain FFM06. The two lower plots represent two different realizations (01 and 02).

## Quality Check 2: Fracture orientation distributions

The simulated fracture orientation distributions have been confirmed both quantitatively by statistical measures, and qualitatively by equal-area stereonet plots for individual fracture sets.

The consistency of the fitted Fisher mean poles (mean pole trend and plunge in degrees, as given in parentheses) and concentration parameters  $\kappa$  in the following listing have been checked against the same parameters for the same 15 sets as listed in Table A2.1.

The mean pole directions, as listed below, are generally in very close agreement, usually within a fraction of a degree. It should be noted that for Set 5 (SH global) fitted values for trend and plunge such as (359.94, 87.29) are in close agreement with the specified values (0.8, 87.3) when it is recalled that the azimuth of strike is a cyclic value. Similarly for Set 7, fitted directions such as (113.73, 0.09) are in close agreement with the specified value of (293.8, 0.0) when it is considered that fracture poles are bidirectional so can be represented equivalently by a direction that is 180 degrees opposed.

Values of the Fisher concentration  $\kappa$ , as also listed below, generally agree with the specified values within 5%.

Supplementary to these quantitative checks, stereonet plots were also produced for graphical inspection, mainly to confirm that the distributions reproduced have appropriate radial symmetry (as the mean orientations and concentration about the mean are checked by quantitative measures). These are shown for Realization 01 of Calculation Case  $r_2$  in Figures A2.3 through A2.5.

The very close agreement of the quantitative statistical estimates of mean directions and Fisher concentrations with the specified values, along with the visual checks of radial symmetry based on the plots in Figures A2.3 through A2.5, give high confidence that the orientation distributions for each fracture set are accurately simulated.

Comparison with equivalent plots by SKB would be of interest. However, SKB has not presented stereoplots to show the expected distribution of fracture poles for the derived statistical models of each of these sets. Plots of the raw data that were used to estimate the statistical parameters of the fracture sets were given by Fox et al. (2007), but these are not presented as individual fracture sets, nor are any plots given that show the expected distributions of poles, for the fitted parameters, without effects of sampling bias. In Chapter 6 of Fox et al., plots are given which show predicted and observed distributions of fracture poles for directional samples along near-vertical boreholes (one is reproduced here, for example as Figure A2.6), but these are not directly comparable with the plots presented here due to directional sampling bias effects.

The following is a printout of the results of fitting Fisher distribution parameters to the fracture poles for each fracture set in each of the 10 realizations of the DFN model. For each of the 15 sets and each realization, the results of the statistical fitting are given in the following format:

Column 1: Set #  
Column 2: Number of fractures in this set (N = ...)  
Columns 3-5: Fitted mean pole expressed as a unit vector in Cartesian (x,y,z) coordinates  
Columns 6-8: Fitted mean pole (trend, plunge) +/- spherical standard error  
Column 9: 95% confidence cone in degrees  
Column 10: Estimated Fisher concentration parameter  $\kappa$

The sets are numbered in the same order as they are listed in Table A2.1, and as they appear in the stereonet plots in Figures A2.3 through A2.5. For each fracture set, the specified mean orientation and Fisher concentration parameter are given for comparison with the values estimated based on the realizations.

**Table A2.2.** Specified mean orientation and Fisher concentration parameter for each fracture set in the realizations. Set 1 to 6.

Set 1 specified mean orientation: (314.9, 1.3)  $\kappa$  20.94  
Set 1 (N = 217483) -0.705367 -0.708515 -0.021525 (314.87, 1.23) +/- 0.000676 95% cone 0.067o  $\kappa$  21.12  
Set 1 (N = 218670) -0.705402 -0.708470 -0.021871 (314.88, 1.25) +/- 0.000673 95% cone 0.067o  $\kappa$  21.17  
Set 1 (N = 216945) -0.705183 -0.708658 -0.022827 (314.86, 1.31) +/- 0.000677 95% cone 0.067o  $\kappa$  21.13  
Set 1 (N = 217950) -0.705368 -0.708484 -0.022490 (314.87, 1.29) +/- 0.000675 95% cone 0.067o  $\kappa$  21.11  
Set 1 (N = 217465) -0.705293 -0.708571 -0.022105 (314.87, 1.27) +/- 0.000677 95% cone 0.067o  $\kappa$  21.07  
Set 1 (N = 217513) -0.704880 -0.708980 -0.022164 (314.83, 1.27) +/- 0.000677 95% cone 0.067o  $\kappa$  21.05  
Set 1 (N = 216288) -0.704537 -0.709311 -0.022490 (314.81, 1.29) +/- 0.000678 95% cone 0.067o  $\kappa$  21.10  
Set 1 (N = 216731) -0.704605 -0.709232 -0.022840 (314.81, 1.31) +/- 0.000677 95% cone 0.067o  $\kappa$  21.15  
Set 1 (N = 218568) -0.705001 -0.708876 -0.021647 (314.84, 1.24) +/- 0.000673 95% cone 0.067o  $\kappa$  21.18  
Set 1 (N = 218689) -0.705812 -0.708063 -0.021821 (314.91, 1.25) +/- 0.000674 95% cone 0.067o  $\kappa$  21.11

Set 2 specified mean orientation: (270.1, 5.3)  $\kappa$  21.34  
Set 2 (N = 149237) -0.003782 -0.995753 -0.091985 (270.22, 5.28) +/- 0.000807 95% cone 0.080o  $\kappa$  21.56  
Set 2 (N = 149957) -0.004200 -0.995762 -0.091871 (270.24, 5.27) +/- 0.000808 95% cone 0.080o  $\kappa$  21.43  
Set 2 (N = 149328) -0.004199 -0.995717 -0.092353 (270.24, 5.30) +/- 0.000808 95% cone 0.080o  $\kappa$  21.53  
Set 2 (N = 148635) -0.004349 -0.995783 -0.091638 (270.25, 5.26) +/- 0.000811 95% cone 0.080o  $\kappa$  21.46  
Set 2 (N = 148829) -0.004103 -0.995785 -0.091623 (270.24, 5.26) +/- 0.000811 95% cone 0.080o  $\kappa$  21.45  
Set 2 (N = 149967) -0.004107 -0.995854 -0.090868 (270.24, 5.21) +/- 0.000806 95% cone 0.080o  $\kappa$  21.52  
Set 2 (N = 150191) -0.003443 -0.995839 -0.091065 (270.20, 5.22) +/- 0.000804 95% cone 0.080o  $\kappa$  21.63  
Set 2 (N = 149038) -0.004884 -0.995771 -0.091743 (270.28, 5.26) +/- 0.000809 95% cone 0.080o  $\kappa$  21.49  
Set 2 (N = 149920) -0.004288 -0.995893 -0.090434 (270.25, 5.19) +/- 0.000807 95% cone 0.080o  $\kappa$  21.51  
Set 2 (N = 150703) -0.003531 -0.995796 -0.091536 (270.20, 5.25) +/- 0.000807 95% cone 0.080o  $\kappa$  21.40

Set 3 specified mean orientation: (230.1, 4.6)  $\kappa$  15.7  
Set 3 (N = 158491) 0.641652 -0.762792 -0.080193 (229.93, 4.60) +/- 0.000927 95% cone 0.092o  $\kappa$  15.67  
Set 3 (N = 159001) 0.641208 -0.763377 -0.078157 (229.97, 4.48) +/- 0.000923 95% cone 0.092o  $\kappa$  15.75  
Set 3 (N = 158058) 0.640965 -0.763440 -0.079524 (229.98, 4.56) +/- 0.000927 95% cone 0.092o  $\kappa$  15.72  
Set 3 (N = 159610) 0.641469 -0.763045 -0.079252 (229.95, 4.55) +/- 0.000920 95% cone 0.091o  $\kappa$  15.80  
Set 3 (N = 157688) 0.640973 -0.763525 -0.078637 (229.99, 4.51) +/- 0.000930 95% cone 0.092o  $\kappa$  15.66  
Set 3 (N = 159131) 0.641494 -0.763042 -0.079065 (229.95, 4.53) +/- 0.000924 95% cone 0.092o  $\kappa$  15.73  
Set 3 (N = 157567) 0.641838 -0.762697 -0.079603 (229.92, 4.57) +/- 0.000928 95% cone 0.092o  $\kappa$  15.74  
Set 3 (N = 159887) 0.641283 -0.763184 -0.079409 (229.96, 4.55) +/- 0.000919 95% cone 0.091o  $\kappa$  15.80  
Set 3 (N = 158894) 0.640656 -0.763734 -0.079184 (230.01, 4.54) +/- 0.000922 95% cone 0.091o  $\kappa$  15.82  
Set 3 (N = 159350) 0.642229 -0.762341 -0.079861 (229.89, 4.58) +/- 0.000922 95% cone 0.091o  $\kappa$  15.78

Set 4 specified mean orientation: ( 0.8, 87.3)  $\kappa$  17.42  
Set 4 (N = 92766) -0.048282 0.000089 -0.998834 ( 0.11,87.23) +/- 0.001171 95% cone 0.116o  $\kappa$  16.74  
Set 4 (N = 92982) -0.048888 -0.000089 -0.998804 (359.90,87.20) +/- 0.001172 95% cone 0.116o  $\kappa$  16.69  
Set 4 (N = 93034) -0.048305 0.002522 -0.998829 ( 2.99,87.23) +/- 0.001171 95% cone 0.116o  $\kappa$  16.68  
Set 4 (N = 93179) -0.049421 -0.000864 -0.998778 (359.00,87.17) +/- 0.001170 95% cone 0.116o  $\kappa$  16.69  
Set 4 (N = 93264) -0.049135 0.000363 -0.998792 ( 0.42,87.18) +/- 0.001171 95% cone 0.116o  $\kappa$  16.65  
Set 4 (N = 93518) -0.050392 0.000915 -0.998729 ( 1.04,87.11) +/- 0.001168 95% cone 0.116o  $\kappa$  16.68  
Set 4 (N = 93548) -0.048272 0.000081 -0.998834 ( 0.10,87.23) +/- 0.001169 95% cone 0.116o  $\kappa$  16.65  
Set 4 (N = 93666) -0.049969 -0.000911 -0.998750 (358.96,87.14) +/- 0.001167 95% cone 0.116o  $\kappa$  16.69  
Set 4 (N = 93994) -0.048551 0.000118 -0.998821 ( 0.14,87.22) +/- 0.001165 95% cone 0.116o  $\kappa$  16.69  
Set 4 (N = 94052) -0.047359 -0.000051 -0.998878 (359.94,87.29) +/- 0.001165 95% cone 0.115o  $\kappa$  16.70

Set 5 specified mean orientation: (157.5, 3.1)  $\kappa$  34.11  
Set 5 (N = 14264) 0.922720 0.382026 -0.051415 (157.51, 2.95) +/- 0.002052 95% cone 0.204o  $\kappa$  34.28  
Set 5 (N = 14390) 0.923319 0.380211 -0.054044 (157.62, 3.10) +/- 0.002053 95% cone 0.204o  $\kappa$  33.99  
Set 5 (N = 14405) 0.922533 0.382040 -0.054579 (157.50, 3.13) +/- 0.002045 95% cone 0.203o  $\kappa$  34.21  
Set 5 (N = 14473) 0.923724 0.379018 -0.055482 (157.69, 3.18) +/- 0.002044 95% cone 0.203o  $\kappa$  34.07  
Set 5 (N = 14512) 0.923549 0.379692 -0.053766 (157.65, 3.08) +/- 0.002028 95% cone 0.201o  $\kappa$  34.52  
Set 5 (N = 14553) 0.921979 0.383423 -0.054228 (157.42, 3.11) +/- 0.002035 95% cone 0.202o  $\kappa$  34.18  
Set 5 (N = 14578) 0.922446 0.382235 -0.054687 (157.49, 3.13) +/- 0.002027 95% cone 0.201o  $\kappa$  34.39  
Set 5 (N = 14588) 0.922784 0.381997 -0.050479 (157.51, 2.89) +/- 0.002034 95% cone 0.202o  $\kappa$  34.15  
Set 5 (N = 14632) 0.922160 0.383050 -0.053787 (157.44, 3.08) +/- 0.002026 95% cone 0.201o  $\kappa$  34.31  
Set 5 (N = 14665) 0.923591 0.379592 -0.053750 (157.66, 3.08) +/- 0.002034 95% cone 0.202o  $\kappa$  33.97

Set 6 specified mean orientation: ( 0.4, 11.9)  $\kappa$  13.89  
Set 6 (N = 10782) -0.978498 0.012791 -0.205861 ( 0.75,11.88) +/- 0.003781 95% cone 0.375o  $\kappa$  13.98  
Set 6 (N = 10940) -0.979657 0.006546 -0.200573 ( 0.38,11.57) +/- 0.003751 95% cone 0.372o  $\kappa$  14.00  
Set 6 (N = 10958) -0.979431 0.003122 -0.201754 ( 0.18,11.64) +/- 0.003752 95% cone 0.372o  $\kappa$  13.97  
Set 6 (N = 11008) -0.979975 0.010535 -0.198841 ( 0.62,11.47) +/- 0.003711 95% cone 0.368o  $\kappa$  14.17  
Set 6 (N = 11047) -0.978937 0.004457 -0.204112 ( 0.26,11.78) +/- 0.003702 95% cone 0.367o  $\kappa$  14.23  
Set 6 (N = 11071) -0.979544 0.007708 -0.201085 ( 0.45,11.60) +/- 0.003711 95% cone 0.368o  $\kappa$  14.11  
Set 6 (N = 11083) -0.979951 0.006634 -0.199128 ( 0.39,11.49) +/- 0.003732 95% cone 0.370o  $\kappa$  13.95  
Set 6 (N = 11110) -0.979638 0.007224 -0.200641 ( 0.42,11.57) +/- 0.003675 95% cone 0.364o  $\kappa$  14.32  
Set 6 (N = 11168) -0.979004 0.006300 -0.203742 ( 0.37,11.76) +/- 0.003720 95% cone 0.369o  $\kappa$  13.94  
Set 6 (N = 11195) -0.979733 0.004207 -0.200266 ( 0.25,11.55) +/- 0.003729 95% cone 0.370o  $\kappa$  13.86

**Table A2.2.** Cont. Specified mean orientation and Fisher concentration parameter for each fracture set in the realizations. Set 1 to 15.

Set 7 specified mean orientation: (293.8, 0.0) κ 21.79  
Set 7 (N = 34806) 0.402473 0.915430 -0.001559 (113.73, 0.09) +/- 0.001652 95% cone 0.164o κ 22.06  
Set 7 (N = 34907) 0.404687 0.914455 -0.000257 (113.87, 0.01) +/- 0.001656 95% cone 0.164o κ 21.90  
Set 7 (N = 35056) 0.403523 0.914969 -0.001015 (113.80, 0.06) +/- 0.001655 95% cone 0.164o κ 21.82  
Set 7 (N = 35094) 0.403357 0.915041 -0.001449 (113.79, 0.08) +/- 0.001653 95% cone 0.164o κ 21.86  
Set 7 (N = 35096) 0.401789 0.915731 -0.001145 (113.69, 0.07) +/- 0.001642 95% cone 0.163o κ 22.15  
Set 7 (N = 35103) 0.404755 0.914423 -0.001957 (113.88, 0.11) +/- 0.001647 95% cone 0.163o κ 22.00  
Set 7 (N = 35394) -0.403345 -0.915048 -0.000592 (293.79, 0.03) +/- 0.001644 95% cone 0.163o κ 21.90  
Set 7 (N = 35578) 0.402753 0.915307 -0.001413 (113.75, 0.08) +/- 0.001641 95% cone 0.163o κ 21.86  
Set 7 (N = 35638) -0.402555 -0.915396 -0.000199 (293.74, 0.01) +/- 0.001632 95% cone 0.162o κ 22.07  
Set 7 (N = 35895) 0.403850 0.914824 -0.001427 (113.82, 0.08) +/- 0.001629 95% cone 0.162o κ 22.01

Set 8 specified mean orientation: (164.0, 52.6) κ 35.43  
Set 8 (N = 11872) 0.590194 0.165353 -0.790145 (164.35, 52.20) +/- 0.002221 95% cone 0.220o κ 35.13  
Set 8 (N = 12123) 0.588715 0.169345 -0.790403 (163.95, 52.22) +/- 0.002186 95% cone 0.217o κ 35.51  
Set 8 (N = 12136) 0.591185 0.169811 -0.788457 (163.97, 52.04) +/- 0.002199 95% cone 0.218o κ 35.07  
Set 8 (N = 12303) 0.589854 0.167117 -0.790028 (164.18, 52.19) +/- 0.002170 95% cone 0.215o κ 35.52  
Set 8 (N = 12369) 0.590193 0.166146 -0.789980 (164.28, 52.18) +/- 0.002174 95% cone 0.216o κ 35.21  
Set 8 (N = 12447) 0.590006 0.168319 -0.789659 (164.08, 52.15) +/- 0.002160 95% cone 0.214o κ 35.45  
Set 8 (N = 12560) 0.588238 0.167893 -0.791068 (164.07, 52.29) +/- 0.002154 95% cone 0.214o κ 35.32  
Set 8 (N = 12562) 0.589606 0.168232 -0.789976 (164.07, 52.18) +/- 0.002149 95% cone 0.213o κ 35.50  
Set 8 (N = 12623) 0.589600 0.166346 -0.790380 (164.24, 52.22) +/- 0.002140 95% cone 0.212o κ 35.61  
Set 8 (N = 12655) 0.588598 0.168001 -0.790777 (164.07, 52.26) +/- 0.002137 95% cone 0.212o κ 35.62

Set 9 specified mean orientation: (337.9, 52.9) κ 17.08  
Set 9 (N = 10092) -0.571051 -0.233675 -0.786954 (337.75, 51.90) +/- 0.003533 95% cone 0.350o κ 16.88  
Set 9 (N = 10119) -0.564580 -0.230415 -0.792564 (337.80, 52.43) +/- 0.003552 95% cone 0.352o κ 16.65  
Set 9 (N = 10216) -0.566973 -0.227996 -0.791555 (338.09, 52.33) +/- 0.003473 95% cone 0.344o κ 17.23  
Set 9 (N = 10218) -0.567758 -0.233906 -0.789265 (337.61, 52.12) +/- 0.003502 95% cone 0.347o κ 16.96  
Set 9 (N = 10223) -0.567480 -0.234825 -0.789192 (337.52, 52.11) +/- 0.003462 95% cone 0.343o κ 17.31  
Set 9 (N = 10230) -0.565904 -0.230813 -0.791504 (337.81, 52.33) +/- 0.003502 95% cone 0.347o κ 16.94  
Set 9 (N = 10273) -0.566295 -0.229588 -0.791580 (337.93, 52.33) +/- 0.003470 95% cone 0.344o κ 17.16  
Set 9 (N = 10399) -0.568053 -0.230993 -0.789910 (337.87, 52.18) +/- 0.003485 95% cone 0.346o κ 16.83  
Set 9 (N = 10445) -0.568196 -0.236306 -0.788234 (337.42, 52.02) +/- 0.003455 95% cone 0.343o κ 17.03  
Set 9 (N = 10471) -0.568709 -0.228087 -0.790282 (338.15, 52.21) +/- 0.003446 95% cone 0.342o κ 17.09

Set 10 specified mean orientation: (125.7, 10.1) κ 45.05  
Set 10 (N = 79407) 0.574198 0.799948 -0.174298 (125.67, 10.04) +/- 0.000755 95% cone 0.075o κ 45.17  
Set 10 (N = 79495) 0.573727 0.800213 -0.174629 (125.64, 10.06) +/- 0.000756 95% cone 0.075o κ 44.98  
Set 10 (N = 79584) 0.574554 0.799723 -0.174159 (125.70, 10.03) +/- 0.000754 95% cone 0.075o κ 45.20  
Set 10 (N = 79663) 0.574582 0.799631 -0.174489 (125.70, 10.05) +/- 0.000754 95% cone 0.075o κ 45.18  
Set 10 (N = 80166) 0.575301 0.799170 -0.174228 (125.75, 10.03) +/- 0.000754 95% cone 0.075o κ 44.91  
Set 10 (N = 80287) 0.574685 0.799507 -0.174715 (125.71, 10.06) +/- 0.000754 95% cone 0.075o κ 44.81  
Set 10 (N = 80331) 0.574140 0.799871 -0.174842 (125.67, 10.07) +/- 0.000750 95% cone 0.074o κ 45.28  
Set 10 (N = 80428) 0.574870 0.799445 -0.174389 (125.72, 10.04) +/- 0.000749 95% cone 0.074o κ 45.29  
Set 10 (N = 80548) 0.575146 0.799356 -0.173885 (125.74, 10.01) +/- 0.000752 95% cone 0.075o κ 44.92  
Set 10 (N = 80822) 0.575242 0.799169 -0.174429 (125.75, 10.05) +/- 0.000749 95% cone 0.074o κ 45.14

Set 11 specified mean orientation: ( 91.0, 4.1) κ 19.49  
Set 11 (N = 53333) 0.015200 0.997423 -0.070120 ( 90.87, 4.02) +/- 0.001420 95% cone 0.141o κ 19.59  
Set 11 (N = 54169) 0.013767 0.997594 -0.067948 ( 90.79, 3.90) +/- 0.001407 95% cone 0.140o κ 19.65  
Set 11 (N = 54187) 0.014355 0.997411 -0.070470 ( 90.82, 4.04) +/- 0.001403 95% cone 0.139o κ 19.76  
Set 11 (N = 54326) 0.015662 0.997391 -0.070466 ( 90.90, 4.04) +/- 0.001406 95% cone 0.139o κ 19.63  
Set 11 (N = 54394) 0.015073 0.997486 -0.069246 ( 90.87, 3.97) +/- 0.001404 95% cone 0.139o κ 19.66  
Set 11 (N = 54663) 0.013884 0.997430 -0.070292 ( 90.80, 4.03) +/- 0.001395 95% cone 0.138o κ 19.80  
Set 11 (N = 54709) 0.015818 0.997371 -0.070715 ( 90.91, 4.06) +/- 0.001402 95% cone 0.139o κ 19.61  
Set 11 (N = 54951) 0.015478 0.997461 -0.069517 ( 90.89, 3.99) +/- 0.001395 95% cone 0.138o κ 19.71  
Set 11 (N = 54984) 0.016173 0.997275 -0.071979 ( 90.93, 4.13) +/- 0.001395 95% cone 0.138o κ 19.69  
Set 11 (N = 54998) 0.014048 0.997358 -0.071273 ( 90.81, 4.09) +/- 0.001402 95% cone 0.139o κ 19.49

Set 12 specified mean orientation: ( 34.1, 0.8) κ 16.13  
Set 12 (N = 56754) -0.827484 0.561317 -0.013916 ( 34.15, 0.80) +/- 0.001516 95% cone 0.150o κ 16.32  
Set 12 (N = 56786) -0.828016 0.560532 -0.013867 ( 34.10, 0.79) +/- 0.001521 95% cone 0.151o κ 16.23  
Set 12 (N = 57032) -0.827271 0.561605 -0.014917 ( 34.17, 0.85) +/- 0.001515 95% cone 0.150o κ 16.28  
Set 12 (N = 57091) -0.827386 0.561451 -0.014325 ( 34.16, 0.82) +/- 0.001515 95% cone 0.150o κ 16.26  
Set 12 (N = 57100) -0.826475 0.562778 -0.014863 ( 34.25, 0.85) +/- 0.001518 95% cone 0.151o κ 16.20  
Set 12 (N = 57236) -0.827309 0.561595 -0.013074 ( 34.17, 0.75) +/- 0.001512 95% cone 0.150o κ 16.29  
Set 12 (N = 57252) -0.826980 0.562037 -0.014769 ( 34.20, 0.85) +/- 0.001507 95% cone 0.149o κ 16.38  
Set 12 (N = 57283) -0.828336 0.560045 -0.014464 ( 34.06, 0.83) +/- 0.001513 95% cone 0.150o κ 16.26  
Set 12 (N = 57817) -0.826063 0.563412 -0.013694 ( 34.30, 0.78) +/- 0.001504 95% cone 0.149o κ 16.29  
Set 12 (N = 57834) -0.826908 0.562153 -0.014368 ( 34.21, 0.82) +/- 0.001501 95% cone 0.149o κ 16.34

**Table A2.2.** Cont. Specified mean orientation and Fisher concentration parameter for each fracture set in the realizations. Set 1 to 15.

Set 13 specified mean orientation: ( 84.3, 71.3) κ 10.78  
Set 13 (N = 23919) -0.036929 0.331428 -0.942758 ( 83.64,70.52) +/- 0.002979 95% cone 0.295o κ 10.43  
Set 13 (N = 23933) -0.032153 0.332179 -0.942668 ( 84.47,70.50) +/- 0.002993 95% cone 0.297o κ 10.33  
Set 13 (N = 23946) -0.033365 0.331422 -0.942893 ( 84.25,70.54) +/- 0.002993 95% cone 0.297o κ 10.33  
Set 13 (N = 24079) -0.034697 0.331964 -0.942654 ( 84.03,70.50) +/- 0.002964 95% cone 0.294o κ 10.45  
Set 13 (N = 24239) -0.033482 0.331681 -0.942797 ( 84.24,70.53) +/- 0.002967 95% cone 0.294o κ 10.39  
Set 13 (N = 24282) -0.031762 0.331391 -0.942959 ( 84.53,70.55) +/- 0.002952 95% cone 0.293o κ 10.46  
Set 13 (N = 24400) -0.033702 0.331138 -0.942980 ( 84.19,70.56) +/- 0.002963 95% cone 0.294o κ 10.34  
Set 13 (N = 24448) -0.033263 0.333879 -0.942029 ( 84.31,70.40) +/- 0.002961 95% cone 0.294o κ 10.33  
Set 13 (N = 24873) -0.032676 0.331148 -0.943013 ( 84.36,70.56) +/- 0.002920 95% cone 0.290o κ 10.44  
Set 13 (N = 24931) -0.034047 0.333148 -0.942260 ( 84.16,70.43) +/- 0.002917 95% cone 0.289o κ 10.43

Set 14 specified mean orientation: (155.4, 8.3) κ 20.83  
Set 14 (N = 3611) 0.899763 0.412020 -0.143760 (155.40, 8.27) +/- 0.005269 95% cone 0.523o κ 20.94  
Set 14 (N = 3648) 0.900117 0.411937 -0.141765 (155.41, 8.15) +/- 0.005262 95% cone 0.522o κ 20.79  
Set 14 (N = 3651) 0.901151 0.410844 -0.138326 (155.49, 7.95) +/- 0.005314 95% cone 0.527o κ 20.41  
Set 14 (N = 3672) 0.900836 0.408246 -0.147749 (155.62, 8.50) +/- 0.005224 95% cone 0.518o κ 20.99  
Set 14 (N = 3694) 0.896532 0.419608 -0.141983 (154.92, 8.16) +/- 0.005137 95% cone 0.509o κ 21.48  
Set 14 (N = 3697) 0.898372 0.415449 -0.142585 (155.18, 8.20) +/- 0.005132 95% cone 0.509o κ 21.56  
Set 14 (N = 3744) 0.903369 0.402932 -0.146866 (155.96, 8.45) +/- 0.005203 95% cone 0.516o κ 20.75  
Set 14 (N = 3761) 0.901850 0.404540 -0.151705 (155.84, 8.73) +/- 0.005149 95% cone 0.511o κ 21.02  
Set 14 (N = 3813) 0.900456 0.409241 -0.147311 (155.56, 8.47) +/- 0.005081 95% cone 0.504o κ 21.34  
Set 14 (N = 3815) 0.901089 0.409221 -0.143448 (155.58, 8.25) +/- 0.005185 95% cone 0.514o κ 20.48

Set 15 specified mean orientation: ( 0.0, 47.5) κ 12.71  
Set 15 (N = 16012) -0.684260 0.002887 -0.729232 ( 0.24,46.82) +/- 0.003253 95% cone 0.323o κ 12.81  
Set 15 (N = 16033) -0.690087 -0.004419 -0.723713 (359.63,46.36) +/- 0.003259 95% cone 0.323o κ 12.75  
Set 15 (N = 16073) -0.682783 0.002416 -0.730618 ( 0.20,46.94) +/- 0.003263 95% cone 0.324o κ 12.68  
Set 15 (N = 16086) -0.684109 -0.000439 -0.729380 (359.96,46.83) +/- 0.003286 95% cone 0.326o κ 12.50  
Set 15 (N = 16160) -0.685728 -0.000161 -0.727858 (359.99,46.71) +/- 0.003247 95% cone 0.322o κ 12.74  
Set 15 (N = 16264) -0.684765 -0.001680 -0.728762 (359.86,46.78) +/- 0.003253 95% cone 0.323o κ 12.62  
Set 15 (N = 16277) -0.685173 0.000995 -0.728380 ( 0.08,46.75) +/- 0.003220 95% cone 0.319o κ 12.85  
Set 15 (N = 16278) -0.685253 -0.000745 -0.728304 (359.94,46.74) +/- 0.003234 95% cone 0.321o κ 12.74  
Set 15 (N = 16399) -0.687238 0.000530 -0.726432 ( 0.04,46.59) +/- 0.003215 95% cone 0.319o κ 12.81  
Set 15 (N = 16604) -0.688066 0.000057 -0.725649 ( 0.00,46.52) +/- 0.003178 95% cone 0.315o κ 12.92

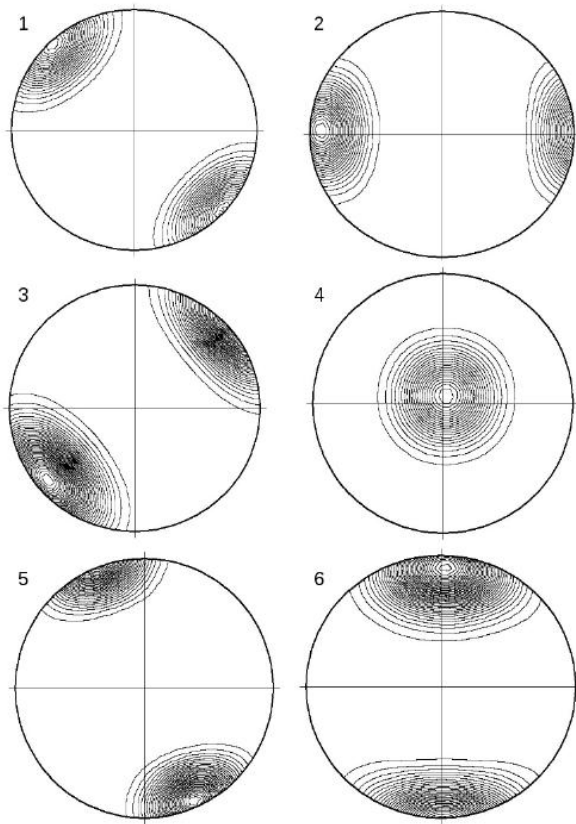


**Figure A2.3.** Equal-area stereonet plots of simulated fracture pole directions for the first six fracture sets in fracture domain FFM01, r0-fixed model: (1) NE global, (2) NS global, (3) NW global, (4) SH global, (5) ENE local, and (6) EW local.

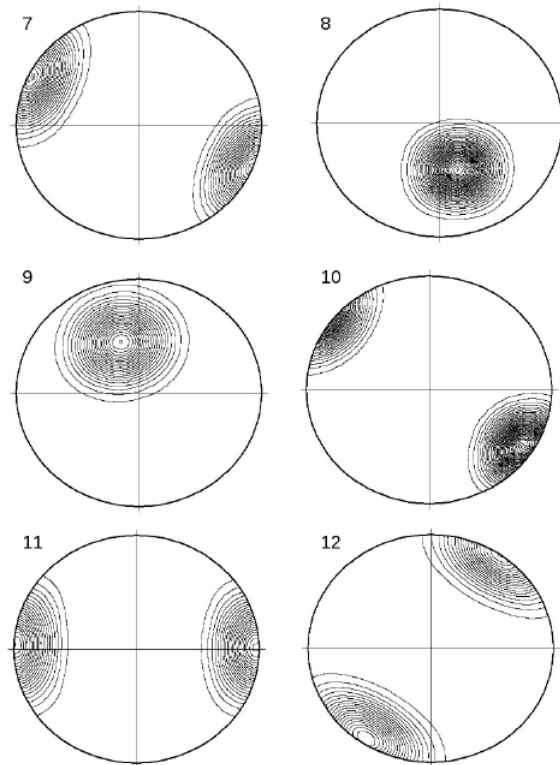


**Figure A2.4.** Equal-area stereonet plots of simulated fracture pole directions for the last three fracture sets in fracture domain FFM01, r0-fixed model: (7) NNE local, (8) SH2 local, (9) SH3 local; plus the first three sets of FFM06: (10) NE global, (11) NS global), and (12) NW global.

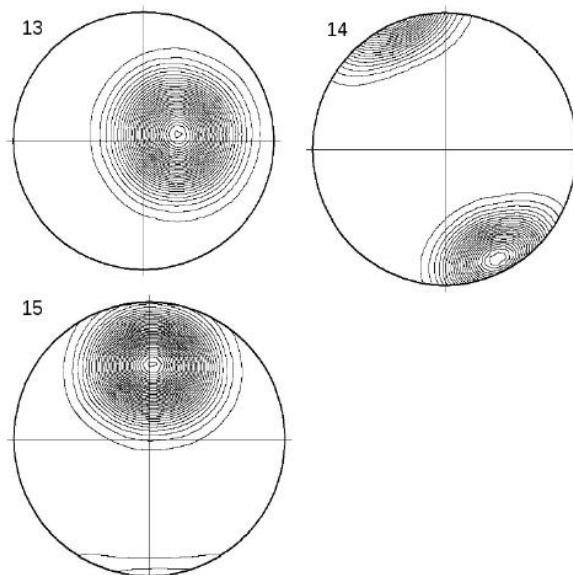


**Figure A2.5.** Equal-area stereonet plots of simulated fracture pole directions for the last three fracture sets in fracture domain FFM06: (13) SH global, (14) ENE local, and (15) SH2 local.

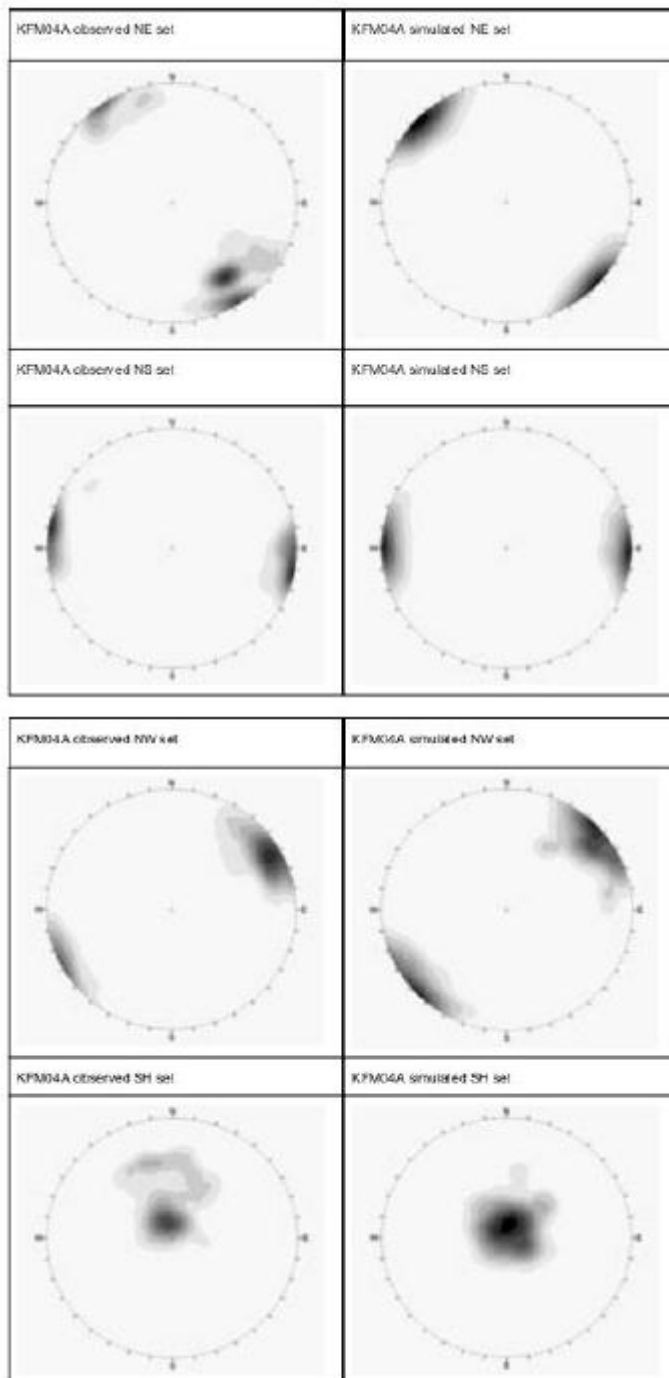


**Figure A2.6.** Observed vs. predicted fracture poles in borehole KFM04, Fracture Domain FFM01 as reproduced from Fox et al. (2007). Observed fracture poles are shown on the left while those predicted by stochastic simulations by Fox et al. (2007) are shown on the right. The observations and simulations both incorporate directional sampling bias along the borehole. However, the orientations can be compared in general terms with the global sets shown as Sets 1-4 in Figure A2.3.

### **Quality Check 3: Comparison of expected and simulated $P_{21}$ fracture intensity on the sampling plane**

The third main check of quality is to compare the observed values of fracture intensity as measured in the same 2-D cross-sections for which data area delivered, in terms of the  $P_{21}$  fracture intensity (trace length per unit area).

This can be estimated from the volumetric fracture intensity  $P_{32}$ , after correcting for the effects of truncating the fracture size distribution by thinning out the fractures smaller than 50 m radius, and the orientation bias that results from the orientation of the horizontal sampling plane relative to the fractures in each fracture set. The orientation bias is quantified by the factor  $C_{23}$  as defined by Wang (2005; see Geier, 2014a for details and method of calculation). The results are listed in Table A2.3.

The expected  $P_{21}$  values can be compared with the total fracture trace length per unit area of the cross-section. This needs to be taken in the portion of the model within the volume that has been focused on for the repository simulations, to avoid other censoring effects.

The results as shown in Figure A2.6 are generally intermediate to the expected values for fracture domains FFM01 and FFM06. The median value of the realizations is about 10% above the area weighted average of the expected values for the two domains. Some upward bias can be expected for the combined model, due to the fact that fractures simulated with centers inside the FFM06 domain can extend into the FFM01 domain, and due to the simplistic method of calculation which includes all traces in the sampling plane, even in the fringe outside of the repository footprint.

Therefore this match is judged as adequate as a check that the results are reasonable. A more precise, direct evaluation of  $P_{21}$  would require separate treatment of fractures from the two domains, and calculation of truncated trace lengths within the precise boundaries of the repository footprint. While such a calculation is achievable, it requires more complex steps which would diminish its value as a simple, direct verification procedure. It is noted that the more precise quantitative checks of  $P_{32}$  and the orientation distribution, as given in previous sections of this memorandum, also are expected to constrain  $P_{21}$ , and that direct calculations of  $P_{21}$  for more well-constrained 50 m block geometries, in a related task, agreed within 1% of the expected values.

**Table A2.3.** Parameters for fracture sets for the  $r_0$ -fixed alternative, Calculation Case  $r_2$ , and resulting values of truncated  $P_{32}$  (for minimum fracture radius of 50 m), and corresponding values of the geometric factor  $C_{23}$  and  $P_{21}$ .

	Mean pole trend	Mean pole plunge	Fisher concentration $K$	$P_{32}$ (unscaled)	$P_{32}$ (truncated)	$\rho$	$1/C_{23}$	$P_{21}$
<b>FFM01</b>								
NE global	314.9	1.3	20.94	1.733	0.0081	88.7	0.9761	0.0079
NS global	270.1	5.3	21.34	1.292	0.005	84.7	0.9729	0.0048
NW global	230.1	4.6	15.7	0.948	0.0091	85.4	0.9662	0.0088
SH global	0.8	87.3	17.42	0.624	0.0073	2.7	0.2965	0.0022
ENE local	157.5	3.1	34.11	0.256	0.0002	86.9	0.9839	0.0002
EW local	0.4	11.9	13.89	0.169	0.0002	78.1	0.9457	0.0002
NNE local	293.8	0	21.79	0.658	0.0005	90	0.9774	0.0004
SH2 local	164	52.6	35.43	0.081	0.0008	37.4	0.6147	0.0005
SH3 local	337.9	52.9	17.08	0.067	0.0006	37.1	0.6206	0.0004
Total					0.0318			0.0254
<b>FFM06</b>								
NE global	125.7	10.1	45.05	3.299	0.0097	79.9	0.974	0.0094
NS global	91	4.1	19.49	2.15	0.0067	85.9	0.9723	0.0065
NW global	34.1	0.8	16.13	1.608	0.0112	89.2	0.9698	0.0109
SH global	84.3	71.3	10.78	0.64	0.0075	18.7	0.4514	0.0034
ENE local	155.4	8.3	20.83	0.194	0.0003	81.7	0.9662	0.0003
SH2 local	0	47.5	12.71	0.429	0.0041	42.5	0.684	0.0028
Total					0.0395			0.0333

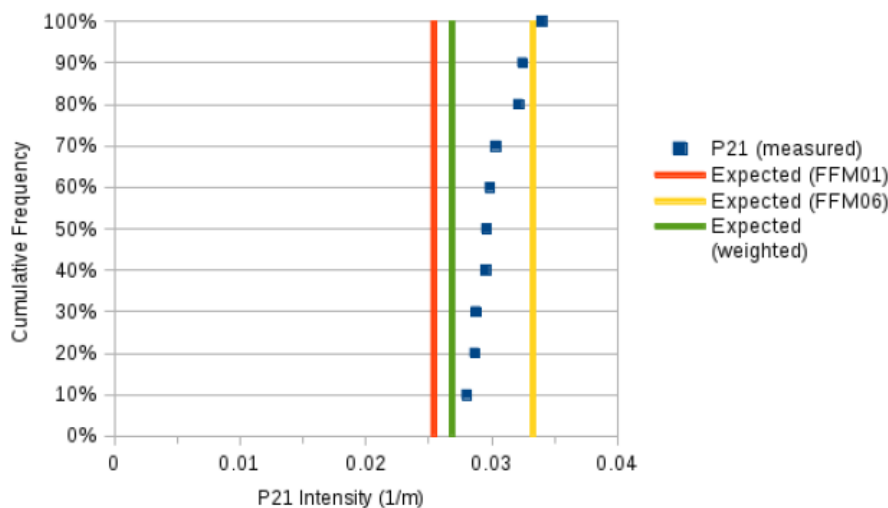


**Figure A2.6.** Measured vs. expected  $P_{21}$  values for ten realizations of the  $r_0$ -fixed model.

### **Plots of cross-sections**

Figures A2.7 through A2.16 give plots of fracture traces in the plane  $z = -465$  m resulting from Calculation Case  $r_2$ , for realizations 01 through 10. Figures on the right shows the realizations of the DFN implemented in the PFC model, where the fractures with trace length shorter than 125 m are eliminated.

Note that these cross sections represent fracture traces from the “thinned” datasets, i.e. after deleting fractures with radius  $r < 50$  m. However, fracture traces with half-lengths  $L/2 < 62.5$  m have not been deleted from these plots.

In all of these plots the spacing of yellow grid lines is 1 km in both directions. North is upward.

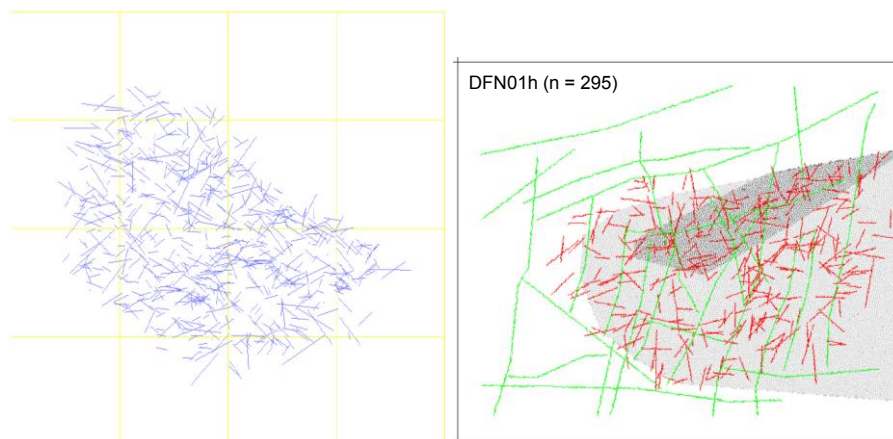


**Figure A2.7:** Fracture traces in the plane  $z = -465$  m for fractures with  $r > 50$  m in Calculation Case  $r2$ , Realization 01 (left) and PFC implementation (right).

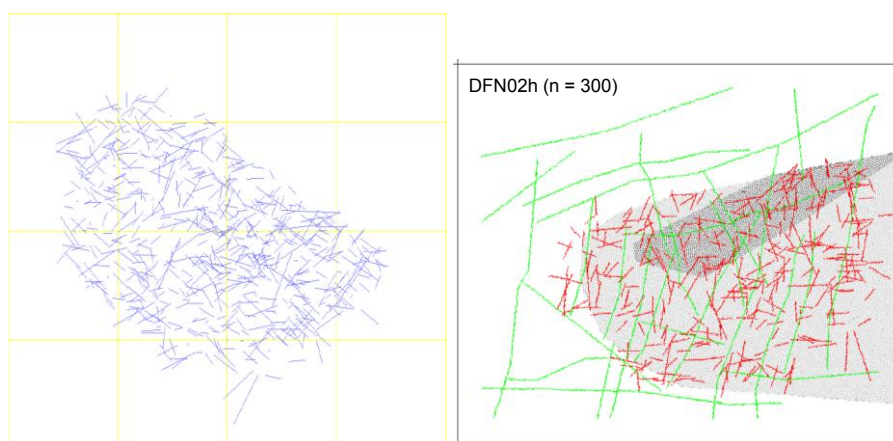


**Figure A2.8:** Fracture traces in the plane  $z = -465$  m for fractures with  $r > 50$  m in Calculation Case  $r2$ , Realization 02 and PFC implementation (right).

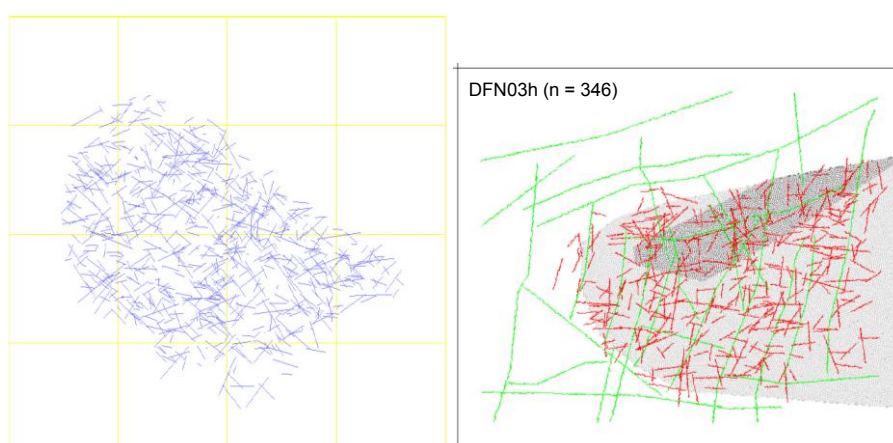


**Figure A2.9:** Fracture traces in the plane  $z = -465$  m for fractures with  $r > 50$  m in Calculation Case  $r2$ , Realization 03 and PFC implementation (right).

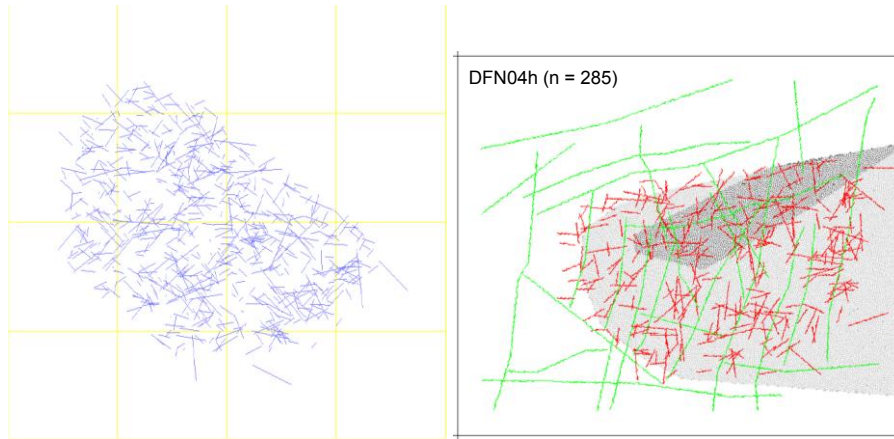


**Figure A2.10:** Fracture traces in the plane  $z = -465$  m for fractures with  $r > 50$  m in Calculation Case  $r_2$ , Realization 04 and PFC implementation (right).

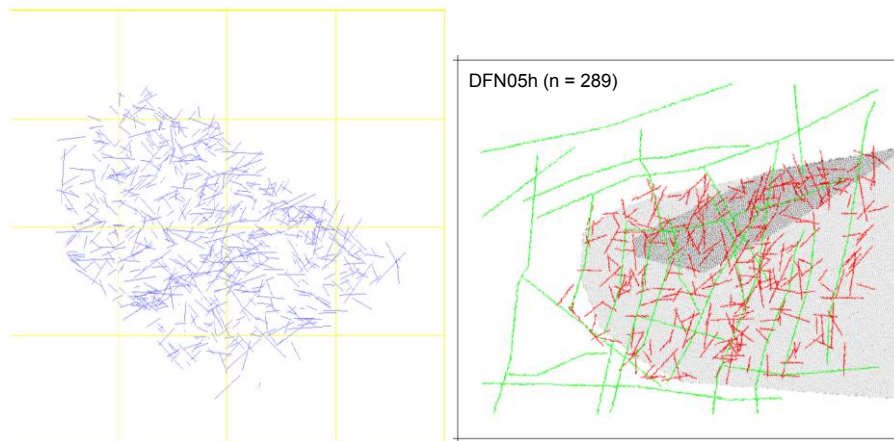


**Figure A2.11:** Fracture traces in the plane  $z = -465$  m for fractures with  $r > 50$  m in Calculation Case  $r_2$ , Realization 05 and PFC implementation (right).

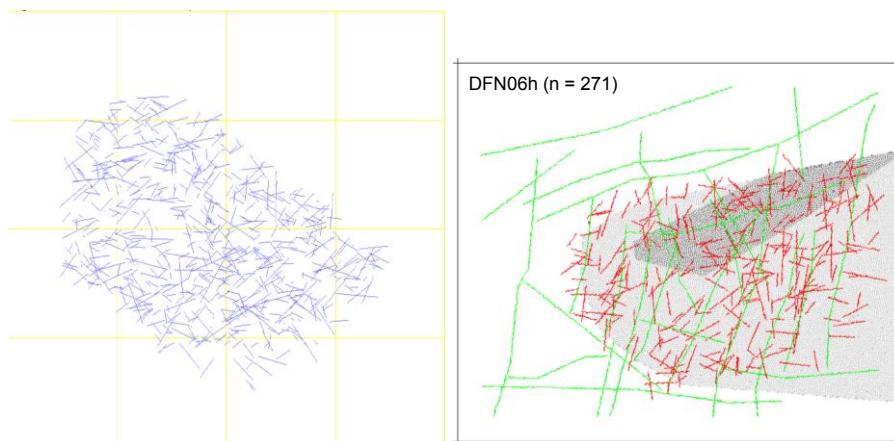


**Figure A2.12:** Fracture traces in the plane  $z = -465$  m for fractures with  $r > 50$  m in Calculation Case  $r_2$ , Realization 06 and PFC implementation (right).

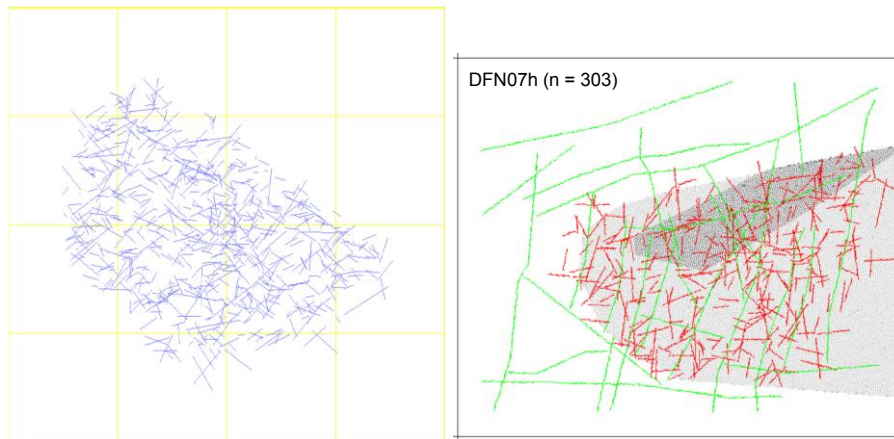


**Figure A2.13:** Fracture traces in the plane  $z = -465$  m for fractures with  $r > 50$  m in Calculation Case  $r_2$ , Realization 07 and PFC implementation (right).

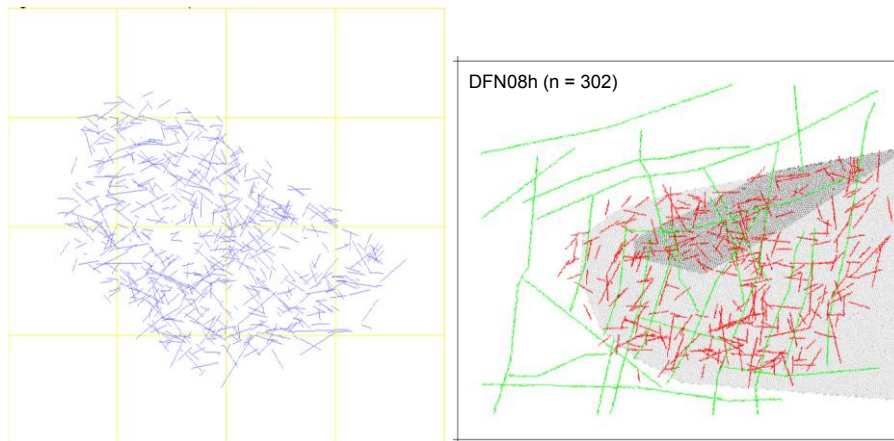


**Figure A2.14:** Fracture traces in the plane  $z = -465$  m for fractures with  $r > 50$  m in Calculation Case  $r_2$ , Realization 08 and PFC implementation (right).

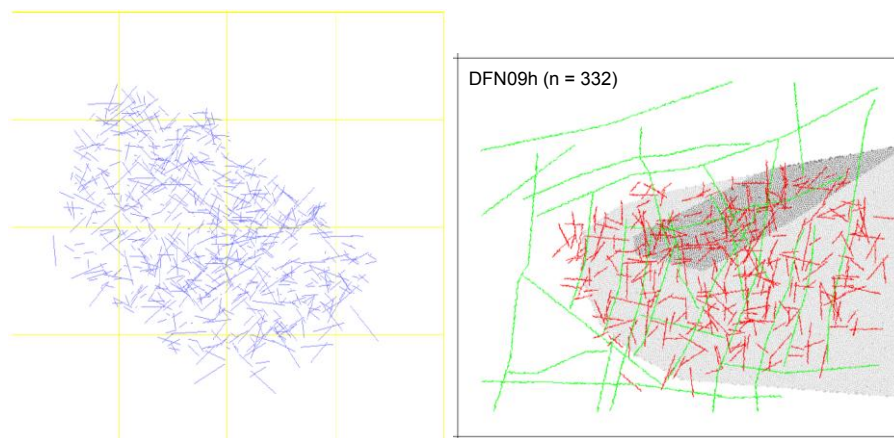


**Figure A2.15:** Fracture traces in the plane  $z = -465$  m for fractures with  $r > 50$  m in Calculation Case  $r_2$ , Realization 09 and PFC implementation (right).

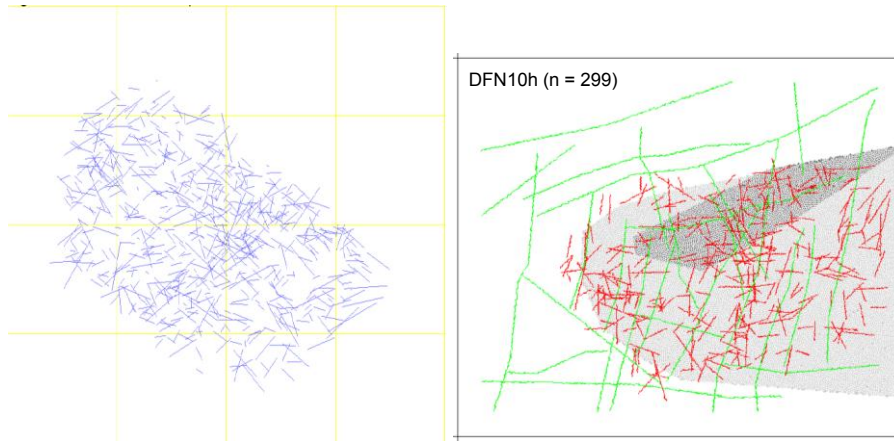


**Figure A2.16:** Fracture traces in the plane  $z = -465$  m for fractures with  $r > 50$  m in Calculation Case r2, Realization 10 and PFC implementation (right).

**References:**

Fox A, La Pointe P, Hermanson J, Ohman J, 2007. Statistical geological discrete fracture network model. Forsmark modelling stage 2.2. SKB R-07-46, Swedish Nuclear Fuel and Waste Management Company (SKB).

## Vertical sections

*Joel Geier, Clearwater Hardrock Consulting, Date of data delivery: 26 May 2014, Document date: 29 May 2014.*

This memorandum concerns the delivery of the following cross-section data files that were produced on 26 May 2014: SRGeoPFC\_r2\_##\_NWSE2dr.prn, where ## = 01, 02, ..., 10.

These cross-section data files were produced based on DFN simulations for the calculation of  $N_{crit}$  (the number of critical positions). Full documentation is given in an SSM Technical Note by Geier (2014a, in prep.). The DFN simulations used were the same as for the 11 Mar 2014 data delivery. The only difference is that the present data files are for vertical cross sections, in a plane striking nominally NW (N50W or S50E). The main parameters for generating fracture sets for these realizations are thus the same as for the 11 Mar 2014 delivery, as reproduced here in Table A2.4.

**Table A2.4.** Parameters for generation of fracture sets for the  $r_0$ -fixed alternative, Calculation Case r2.

	Mean pole trend (°)	Mean pole plunge (°)	$\kappa^1$	$r_0$ (m)	$k_r$	$P_{32}$ (unscaled)	$r_{max}$
FFM01							
NE global	314.9	1.3	20.94	0.039	2.72	1.733	564.2
NS global	270.1	5.3	21.34	0.039	2.75	1.292	564.2
NW global	230.1	4.6	15.70	0.039	2.61	0.948	564.2
SH global	0.8	87.3	17.42	0.039	2.58	0.624	564.2
ENE local	157.5	3.1	34.11	0.039	2.97	0.256	564.2
EW local	0.4	11.9	13.89	0.039	2.93	0.169	564.2
NNE local	293.8	0.0	21.79	0.039	3.00	0.658	564.2
SH2 local	164.0	52.6	35.43	0.039	2.61	0.081	564.2
SH3 local	337.9	52.9	17.08	0.039	2.61	0.067	564.2
FFM06							
NE global	125.7	10.1	45.05	0.039	2.79	3.299	564.2
NS global	91.0	4.1	19.49	0.039	2.78	2.150	564.2
NW global	34.1	0.8	16.13	0.039	2.66	1.608	564.2
SH global	84.3	71.3	10.78	0.039	2.58	0.640	564.2
ENE local	155.4	8.3	20.83	0.039	2.87	0.194	564.2
SH2 local	0.0	47.5	12.71	0.039	2.61	0.429	564.2

<sup>1</sup> Fisher concentration

The first two steps in the extraction of data from the fracture realizations were previously performed for the 11 Mar 2014 delivery:

1. Extraction of all hexagonal fractures (panels) with equivalent radius  $> 50$  m
2. Conversion of the resulting (thinned) set of hexagonal fractures to disks (not used directly for the production of these datasets, but used to simplify checks of the statistical properties of the fracture population);

The present data delivery starts from the results of these previous two steps, and continues with:

3. Identification of fractures that cross a vertical section striking N50W, with end points (1630380, 6701267) and (1636032, 6696650) in RAK coordinates, between  $z = 0$  m and  $z = -2100$  m, and extraction of fracture traces on that plane, using the DFM module *dfmslice* v. 2.4.1.1.
4. Further processing of the 2-D cross-section data to the format requested by GFZ.

These steps are carried out by the following Linux C-shell script which was used to extract these data from DFN simulated fracture data files with the corresponding names of the form:

SRGeoPFC\_r2\_##\_fracs.pan,

that were produced for the  $N_{crit}$  task.

**PFC\_get\_thin\_sections\_r2\_vertical**

```
#!/bin/csh -f
#
# Script used to thin fractures and post-process fracture panels files into 3-D disk format.
#
set SRC = "../FMcritical2"
set STEM = "SRGeoPFC"
foreach CASE ( r2 )
  foreach N ( 01 02 03 04 05 06 07 08 09 10 )
    set NAME = "${STEM}_${CASE}_${N}"
    if ( -f ${NAME}_thin_fracs.pan ) then
      awk -f hexpanel_disks.awk -v OPT=DIP ${NAME}_thin_fracs.pan >
${NAME}_thin_disks.prn
      dfmslice2411 -p ${NAME}_thin_fracs.pan -x XsectionNWSE.pan >
${NAME}_thin_NWSE.prn
      awk -f processNWsection.awk ${NAME}_thin_NWSE.prn ${NAME}_thin_disks.prn >
${NAME}_NWSE2dr.prn
    endif
  end
end
```

The source files for these calculations are contained in the directory:

~/Desktop/modelling/PFCsimulations

**Quality Check 1: Comparison of expected and simulated P32 fracture intensity as a function of fracture radius**

This quality check was carried out based on the full DFN realizations for the  $N_{crit}$  calculations, prior to thinning. The comparison is based on the increments of  $P_{32}$ , the fracture intensity per unit volume, for a given range of fracture radii  $[r_1, r_2]$ . For

brevity these increments are referred to as  $P_{32}[r_1, r_2]$ . The results were presented in the quality-check memo for the 11 Mar 2014 delivery. As the present delivery uses exactly the same DFN realizations, this quality check is not repeated here.

### **Quality Check 2: Fracture orientation distributions**

The simulated fracture orientation distributions were confirmed both quantitatively by statistical measures, and qualitatively by equal-area stereonet plots for individual fracture sets. The results were presented in the quality-check memo for the 11 Mar 2014 delivery. As the present delivery uses exactly the same DFN realizations, this quality check is also not repeated here.

### **Quality Check 3: Comparison of expected and simulated P21 fracture intensity on the sampling plane**

The third main check of quality is to compare the observed values of fracture intensity as measured in the same 2-D cross-sections for which data are delivered, in terms of the  $P_{21}$  fracture intensity (trace length per unit area).

This can be estimated from the volumetric fracture intensity  $P_{32}$ , after correcting for the effects of truncating the fracture size distribution by thinning out the fractures smaller than 50 m radius, and the orientation bias that results from the orientation of the horizontal sampling plane relative to the fractures in each fracture set. The orientation bias is quantified by the factor  $C_{23}$  as defined by Wang (2005; see Geier, 2014a for details and method of calculation). The results are listed in Table A2.5.

The expected  $P_{21}$  values can be compared with the total fracture trace length per unit area of the cross-section. This has been taken in the portion of the model within the volume that has been focused on for the repository simulations, to avoid other censoring effects.

The results as shown in Figure A2.17 are generally close to (but slightly higher than) the expected values for fracture domain FFM01. The median value of the realizations is just slightly below area-weighted average of the expected values for the two domains, FFM01 and FFM06.

Therefore this match is judged as adequate as a check that the results are reasonable. A more precise, direct evaluation of  $P_{21}$  would require separate treatment of fractures from the two domains, and calculation of truncated trace lengths within the precise boundaries of the repository footprint. While such a calculation is achievable, it requires more complex steps which would diminish its value as a simple, direct verification procedure. It is noted that the more precise quantitative checks of  $P_{32}$  and the orientation distribution, as given in the memorandum for the previous data delivery, also are expected to constrain  $P_{21}$ , and that direct calculations of  $P_{21}$  for more well-constrained 50 m block geometries, in a related task, agreed within 1% of the expected values.

**Table A2.5.** Parameters for fracture sets for the  $r_0$ -fixed alternative, Calculation Case r2, and resulting values of truncated  $P_{32}$  (for minimum fracture radius of 50 m), and corresponding values of the geometric factor  $C_{23}$  and  $P_{21}$ .

	Mean pole trend	Mean pole plunge	$\kappa^1$	$P_{32}^2$	$P_{32}^3$	$\rho$	$1/C_{23}$	$P_{21}$
FFM01								
NE global	314.9	1.3	20.94	1.733	0.0081	85.1	0.9730	0.0079
NS global	270.1	5.3	21.34	1.292	0.005	50.3	0.7650	0.0038
NW global	230.1	4.6	15.7	0.948	0.0091	11.1	0.3477	0.0032
SH global	0.8	87.3	17.42	0.624	0.0073	87.9	0.9707	0.0071
ENE local	157.5	3.1	34.11	0.256	0.0002	62.5	0.8770	0.0002
EW local	0.4	11.9	13.89	0.169	0.0002	41.1	0.6674	0.0001
NNE local	293.8	0	21.79	0.658	0.0005	73.8	0.9401	0.0004
SH2 local	164	52.6	35.43	0.081	0.0008	70.1	0.9296	0.0007
SH3 local	337.9	52.9	17.08	0.067	0.0006	73.6	0.9348	0.0006
Total					0.0318			0.0240
FFM06								
NE global	125.7	10.1	45.05	3.299	0.0097	85.8	0.9863	0.0095
NS global	91	4.1	19.49	2.15	0.0067	51.1	0.7728	0.0052
NW global	34.1	0.8	16.13	1.608	0.0112	6.0	0.3159	0.0035
SH global	84.3	71.3	10.78	0.64	0.0075	76.7	0.9312	0.0070
ENE local	155.4	8.3	20.83	0.194	0.0003	64.9	0.8877	0.0003
SH2local	0	47.5	12.71	0.429	0.0041	58.8	0.8357	0.0035
Total					0.0395			0.0290

<sup>1</sup> Fisher concentration.

<sup>2</sup> Unscaled.

<sup>3</sup> Truncated.

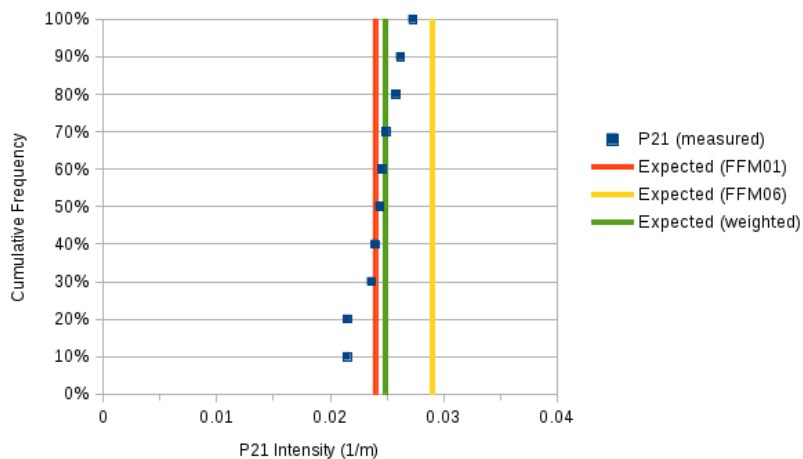


**Figure A2.17.** Measured vs. expected  $P_{21}$  values for ten realizations of the  $r_0$ -fixed model.

### Plots of cross-sections

Figures A2.18 and A2.19 give plots of fracture traces in the vertical plane striking N50W from Calculation Case r2, for realizations 01 through 05 (Figure 2), for realizations 06 through 10 (Figure 3). In all of these plots the spacing of yellow grid lines is 500 m in both directions. Figures 4 gives plots of fracture embedded in the PFC model.

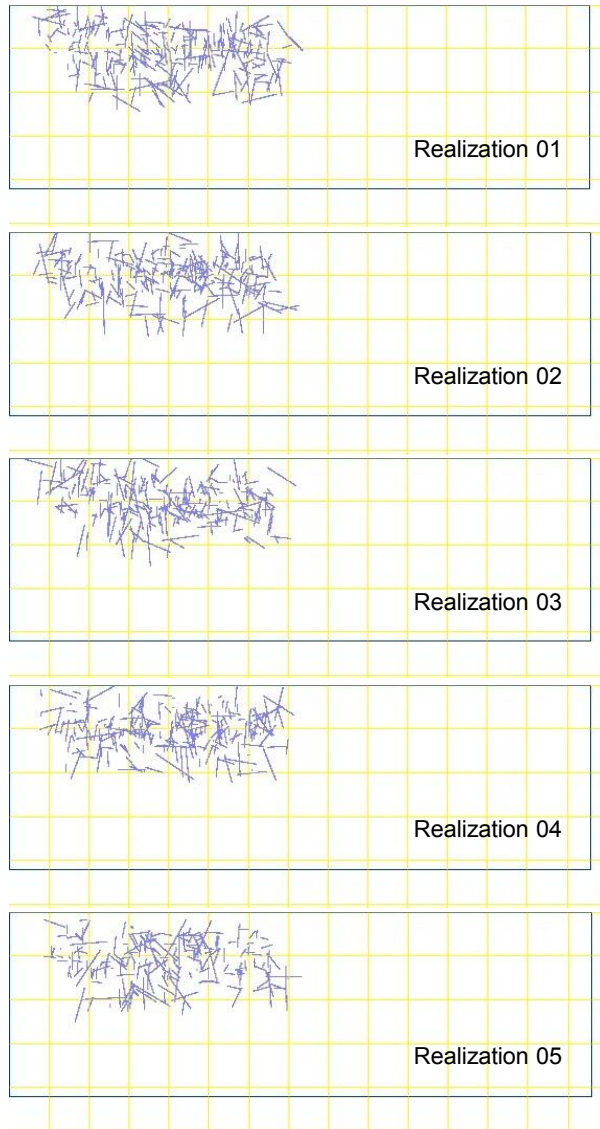


**Figure A2.18.** Fracture traces in the vertical plane striking N50W-S50E in Calculation Case r2, Realizations 01-05.

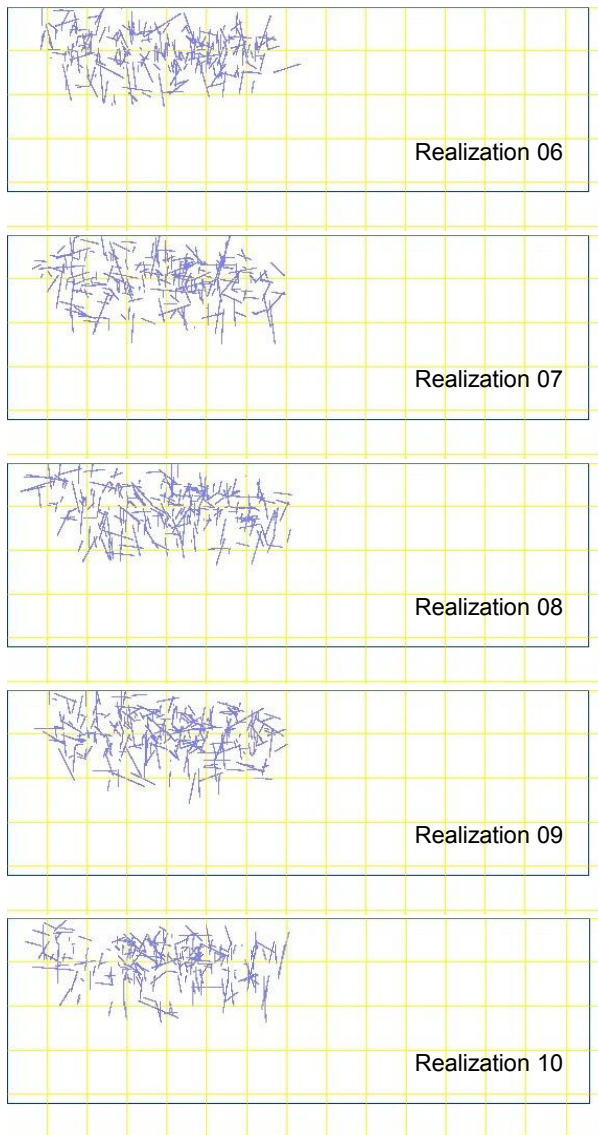


**Figure A2.19.** Fracture traces in the vertical plane striking N50W-S50E in Calculation Case r2, Realization 06-10.

